

HYDRODYNAMIC THEORY OF WET PARTICLE SYSTEMS

Sudeshna Roy

Thesis committee members:

Chair:

Prof.dr. G. P. M. R. Dewulf,

Universiteit Twente

Promotor:

Prof.dr.rer.-nat. S. Luding,

Universiteit Twente

Co-promotor:

Dr. T. Weinhart,

Universiteit Twente

Commission:

Prof.dr. R. M. van der Meer,

Universiteit Twente

Dr.ir. N. P. Kruyt,

Universiteit Twente

Prof.dr.-ing. S. Antonyuk,

Technische Universität Kaiserslautern

Prof.dr.rer.-nat. D. E. Wolf,

Universität Duisburg-Essen

Prof.dr.-ing. habil. R. Schwarze,

Technische Universität Bergakademie Freiberg

MESA+
INSTITUTE FOR NANOTECHNOLOGY



UNIVERSITY OF TWENTE.

The work in this thesis was carried out at the Multiscale Mechanics (MSM) group, MESA+ Institute of Nanotechnology, Faculty of Engineering Technology (ET), University of Twente, Enschede, The Netherlands.

This work was financially supported by STW grant number 12272, 'Hydrodynamic theory of wet particle systems. Modeling, simulation and validation based on microscopic and macroscopic descriptions'.

Cover design: S. Roy and Dr. H. Y. Cheng, figure taken from Chapter 6, Figure 6.2.

Copyright © 2017 by S. Roy

Published by Ipskamp Printing, Enschede, The Netherlands

ISBN: 978-90-365-4468-9

DOI number: 10.3990/1.9789036544689

Official URL: <https://doi.org/10.3990/1.9789036544689>.

HYDRODYNAMIC THEORY OF WET PARTICLE SYSTEMS

DISSERTATION

to obtain
the degree of doctor at the University of Twente,
on the authority of the rector magnificus,
Prof.dr. T.T.M. Palstra,
on account of the decision of the graduation committee,
to be publicly defended
on Friday 26th January 2018 at 14:45 hrs

by

Sudeshna Roy
born on the 1st October 1984
in Kolkata, India.

This dissertation was approved by the promotor:

Prof.dr.rer.-nat. S. Luding

and the co-promotor (supervisor):

Dr. T. Weinhart

In the loving memory of my mother.



CONTENTS

Summary	xi
Samenvatting	xiii
1 Introduction	1
1.1 Introduction	1
1.2 Goals and questions	5
1.3 Dissertation overview	6
References	7
2 A general(ized) local rheology	11
2.1 Introduction	11
2.2 Model System	13
2.2.1 Geometry	13
2.2.2 Contact model and parameters	14
2.2.3 Averaging methodology	15
2.2.4 Critical state	16
2.3 Time scales	17
2.4 Rheology of dry granular materials	19
2.4.1 Effect of softness in the bulk of the materials.	19
2.4.2 Effect of inertial number	19
2.4.3 Effect of gravity close to the free surface	20
2.4.4 Shear rate dependence in critical state flow	21
2.5 Rheology of wet-cohesive granular materials	23
2.5.1 Bond number	23
2.5.2 Effect of gravity close to the free surface	24
2.6 Rheological model	25
2.7 Local visco-plasticity	26
2.7.1 Prediction of local visco-plasticity	27
2.7.2 Eliminating the effect of cohesion and gravity	30
2.8 Discussions and conclusions	31
References	32
3 Effect of cohesion on local compaction	37
3.1 Introduction	37
3.2 Model System	38
3.2.1 Geometry	38
3.2.2 Contact model and parameters	39

3.3	Dimensionless numbers	39
3.4	Rheological model	40
3.4.1	Non-cohesive granular materials	40
3.4.2	Cohesive granular materials	40
3.5	Conclusion	43
	References	43
4	Micro-macro transition	45
4.1	Introduction	45
4.2	Model system	47
4.2.1	Geometry	47
4.2.2	Microscopic model parameters	48
4.2.3	Liquid bridge contact model	50
4.2.4	Dimensional analysis	53
4.3	Micro macro transition	53
4.3.1	Steady state cohesion and its correlation with liquid bridge volume and surface tension	54
4.3.2	Macroscopic torque analysis from the micro parameters	57
4.4	An analogous linear adhesive contact model for cohesive particles	60
4.4.1	Equal maximum force and interaction distance	61
4.4.2	Equal maximum force and adhesive energy	62
4.4.3	Different maximum force for the two contact models	63
4.5	Conclusion	65
	References	66
5	Liquid re-distribution in sheared wet granular media	69
5.1	Introduction	69
5.2	System	71
5.2.1	Geometry	71
5.2.2	DEM model	71
5.2.3	Liquid migration model	73
5.2.4	Initial conditions.	74
5.3	Micro-macro transition	76
5.3.1	Identifying the shear band	76
5.3.2	Wet shear band phenomenology.	76
5.4	Results	77
5.4.1	Transients for liquid re-distribution	77
5.4.2	Liquid re-distribution in pseudo-critical state	79
5.4.3	Dependence on the relative shear rate threshold.	81
5.4.4	Dependence on the liquid bridge limit-volume	82
5.4.5	Dependence on the liquid saturation	83
5.4.6	Effect of diffusion and transport of liquid	83
5.5	Conclusions.	84
	References	85

6	Diffusive-convective liquid migration	89
6.1	Introduction	90
6.2	System and numerical schemes.	91
6.2.1	Geometry	91
6.2.2	Discrete Element Model	91
6.2.3	Continuum Model	92
6.3	Comparison of DEM and continuum model	93
6.3.1	Liquid density	93
6.3.2	Trajectory of liquid migration	94
6.4	Effect of diffusion in vertical direction	95
6.5	Transformation to drift and diffusion equation	95
6.5.1	Drift	97
6.5.2	Diffusion.	98
6.5.3	Significance of drift and diffusion	98
6.5.4	Superposition of drift and diffusion effects.	99
6.6	Conclusion	100
	References	100
7	Surface flow profiles for dry and wet granular materials	103
7.1	Introduction	103
7.2	Experimental set-up	105
7.2.1	Geometry	105
7.2.2	Particles	105
7.2.3	Liquids and concentrations	106
7.3	Velocity measurement	107
7.3.1	Particle Tracking Velocimetry	107
7.3.2	Coarse-graining: Discrete to continuum velocity field	108
7.4	Experiments with dry glass beads	110
7.4.1	Varying filling height.	110
7.4.2	Varying shear rate	112
7.5	Experiments with wet glass beads.	113
7.5.1	Effect of glycerol	114
7.5.2	Effect of silicon oil	115
7.6	Conclusion	117
	References	117
8	Conclusions and Outlook	121
A	Appendix	125
A.1	Continuum model	125
A.1.1	Continuum equations	125
A.1.2	Rheology.	126
A.1.3	Continuum solution	127
	References	128

Acknowledgements	129
Curriculum Vitae	133
List of Publications	135

SUMMARY

External forces lead to granular flow under the condition that the applied shear stress reaches the yield (shear) stress while an (other) stress must be maintained for continuous flow in steady state. Most studies in granular physics focus on dry granular materials and their flow rheology. However, wet granular materials are ubiquitous in geology and many real world applications where interstitial liquid is present between the grains. There are several proposals for flow rules of dry and wet granular materials available in the literature. These flow rules differ in complexity and in the number of parameters, which are combined in the equations. The main focus areas of my research are (i) the formulation of suitable constitutive equations for the hydrodynamic density-stress-strain relations, specifically for wet granular materials, (ii) the deduction of the constitutive equations from discrete element simulations, and (iii) the validation of the micro-macro transition with numerical, theoretical and experimental results. The geometrical set-up of split-bottom shear cell used in my research is most appropriate for assessing the shear band originating from the split position that widens near the free surface. The velocity profiles exhibit tails that decay as an error function.

In partially saturated systems, in the pendular regime, the formation of liquid bridges between particle pairs leads to the development of microscopic tensile forces, resulting in cohesion at macroscopic scale. For this, macroscopic quantities consistent with the conservation laws of continuum theory, are obtained by time averaging and spatial coarse graining of the discrete constituents. Initial studies involve understanding the effects of liquid content and liquid properties on the macroscopic quantities. One research goal is to understand the essential phenomena and mechanisms, which determine the rheology of dry and wet granular flow under a different complex conditions. The rheology is described in terms of different dimensionless numbers that relate the time scales of significant phenomena, namely, the time scales related to confining pressure t_p , shear rate t_γ , particle stiffness t_k and cohesion t_c , respectively. Those phenomena collectively contribute to the rheology, entering as multiplicative corrective functions (that turn out to be first order linear). Thus, my research proposes a modified generalized flow rule/rheology to close the fundamental conservation laws for mass and momentum. Subsequently, a correlation is developed between the micro parameters and the steady state cohesion in the limit of very low confining pressure. The macroscopic torque measured at the walls, which is an experimentally accessible parameter, is predicted from simulation results and from the model in dependence on the steady state cohesion.

Another aspect of studying unsaturated granular media is the movement of interstitial liquid due to the rupture of existing and formation of new liquid bridges. Shearing a wet granular system causes a re-distribution of the interstitial liquid. This can strongly change the materials' bulk behavior. I study the transients of this liquid re-distribution, using the Discrete Element Method (DEM) for different initial wetting conditions. The

liquid is then re-distributed under shear. For small shear strain, the interstitial liquid is locally re-distributed to a quasi-steady state almost independent of the initial condition, while for larger shear strain, liquid is transported diffusively away from the shear zone. It is observed in earlier studies that depletion of liquid is observed in the shear band during shear. A front of high density of liquid content is observed moving outwards to the tails of the shear band, demarcating the sheared depleted zone from the relatively saturated zone. This front is propagating towards the boundaries, possibly drying out the entire system, but the boundaries in the long run. This liquid transport can be modeled by a diffusion equation with a space-dependent diffusive coefficient in the split bottom geometry. Alternatively, it is shown here that this is an advective-diffusive process with constant diffusivity coefficient and a space-dependent drift, when transformed to a appropriate set of variables that can be solved analytically.

The final chapter of this thesis concerns the experimental work exploring the surface flow profile for different dry and wet granular materials. The novel experimental technique used is a combination of Particle Tracking Velocimetry (PTV) and Coarse Graining (CG) to obtain continuum velocity fields of granular flow.

SAMENVATTING

Externe krachten kunnen ertoe leiden dat granulaire materialen beginnen te stromen indien de opgelegde afschuifspanning de vloeigrens bereikt. Bij de meeste granulaire studies wordt gefocust op droge materialen en hun reologie. Echter zijn vochtige granulaire materialen alomtegenwoordig in geologie en industriële toepassingen wanneer er een vloeistof aanwezig is tussen de korrels. In de bestaande literatuur zijn er enkele regels hoe droge en natte granulaire materialen zich gedragen als ze stromen. Echter, deze regels verschillen in complexiteit en de hoeveelheid stromingsparameters als deze zijn vertaald naar vergelijkingen. De gebieden waar ik op focus in mijn onderzoek zijn (i) het formuleren van geschikte constitutieve vergelijkingen voor de hydrodynamische dichtheid-spanning-rek verhoudingen, specifiek voor vochtige granulaire materialen, (ii) het afleiden van de parameters voor deze vergelijkingen uit discrete element methode simulaties, en (iii) de toetsing van de micro-macro overgang door numerieke, theoretische en experimentele resultaten. De kenmerkende geometrische opstelling split-bottom shear cell is hiervoor het meest geschikt. Deze heeft een afschuifband beginnend op de split positie waar deze uitwaaiert richting het oppervlak waar het materiaal vrij kan stromen.

Ik onderzoek gedeeltelijk verzadigde systemen in het pendulum regime, waar de vorming van vloeistof bruggen tussen de korrels leidt tot de vorming van microscopische trekkrachten. Deze trekkrachten gevormd door vloeistofbruggen bij contact tussen korrels van op de macroschaal leiden tot cohesie. Het doel van ons onderzoek hier is het vinden van de micro-macro correlaties die geldig zijn voor zowel natte als vochtige granulaire materialen. Hiervoor zijn macroscopische grootheden nodig die verenigbaar zijn met de behoudswetten van de continuüm theorie. Deze worden verkregen door de discrete waarden te middelen over tijd en coarse grains over ruimte. De begin studies betreft het begrijpen van het effect van het vloeistof gehalte en de vloeistof eigenschappen op de macroscopische grootheden. Een van de doelen van het onderzoek is het begrijpen van de essentiële verschijnselen en mechanismen die de reologie van de vochtige granulaire stroming bepalen onder verschillende en complexe omstandigheden. De reologie is beschreven door middel van dimensieloze grootheden die de tijdschalen van de belangrijke verschijnselen met elkaar verbindt. Hierbij worden de tijdschalen met betrekking tot de lithostatische druk t_p , afschuif snelheid t_γ , korrel stijfheid t_k zwaartekracht t_g en de cohesie t_c meegenomen. Ik laat zien dat deze verschijnselen gezamenlijk bijdragen aan de reologie doordat deze als multiplicatieve correctie functie worden toegevoegd (welke eerste orde lineair blijkt te zijn). Dus geven wij als voorstel een aangepaste gegeneraliseerde stromingsregel/reologie om alle belangrijke relaties tussen de stromingsvariabelen te omvatten welke nodig zijn om de fundamentele behoudswet van massa en impuls te sluiten. Vervolgens is er een correlatie afgeleid tussen de micro-parameters en de steady-state cohesie inclusief de limiet met lithostatische druk van nul. De macroscopische koppel gemeten aan de wand, een parameter die experimen-

teel gemeten kan worden, is voorspeld doormiddel van mijn simulatie resultaten met afhankelijkheid van de micro-parameters.

Een ander aspect van het onderzoek naar niet gesatureerde granulaire materialen is de verplaatsing van de vloeistof tussen de korrels door de afschuiving doordat bestaande vloeistofbruggen worden verbroken en nieuwe worden gevormd. Door een afschuiving aan te brengen op een vochtig granulair systeem herverdeeld deze vloeistof zich. Dit kan leiden tot een sterke verandering in het gedrag van het bulkmateriaal. Ik onderzoek de overgang van deze vloeistof herverdeling door middel van de Discrete Element Methode (DEM) voor verschillende initiële bevochtiging condities. Voor kleine afschuivingen, wordt de vloeistof tussen de korrels lokaal herverdeeld. Voor grotere afschuivingen wordt de vloeistof weg getransporteerd uit het afschuif gebied. Vloeistof migratie is een interessant verschijnsel in afschuivende granulaire materialen. In eerdere studies is waargenomen dat er uitdunning van vloeistof optreedt in de afschuif band gedurende afschuiving. Een front van hoge concentratie van vloeistof beweegt zich naar buiten naar de randen van de afschuif band, waardoor er een scheidslijn ontstaat tussen het uitgedunde gebied en het relatief verzadigde gebied. Dit front verplaatst zich richting de randen, wellicht kan dit het hele systeem uitdrogen met uitzondering van de randen op een groter tijdsinterval. Voorgaande studies laten zien dat deze vloeistof verplaatsing kan worden gemodelleerd door middel van een diffusie vergelijking met een ruimte-afhankelijk diffusie coëfficiënt in de split-bottom geometrie. Echter laten wij een alternatief zien dat het een advection-diffusie proces met een constante diffusie coëfficiënt en ruimte-afhankelijk drift coëfficiënt als deze wordt omgeschreven naar een andere set variabelen.

In het laatste hoofdstuk van deze thesis, focussen wij op het experimentele werk. Ik verken het oppervlakte stroom profiel en afschuifband eigenschappen met verschillende condities in droge en vochtige granulaire stromingen. De nieuwe experimentele techniek die ik gebruik is een combinatie van Particle Tracking Velocimetry (PTV) en Coarse Graining (CG) om continuüm snelheid velden te krijgen.

1

INTRODUCTION

1.1. INTRODUCTION

Matter is usually classified into solids, liquids and gases. Granular material is a collection of distinct macroscopic particles, such as sand in an hourglass or peanuts in a container. They behave differently than solids, liquids, and gases which has led many to characterize granular materials as a new form of matter. One of the biggest challenges is when we try to model granular material flow i.e. the “hydrodynamics of granular matter” as major goal of this thesis. For example, if we look at the top section of an hour glass as shown in Figure 1.1, we see that the grains are stationary, behaving like solids. In the center and close to the bottom of the top section, near the nozzle, the grains flow and thus behave like a liquid. When we move to the bottom section of the compartment, the grains form a conical heap signifying that the materials can support their own weight, unlike a standard liquid. In fact when we look at the downstream and where the stream hits the top of the cone, we might be able to see that the grains are actually colliding and bouncing around much like we expect in a gas. Yet, in contrast to what is seen in atomistic gases, the collisions between the grains are inelastic and dissipative in nature, leading to energy loss due to mechanisms like friction between the grains. Thus, in this one geometry, we see that what appears to be granular solid, liquid and gas co-existing at the same time, yet they do not behave like ideal solids, liquids or gases.

Judging from the ease with which granular matter flows through the orifice of an hourglass, or forms sand dunes like waves on the ocean, dry sand could be called a fluid, very much resembling regular liquids, like water. However, when some liquid like water is mixed into dry sand, a pasty, more viscous material emerges which loses its fluidity partially. Thus, the addition of liquid forming capillary bridges between the adjacent grains plays an important role in the transition from liquid- to solid-like behavior [1–5]. Another example is a sandcastle, see Figure 1.2. With a sandcastle, the wet sand can be held together like a solid, but it can also fall apart as it dries, breaking off the walls of an inclined surface in an avalanche, in “wedges”, or in other patterns.

Even though sand may appear liquid-like, and wet sand may appear solid-like, it is not yet clear if any standard fluid dynamics principle can be applied, especially in the

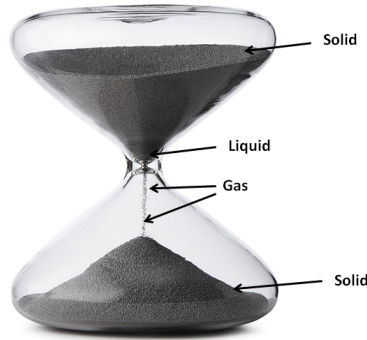


Figure 1.1: Hour Glass demonstrating the behavior of granular materials (Copyright Walls Cover).

transition from fluid to solid when going from dry to wet flow. The need for bulk predictions has restricted the studies of granular materials mainly to *real* systems which are far too complex for a microscopic approach. One rather uses continuum models, with empirical material laws as input which exhibit effects similar to those observed in the real systems of materials. Continuum constitutive relations for bulk granular flow, forming the basis for a hydrodynamic theory are mostly derived and verified from small scale representative micro-scale simulations. Several studies have been done on the constitutive relations for dry granular materials within the last decade, mostly based on simulations and experiments. The presence of interstitial liquid for wet materials adds further complexity to that. Several constitutive models for the stress strain behavior of partially saturated soils are proposed [9, 10]. An extension of the Mohr Coulomb failure criterion is presented to include partial saturation, through a new angle of friction and by including cohesion [11]. From the soil mechanics perspective, special attention has been paid to the use of effective stress. The basic information like the degree of saturation for finding the equivalent fluid pressure in unsaturated soil is given by Bishop-type formulations. It is suggested that this effective stress should be related to the soil microstructure [6–8].

When one takes a closer look on the characteristics of liquid, one might notice that liquid flows readily; yet it can adopt extremely stable shapes when the volume is very small. A liquid surface can be thought of as a stretched surface characterized by a surface tension that opposes its distortion. In fact, a liquid molecule near the surface loses half its cohesive interactions with the surrounding molecules, thus resides under tension causing surface tension and resulting in capillary forces in presence of other materials. Capillary forces are truly remarkable. They enable insects to walk on water. As we will see later, the two aspects of surface tension energy and force will be a recurring theme. The capillary force in unsaturated granular media originates from the attractive forces due to the surface wetting property of the liquid between the particles, see Figure 1.3. The liquid meniscus between the two particles is concave and has a negative radius of curvature, showing a pressure difference between the liquid and the vapor phase, i.e. pressure in the liquid is lower than in the vapor phase. However, this holds true for most



Figure 1.2: Sand castle demonstrating the behavior of wet granular materials (Copyright Sandscapes).

generalized cases when the liquid is wetting and liquid/ solid/ vapor contact angle is less than 90° . The capillary bridge will exhibit a convex meniscus with positive radius of curvature if the liquid/ solid/ vapor contact angle is greater than 90° when the liquid is non-wetting [12–14]. The Laplace-Young equation describes the pressure difference sustained across the interface between the phases due to surface tension [15–18]. The profile and properties of liquid bridges is governed by the Laplace-Young equation [19–24]. It relates the pressure difference to the radius of curvature of the meniscus and is of fundamental importance for the study of capillary bridges.

Several capillary bridge models (CBMs) are deduced based on experimental information and numerical solution of the Laplace Young equation and have been the subject of investigations within the last decade [20, 25, 26]. They all have in common that the irreversible force becomes active at contact only, but is active upto a cut-off distance at rupture of the bridge. These CBMs can be implemented in particle based simulation methods, for example the Discrete Element Method (DEM), in order to model the effects of individual capillary bridges between particles on the bulk materials. The resulting bulk behavior (and hydrodynamics) can not easily be anticipated from the functional relationships given by the different CBMs. Recent studies confirmed that the specific choice of the CBMs has no marked influence on the hydrodynamics of granular flow [27, 28] for small volumes of interstitial liquids. In fact, the force at contact and the energy, i.e. the integrated capillary force of the CBMs determine the bulk properties. However, whether one can tune the parameters of completely different cohesive contact models to obtain the same bulk behavior, for example a dry cohesive model with non-contact, reversible Van der Waals forces, is still an open question that needs to be addressed.

Though capillary cohesion is associated with all liquid bridges, the stability of liquid bridges subjected to external forces is a matter of discussion which has a long history. Several studies have been done under varied conditions of electric fields [29, 30], gravity fields [31, 32], under vibration [33, 34] or shear [35, 36] to examine the changes in shape and spreading of capillary bridges. The rupture of liquid bridges, spreading of liquids and then formation of new liquid bridges leads to the re-distribution as well as transport of liquid [36]. Another source of liquid transport is the diffusion of the particles and

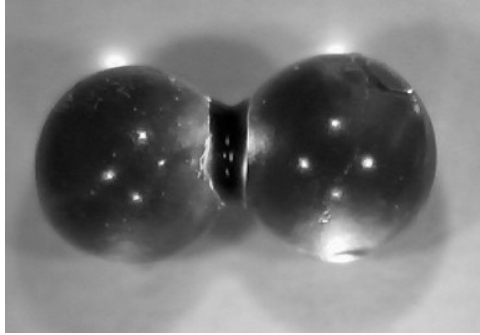


Figure 1.3: Liquid capillary bridge between particles.

their associated liquid films [37]. The liquid transport modes are controlled by the local saturation and the shear rate in the system. Liquid is drawn into dilating shear band granular media when the system is fully saturated. However, one finds a depletion of liquid in shear bands of unsaturated granular media, despite increased porosity due to dilatancy. Though, there has been recent progress on experiments and numerical modeling of liquid transfer in sheared unsaturated granular media, the dynamics of the liquid re-distribution and the associated transport processes are still not revealed.

Since decades, granular media have been subject of many studies, ranging from static conditions to flowing, from hard to soft-particles and from dry to partially wet to fully saturated. Micromechanical studies of granular materials gives an essential understanding of their macro-scale behavior. Studies by Radjai et al. [65] classifies the contacts into subnetworks of strong and weak contacts, where it is shown that the anisotropic shear stress of granular materials is primarily carried by the strong contacts. Many other micromechanical studies of granular materials aimed towards understanding of their elastic moduli behavior [66], contact force networks [67], dilatancy behavior [68]. From the perspective of granular flow, researchers have investigated different flow configurations like plane shear, Couette cell, silos, flows down an inclined plane, or avalanches on piles and in rotating drums [38–42]. Shear bands, localized regions of concentrated shear are an important feature of complex fluids like granular materials, deformed irreversibly [43, 44]. Granular materials are characterized by enduring contacts between particles and the existence of force chains [45–49]. Shear band formation has been extensively studied in specific, for plastic granular flows in rectangular, vertical-pipe chute configurations. In these geometries, granular flows exhibit plug flow in the central region with shear bands near the side walls. Shear band formation with a wider range of flow rates is probed in annular Couette cell geometry where an exponentially decaying velocity profile is well established near the wall. Until 2001, it was mostly reported that granular shear bands are narrow i.e. a few particle diameters wide and are accompanied by strong localisation of strain. In a modified Couette cell, or so-called split-bottom shear cell, granular flow is driven from the bottom, instead from the side walls [50–55]. Typically, a disc of radius R_s , mounted at the bottom is rotated at a rate Ω and the outer container is fixed. The differential motion of the of the disc and the container creates

a very thin shear band at bottom that becomes robust and wide upwards and remains away from the walls. The tails of velocity profile decay as an error function, not an exponential function like the Couette cell. These observations strongly indicates that there is a continuum theory with its own domain of validity, that should capture this smooth quasi-static granular flow regime.

Partly saturated granular systems, mostly in the quasistatic, dense steady-state flow regime, as realized in a split-bottom shear cell geometry. We make an attempt to understand and predict the hydrodynamics or rheology of such shear-driven granular flows through discrete particle simulations by utilising accurate discrete to continuum mapping methods, i.e. a micro-macro transition. Secondly, we focus on the migration of interstitial liquid itself within the wet granular media and predict its flow by continuum models, calibrated by discrete particle simulations and establish close agreement between the two methods. Finally, we use also experimental techniques to explore some of the rheological properties of dry and wet granular flows. Before we progress with the descriptions of our findings and results, in the following chapters, we proceed by briefly introducing the specific goals of this thesis and overview of the chapters.

1.2. GOALS AND QUESTIONS

The aim of this thesis is to study wet granular materials in quasistatic shear flows. Dry and wet granular materials are ubiquitous in many forms, be it in industries, earth and agricultural sciences, in nature or in celestial bodies. How does the presence of interstitial liquid at the microscopic level influence the macroscopic bulk properties and flow of the materials? Are wet granular materials an extension of their dry counterpart or are they completely different? These questions remain in our mind and will be addressed in this thesis.

A liquid bridge capillary force model is well prescribed for modeling unsaturated granular materials. Can we replace a non-linear capillary force by a simple linear one to get similar bulk properties? How can we tune or scale the micro parameters to get the same bulk behavior and how much detail is needed at the micro-scale anyway? Answers to this would also give us the key parameters of contact models for the DEM simulation.

Another area of particular interest to many scientists is the flowing behavior of granular materials under shear, especially in the presence of an interstitial fluid. It is noteworthy that the particles and the interstitial liquids behave differently under shear, thus leading to rearrangement and transport of liquid. This is of fundamental importance in the field of agriculture, soil mechanics or petroleum engineering. Shear being the fundamental factor, the question comes to our mind if shear is the sole factor influencing the liquid rearrangement and transport processes, irrespective of the time of shearing. Does the liquid re-distribution depend on the initial configuration? How do the liquid transport mechanisms work and can we develop a macro-model with micro-basis? This thesis tries to address most of the questions raised above, digging out the causes and effects. Indeed, this thesis answers some of the fundamental questions in the form of specific improved numerical models or analytical solutions of aspects of the “Hydrodynamic theory of wet particle systems” thesis.

1.3. DISSERTATION OVERVIEW

The chapters of this thesis are organized, starting from more generalized phenomenological models describing the rheology of granular materials over a wide domain explained in Chapters 2 and 3. In Chapter 4, we move towards more fundamental rheological model based on Mohr Coulomb theory to explore the micro-macro correlations. We deal with our initial studies on rheology of granular flow in Chapters 2, 3 and 4 by keeping the system simple and homogeneous in its liquid content. In a later stage in Chapters 5 and 6, we consider a more complex DEM model where liquid is allowed to move between particles and contacts. The complexity here lies in the fact that particles and their interstitial liquid flow differently when subjected to shear. Apart from the movement of the liquids along with the particles and contacts, there is additional movement of liquid whenever liquid bridges rupture. As a result, liquids are re-distributed or transported differently than the particles. So far we had been dealing with particle simulations in discrete scale and hydrodynamic theory in the form of steady-state rheology models obtained using DEM. However, in Chapter 6, we move to continuum modeling of liquid transport in granular media and its comparison with DEM. Last but not the least, we discuss about our experimental work in Chapter 7. Finally, we give our conclusion and an outlook in Chapter 8.

In Chapter 2, the challenge on the theoretical side is to extend the classical internal friction model, the so-called $\mu(I)$ rheology, and previous results on soft and dry non-cohesive materials, towards wet cohesive materials. A generalized rheology shows that the steady-state macro friction coefficient (or normalized shear stress) is factorized into a product of different functions, on top of the classical $\mu(I)$ rheology, each of which depends on at least one dimensionless control parameter. There are four control parameters relating the five time scales of shear rate $t_{\dot{\gamma}}$, particle stiffness t_k , gravity t_g and cohesion t_c , with the governing time scale of confining pressure t_p .

In Chapter 3, we investigate the effect of cohesion on the compaction or dilation of sheared soft, wet granular materials. Inter-particle cohesion has a considerable impact on the compaction of soft materials. Cohesion causes additional stresses, due to capillary forces between particles, leading to an increase in volume fraction due to higher compaction. This effect is not visible in a system of infinitely stiff particles. In addition, acting oppositely, we observe a general decrease in volume fraction for increased cohesion, which we attribute to the role of contact friction that enhances dilation. We complete the generalized rheology of Chapter 2 by a local volume fraction prediction described in terms of the different time scales or dimensionless numbers, in similar spirit of the generalized rheology for macro friction coefficient described in Chapter 2.

Chapter 4 describes micro-macro correlations valid for both dry and partially saturated granular materials. A simple constitutive relation based on the Mohr Coulomb failure criterion shows that the critical-state shear stress is constituted of the bulk cohesion and the macro friction coefficient [4, 56]. The bulk cohesion is correlated with the *Bond number* or *adhesion index*, measured from the microscopic parameters of the adhesive contact model [56, 57] and the confining stress or gravity.

In Chapter 5, we study the transients of this liquid re-distribution, using Discrete Element Method (DEM) simulations for varying initial wetting conditions. In our model, liquid is contained in liquid bridges between particles and liquid films on the particle

surfaces. The liquid is then re-distributed under shear, due to the rupture and formation of liquid bridges. A threshold liquid bridge volume is imposed to avoid clustering of liquid. Two distinct effects are observed: for small amounts of shear, the re-distribution of the interstitial liquid is dominant, while for larger amounts of shear, liquid transport by diffusion away from the shear zone is dominating. The local re-distribution quickly results in a characteristic distribution of liquid bridge volume, independent of the initial wetting conditions. The mean liquid bridge volume, however, is strongly affected by the threshold volume, showing the significance of this parameter. We further discuss the effects of local shear rate and the saturation on the transients of liquid re-distribution.

Chapter 6 is a continuation of the discussions of Chapter 5 in the larger shear scale when we observe liquid migration from the unsaturated shear band to the edges of the shear band. Earlier studies show that the liquid migration is modeled by a diffusive equation with a space-dependent diffusive coefficient in the split bottom geometry. We show that this is a drift-diffusion process with constant diffusivity coefficient and space dependent drift coefficient, when transformed to a different set of variables.

Finally, in Chapter 7, we give a glimpse of our experimental work on measuring the properties of the shear band at the free surface of dense granular flow in a split-bottom shear cell geometry. The discrete velocity of the particles at the free surface is obtained by 2D image analysis and Particle Tracking Velocimetry. The discrete particle velocity is further translated to a continuous velocity field by using coarse graining tool MercuryCG [58–61]. We estimate the location of shear band center and the width at the free surface from the surface velocity profile for dry and wet granular materials.

REFERENCES

- [1] S. Herminghaus, *Advances in Physics* **54**, 221 (2005).
- [2] N. Mitarai and F. Nori, *Advances in Physics* **55**, 1 (2006).
- [3] N. Huang, G. Ovarlez, F. Bertrand, S. Rodts, P. Coussot, and D. Bonn, *Physical Review Letters* **94**, 028301 (2005).
- [4] V. Richefeu, M. S. El Youssofi, and F. Radjai, *Physical Review E* **73**, 051304 (2006).
- [5] M. M. Kohonen, D. Geromichalos, M. Scheel, C. Schier, and S. Herminghaus, *Physica A: Statistical Mechanics and its Applications* **339**, 7 (2004).
- [6] E. E. Alonso, J.-M. Pereira, J. Vaunat, and S. Olivella, *Géotechnique* **60**, 913 (2010).
- [7] A. W. Bishop and G. Blight, *Géotechnique* **13**, 177 (1963).
- [8] X. Li, *Géotechnique* **53**, 273 (2003).
- [9] E. E. Alonso, A. Gens, and A. Josa, *Géotechnique* **40**, 405 (1990).
- [10] D. Sheng, S. Sloan, and A. Gens, *Computational Mechanics* **33**, 453 (2004).
- [11] D. Fredlund, N. R. Morgenstern, and R. Widger, *Canadian Geotechnical Journal* **15**, 313 (1978).

- [12] G. Mason and N. R. Morrow, *Journal of Colloid and Interface Science* **141**, 262 (1991).
- [13] W. A. Zisman, in *Contact Angle, Wettability and Adhesion* (ACS Publications, 1964).
- [14] P.G. De Gennes, *Reviews of Modern Physics* **57**, 827 (1985).
- [15] N. Maeda, J. N. Israelachvili, and M. M. Kohonen, *Proceedings of the National Academy of Sciences* **100**, 803 (2003).
- [16] R. Finn, *Notices of the AMS* **46**, 770 (1999).
- [17] T. Young *et al.*, in *Abstracts of the Papers Printed in the Philosophical Transactions of the Royal Society of London*, Vol. 1 (The Royal Society, 1832) pp. 171–172.
- [18] M. Rodriguez-Valverde, M. Cabrerizo-Vilchez, and R. Hidalgo-Alvarez, *European Journal of Physics* **24**, 159 (2003).
- [19] G. Lian, C. Thornton, and M. J. Adams, *Journal of Colloid and Interface Science* **161**, 138 (1993).
- [20] F. Soulie, F. Cherblanc, M. S. El Youssoufi, and C. Saix, *International Journal for Numerical and Analytical Methods in Geomechanics* **30**, 213 (2006).
- [21] J. Van Honschoten, N. R. Tas, and M. Elwenspoek, *American Journal of Physics* **78**, 277 (2010).
- [22] Y. I. Rabinovich, M. S. Esayanur, and B. M. Moudgil, *Langmuir* **21**, 10992 (2005).
- [23] N. Kruyt and O. Millet, *Journal of Fluid Mechanics* **812**, 129 (2017).
- [24] P. Rynhart, R. McLachlan, J. Jones, and R. McKibbin, *Massey Research Online* **5**, 119 (2003).
- [25] C. D. Willett, M. J. Adams, S. A. Johnson, and J. P. Seville, *Langmuir* **16**, 9396 (2000).
- [26] T. Weigert and S. Ripperger, *Particle & Particle Systems Characterization* **16**, 238 (1999).
- [27] A. Gladkyy and R. Schwarze, *Granular Matter* **16**, 911 (2014).
- [28] P. Lambert, A. Chau, A. Delchambre, and S. Régnier, *Langmuir* **24**, 3157 (2008).
- [29] E. Schäffer, T. Thurn-Albrecht, T. P. Russell, and U. Steiner, *Europhysics Letters* **53**, 518 (2001).
- [30] G. Taylor and A. McEwan, *Journal of Fluid Mechanics* **22**, 1 (1965).
- [31] L. A. Slobozhanin and J. I. D. Alexander, *Physics of Fluids* **9**, 1880 (1997).
- [32] I. Martínez and J. Perales, *Journal of Crystal Growth* **78**, 369 (1986).
- [33] E. Benilov, *Physical Review E* **93**, 063118 (2016).

- [34] W. Hu, J. Shu, R. Zhou, and Z. Tang, *Journal of Crystal Growth* **142**, 379 (1994).
- [35] A. K. Uguz, N. Alvarez, and R. Narayanan, *Journal of Colloid and Interface Science* **346**, 464 (2010).
- [36] R. Mani, D. Kadau, D. Or, and H. J. Herrmann, *Physical Review Letters* **109**, 248001 (2012).
- [37] B. Utter and R. P. Behringer, *Physical Review E* **69**, 031308 (2004).
- [38] Y. Forterre and O. Pouliquen, *Annual Review of Fluid Mechanics* **40**, 1 (2008).
- [39] P. Schall and M. van Hecke, *Annual Review of Fluid Mechanics* **42**, 67 (2010).
- [40] G. MiDi, *European Physical Journal E* **14**, 341 (2004).
- [41] P. Jop, Y. Forterre, and O. Pouliquen, *Nature* **441**, 727 (2006).
- [42] O. Pouliquen, C. Cassar, P. Jop, Y. Forterre, and M. Nicolas, *Journal of Statistical Mechanics: Theory and Experiment* **2006**, P07020 (2006).
- [43] P. A. Cundall, *Archive of Applied Mechanics* **59**, 148 (1989).
- [44] H. Mühlhaus and I. Vardoulakis, *Géotechnique* **37**, 271 (1987).
- [45] T. S. Majmudar and R. P. Behringer, *Nature* **435**, 1079 (2005).
- [46] B. Miller, C. O'Hern, and R. Behringer, *Physical Review Letters* **77**, 3110 (1996).
- [47] D. Howell, R. Behringer, and C. Veje, *Physical Review Letters* **82**, 5241 (1999).
- [48] A. Ferguson, B. Fisher, and B. Chakraborty, *Europhysics Letters* **66**, 277 (2004).
- [49] A. Ferguson and B. Chakraborty, *Physical Review E* **73**, 011303 (2006).
- [50] D. Fenistein and M. van Hecke, *Nature* **425**, 256 (2003).
- [51] D. L. Henann and K. Kamrin, *Proceedings of the National Academy of Sciences* **110**, 6730 (2013).
- [52] J. A. Dijksman and M. van Hecke, *Soft Matter* **6**, 2901 (2010).
- [53] X. Cheng, J. B. Lechman, A. Fernandez-Barbero, G. S. Grest, H. M. Jaeger, G. S. Karczmar, M. E. Möbius, and S. R. Nagel, *Physical Review Letters* **96**, 038001 (2006).
- [54] K. Hill and Y. Fan, *Physical Review Letters* **101**, 088001 (2008).
- [55] D. Fenistein, J. W. van de Meent, and M. van Hecke, *Physical Review Letters* **92**, 094301 (2004).
- [56] S. Roy, A. Singh, S. Luding, and T. Weinhart, *Computational Particle Mechanics* **3**, 449 (2016).

- [57] F. Radjai and V. Richefeu, *Philosophical Transactions of the Royal Society of London A: Mathematical, Physical and Engineering Sciences* **367**, 5123 (2009).
- [58] T. Weinhart, A. R. Thornton, S. Luding, and O. Bokhove, *Granular Matter* **14**, 289 (2012).
- [59] A. Thornton, T. Weinhart, S. Luding, and O. Bokhove, *International Journal of Modern Physics C* **23**, 1240014 (2012).
- [60] T. Weinhart, D. Tunuguntla, M. van Schrojenstein-Lantman, A. van der Horn, I. Denissen, C. Windows-Yule, A. de Jong, and A. Thornton, in *Proceedings of the 7th International Conference on Discrete Element Methods* (2017) pp. 1353–1360.
- [61] A. Thornton, D. Krijgsman, R. Fransen, S. Gonzalez, D. Tunuguntla, A. Voortwis, S. Luding, O. Bokhove, and T. Weinhart, *EnginSoft's SBE&S Magazine* **10**, 48 (2013).
- [62] F. M. Fowkes, *Contact angle, wettability, and adhesion* (ACS Publications, 1964).
- [63] L. Wang and T. J. McCarthy, *Proceedings of the National Academy of Sciences* **112**, 2664 (2015).
- [64] Y. Yuan and T. R. Lee, in *Surface Science Techniques* (Springer, 2013) pp. 3–34.
- [65] F. Radjai, D. E. Wolf, M. Jean, and J.-J. Moreau, *Physical Review Letters* **80**, 61 (1998).
- [66] N. Kruyt, I. Agnolin, S. Luding, and L. Rothenburg, *Journal of the Mechanics and Physics of Solids* **58**, 1286 (2010).
- [67] N. Kruyt, *International Journal of Solids and Structures* **92**, 135 (2016).
- [68] N. Kruyt and L. Rothenburg, *Journal of the Mechanics and Physics of Solids* **95**, 411 (2016).

2

A GENERAL(IZED) LOCAL RHEOLOGY FOR WET GRANULAR MATERIALS

We study the rheology of dry and wet granular materials in the steady quasistatic regime using the Discrete Element Method (DEM) in a split-bottom ring shear cell with focus on the macroscopic friction. The aim of our study is to understand the local rheology of bulk flow at various positions in the shear band, where the system is in critical state. We develop a general(ized) rheology, in which the macroscopic friction is factorized into a product of four functions, in addition to the classical $\mu(I)$ rheology, each of which depends on exactly one dimensionless control parameter. These four control parameters relate the time scales of shear rate t_γ , particle stiffness t_k , gravity t_g and cohesion t_c , respectively, with the governing time scale of confining pressure t_p .

While t_γ is large and thus of little importance for most of the slow flow data studied, it can increase the friction of flow in critical state, where the shear gradients are high. t_g and t_k are comparable to t_p in the bulk, but become more or less dominant relative to t_p at the extremes of low pressure at the free surface and high pressure deep inside the bulk, respectively.

We also measure the effect of wet cohesion on the flow rheology, as quantified by decreasing t_c . Furthermore, the proposed rheological model predicts well the shear thinning behavior both in the bulk and near the free surface; shear thinning develops towards shear thickening near the free surface with increasing cohesion.

2.1. INTRODUCTION

The ability to predict a material's flow behavior, its rheology (like the viscosity for fluids) gives manufacturers an important product quantity. Knowledge on material's rhe-

This chapter has been published in New Journal of Physics **19**, (2017) [3].

ological characteristics is important in predicting the pourability, density and ease with which it may be handled, processed or used. The interrelation between rheology and other product dimensions often makes the measurement of viscosity the most sensitive or convenient way of detecting changes in flow properties. A frequent reason for the measurement of rheological properties can be found in the area of quality control, where raw materials must be consistent from batch to batch. For this purpose, flow behavior is an indirect measure of product consistency and quality.

Most studies on cohesive materials in granular physics focus on dry granular materials or powders and their flow [50, 52]. However, wet granular materials are ubiquitous in geology and many real-world applications where interstitial liquid is present between the grains. Many studies have applied the $\mu(I)$ -rheology to flows of dry materials at varying inertial numbers I [1, 2, 4–6]. Studies of wet granular rheology include flow of dense non-Brownian suspensions [7–10]. Here, we study partially wetted system of granular materials, in particular the pendular regime, which is also covered in many studies [11–13]. While ideally, unsaturated granular media under shear show redistribution of liquid content among the contacts [14, 15], we assume a simplistic approach of homogeneous liquid content for liquid bridges of all contacts. One of the important aspects of partially wetted granular shear flows is the dependence of shear stress on the cohesive forces for wet materials. Various experimental and numerical studies show that addition of liquid bridge forces leads to higher yield strength. The yield stress at critical state can be fitted as a linear function of the pressure with the friction coefficient of dry flow μ_o as the slope and a finite offset c , defined as the steady state cohesion in the limit of zero confining pressure [11]. This finite offset c is constant in the high pressure limit. However, very little is known regarding the rheology for granular materials in the low pressure limit.

Depending on the surrounding conditions, granular flows phenomenon are affected by appropriate time scales namely, t_p : time required for particles to rearrange under certain pressure, t_γ : time scale related to strain rate $\dot{\gamma}$, t_k : related to the contact time between particles, t_g : elapsed time for a single particle to fall through half its diameter under the influence of gravity and t_c : time scale for the capillary forces driving the flow are primarily hindered by inertia based on particle density. While various time scales, as related to the ongoing mechanisms in the sheared bulk of the material, can interfere, they also can get decoupled, in the extremes of the local/ global condition, if one time scale gets way smaller in magnitude than the other. A detailed description of this time scales are given in Sec. 2.3. While t_k , t_g and t_c are global, other time scales t_γ and t_p depends on local field variables strain rate $\dot{\gamma}$ and pressure p respectively. We restrict our studies to the quasi-static regime ($t_\gamma \gg t_p$) as the effect of cohesion decreases with increasing inertial number due to the fast decrease in coordination number [16]. Moreover, the quasistatic regime observed for non-cohesive particles also persist for cohesive particles, while the inertial regime of noncohesive particles bifurcates into two regimes: rate-independent cohesive regime at low shear rates and inertial regime at higher shear rates [17]. In the present work, we shed light on the rheology of non-cohesive dry as well as cohesive wet granular materials at the small pressure limit, by studying free surface flow. While the inertial number I [18], i.e. the ratio of confining pressure to strain-rate time scales, is used to describe the change in flow rheology from quasi-static to inertial conditions, we look at additional dimensionless numbers that influence the flow behav-

ior. (i) The local compressibility p^* , which is the squared ratio of the softness and stress time scales (ii) the inverse relative pressure gradient p_g^* , which is the squared ratio of gravitational and stress time scales and (iii) the Bond number Bo [19] quantifying local cohesion as the squared ratio of stress to wetting time scales are these dimensionless numbers. We show a constitutive relation based on these dimensionless numbers in Sec. 2.4, 2.5 and 2.6 of this paper. Additional relevant parameters are not discussed in this study, namely granular temperature or fluidity. All these dimensionless numbers can be related to different time scales or force scales relevant to the granular flow.

Granular materials display non-Newtonian flow behavior for shear stresses above the so called *yield stress* while they remain mostly elastic like solids below this yield stress. More specifically, granular materials flow like a shear thinning fluid under sufficient stress. When dealing with wet granular materials, it is therefore of fundamental interest to understand the effect of cohesion on the bulk flow and yield behavior. Recently, the majority of investigations of non-Newtonian flow behavior focused on concentrated colloidal suspensions. Shear thickening is often observed in those flows due to the formation of flow-induced density fluctuations (hydroclusters) resulting from hydrodynamic lubrication forces between particles [20]. Similar local clusters (aggregates) can also be found in strongly cohesive wet granular materials, especially near to the free surface, where attractive forces dominate their repulsive counterparts [50]. However, the strong correlations observed between particles of close proximity in suspensions seem to be irrelevant in wet granular systems, where the range of force interactions is much more limited. On the other hand, Lin et al. [21] show that contact forces dominate over hydrodynamic forces in suspensions that show continuous shear thickening. Fall et al. [22] propose that discontinuous shear thickening of cornstarch suspensions is a consequence of dilatancy: the system under flow attempts to dilate but instead undergoes a jamming transition because it is confined. Another possible cause for shear thickening is the large stress required to maintain flow due to particle-particle friction above a critical stress as in [23, 24]. This is more likely to happen in charge stabilized colloidal suspensions. Kann et al. [53] described the nonmonotonic oscillatory settling velocity of sphere in a cornstarch suspension, resulting from the jamming-unjamming behavior of the suspension solution. Here we only intended to speculate the flow behavior of cohesive granular materials in relevance to micro scale analogy for shear thickening in suspensions and Sec. 2.7 of this paper is devoted to understand more on the behavior of wet granular materials with increasing cohesion.

2.2. MODEL SYSTEM

2.2.1. GEOMETRY

Split- Bottom Ring Shear Cell: We use MercuryDPM [25, 26], an open-source implementation of the Discrete Particle Method, to simulate a shear cell with annular geometry and a split bottom plate, as shown in Figure 2.1. Some of the earlier studies in similar rotating set-ups include [27–29]. The geometry of the system consists of an outer cylinder (outer radius $R_o = 110$ mm) rotating around a fixed inner cylinder (inner radius $R_i = 14.7$ mm) with a rotation frequency of $\Omega = 0.01$ rotations per second. The granular material is confined by gravity between the two concentric cylinders, the bottom plate, and

a free top surface. The bottom plate is split at radius $R_s = 85$ mm. Due to the split at the bottom, a narrow shear band is formed. It moves inwards and widens towards the flow surface. This set-up thus features a wide shear band away from the bottom and the side walls which is thus free from boundary effects. The filling height ($H = 40$ mm) is chosen such that the shear band does not reach the inner wall at the free surface.

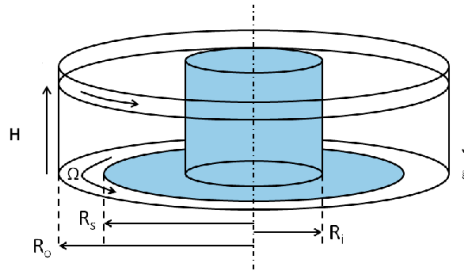


Figure 2.1: Shear cell set-up.

In earlier studies [1, 30, 50], a quarter of this system ($0^\circ \leq \phi \leq 90^\circ$) was simulated using periodic boundary conditions. In order to save computation time, here we simulate only a smaller section of the system ($0^\circ \leq \phi \leq 30^\circ$) with appropriate periodic boundary conditions in the angular coordinate, unless specified otherwise. We have observed no noticeable effect on the macroscopic behavior in comparisons between simulations done with a smaller (30°) and a larger (90°) opening angle. Note that for very strong attractive forces, agglomeration of particles occur. Then, a higher length scale of the geometry is needed and thus the above statement is not true anymore.

2.2.2. CONTACT MODEL AND PARAMETERS

The liquid bridge contact model is based on a combination of an elastic-dissipative linear contact model for the normal repulsive force and a non-linear irreversible liquid bridge model for the non-contact adhesive force as described in [11]. The adhesive force is determined by three parameters; surface tension σ , contact angle θ which determine the maximum adhesive force and the liquid bridge volume V_b which determines the maximum interaction distance between the particles at the point of bridge rupture. The contact model parameters and particle properties are as given in Table 2.1. We have a polydisperse system of glass bead particles with mean diameter $d_p = \langle d \rangle = 2.2$ mm and a homogeneous size distribution ($d_{\min}/d_{\max} = 1/2$ of width $1 - \langle d \rangle^2 / \langle d^2 \rangle \approx 0.04$). Note that we neglect the additional viscous dissipation due to wet medium as proposed by Cruger et al. [51] since we mostly study the slow flows.

To study the effect of inertia and contact stiffness on the non-cohesive materials rheology, we compare our data for non-cohesive case with data from simulations of [1] for different gravity as given below:

$$g \in [1.0, 2.0, 5.0, 10.0, 20.0, 50.0] \text{ ms}^{-2}. \quad (2.1)$$

Table 2.1: Table showing the particle properties and constant contact model parameters.

Parameter	Symbol	Value
Sliding friction coefficient	μ_p	0.01
Normal contact stiffness	k	120 N m ⁻¹
Viscous damping coefficient	γ_o	0.5 × 10 ⁻³ kg s ⁻¹
Rotation frequency	Ω	0.01 s ⁻¹
Particle density	ρ	2000 kg m ⁻³
Gravity	g	9.81 m s ⁻²
Mean particle diameter	d_p	2.2 mm
Contact angle	θ	20°
Liquid bridge volume	V_b	75 nl

We also compare the effect of different rotation rates on the rheology for the following rotation rates:

$$\Omega \in [0.01, 0.02, 0.04, 0.10, 0.20, 0.50, 0.75, 1.00] \text{ rps.} \quad (2.2)$$

The liquid capillary force is estimated as stated in [13]. It is observed in our earlier studies [11] that the shear stress τ for high pressure can be described by a linear function of confining pressure, p , as $\tau = \mu_o p + c$. It was shown that the steady state cohesion c is a linear function of the surface tension of the liquid σ while its dependence on the volume of liquid bridges is defined by a cube root function. The friction coefficient μ_o is constant and matches the friction coefficient of dry flows excluding the small pressure limit. In order to see the effect of varying cohesive strength on the macroscopic rheology of wet materials, we vary the intensity of capillary force by varying the surface tension of the liquid σ , with a constant volume of liquid bridges ($V_b = 75$ nl) corresponding to a saturation of 8%, as follows:

$$\sigma \in [0.0, 0.01, 0.02, 0.04, 0.06, 0.10, 0.20, 0.30, 0.40, 0.50] \text{ N m}^{-1} \quad (2.3)$$

The first case, $\sigma = 0.0 \text{ N m}^{-1}$, represents the case of dry materials without cohesion, whereas $\sigma = 0.50 \text{ N m}^{-1}$ corresponds to the surface tension of a mercury-air interface. For $\sigma > 0.50 \text{ N m}^{-1}$, smooth, axisymmetric shear band formation is not observed and the materials agglomerate to form clusters as shown in Figure 2.2, for our particle size and density. Hence, σ is limited to maximum of 0.50 N m^{-1} .

2.2.3. AVERAGING METHODOLOGY

To extract the macroscopic properties, we use the spatial coarse-graining approach detailed in [31–33]. The averaging is performed over a grid of 47-by-47 toroidal volumes, over many snapshots of time assuming rotational invariance in the tangential ϕ -direction. The averaging procedure for a three-dimensional system is explained in [31, 33]. This spatial coarse-graining method was used earlier in [1, 30, 33, 50]. We do the temporal averaging of non-cohesive simulations over a larger time window from 80s to 440s to ensure the rheological models with enhanced quality data. All the other simulations are run for 200s and temporal averaging is done when the flow is in steady state, between 80s to 200s with 747 snapshots, thereby disregarding the transient behavior at the onset of the shear. In the critical state, the shear band is identified by the region having strain

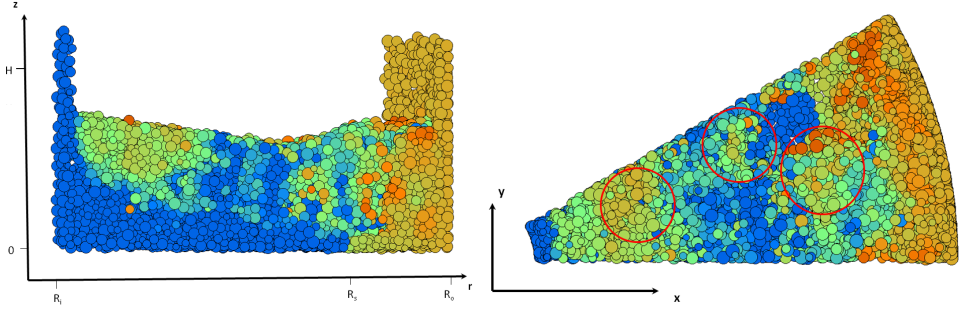


Figure 2.2: Cluster formation (shown by red circles) for highly cohesive materials ($\sigma = 0.70 \text{ N m}^{-1}$) a) front view and b) top view. Different colors blue, green and orange indicate low to high kinetic energy of particles respectively.

rates higher than 80% of the maximum strain rate at the corresponding height. Most of the analysis explained in the later sections are done from this critical state data at the center of the shear band.

MACROSCOPIC QUANTITIES

The general definitions of macroscopic quantities including stress and strain rate tensors are included in [1]. Here, we define the derived macroscopic quantities such as the friction coefficient and the redvisco-plasticity which are the major subjects of our study.

The local macroscopic friction coefficient is defined as the ratio of shear to normal stress and is defined as $\mu = \tau / p$.

The magnitude of strain rate tensor in cylindrical polar coordinates is simplified, assuming $u_r = 0$ and $u_z = 0$:

$$\dot{\gamma} = \frac{1}{2} \sqrt{\left(\frac{\partial u_\phi}{\partial r} - \frac{u_\phi}{r} \right)^2 + \left(\frac{\partial u_\phi}{\partial z} \right)^2} \quad (2.4)$$

The visco-plasticity is given by the ratio of the shear stress and strain rate as:

$$\eta = \frac{\tau}{\dot{\gamma}} = \frac{\mu p}{\dot{\gamma}}, \quad (2.5)$$

where $\dot{\gamma}$ is the strain rate; in a simple fluid, this would be viscosity, so that η in Eq. A.5 is also referred to as apparent viscosity [3].

2.2.4. CRITICAL STATE

We obtain the macroscopic quantities by temporal averaging as explained in Sec. 2.2.3. Next we analyze the data, neglecting data near walls ($r < r_{\min} \approx 0.045 \text{ m}$, $r > r_{\max} \approx 0.105 \text{ m}$, $z < z_{\min} \approx 0.004 \text{ m}$) and free surface ($z > z_{\max} \approx 0.035 \text{ m}$) as shown in Figure 2.3. Further, the consistency of the local averaged quantities also depends on whether the local data has achieved the critical state. The critical state is defined by the local shear accumulated over time under a constant pressure and constant shear rate condition. This state is reached after large enough shear, when the materials deform with applied strain

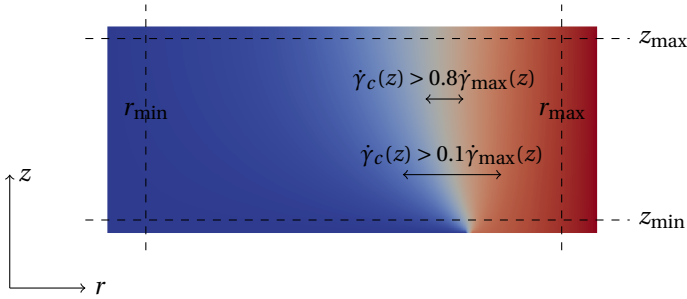


Figure 2.3: Flow profile in the $r - z$ plane with different colors indicating different velocities, with blue 0 m s^{-1} to red 0.007 m s^{-1} . The shear band is the pink and light blue area, while the arrows indicate 10 % and 80 % cut-off range of shear rate as specified in the text.

without any change in the local quantities, independent of the initial condition. We focus our attention in the region where the system can be considered to be in the critical state and thus has a well defined macroscopic friction. To determine the region in which the flow is in critical state, $\dot{\gamma}_{\max}(z)$ is defined to be the maximum strain rate for a given pressure, or a given height z . The critical state is achieved at a constant pressure and strain rate condition over regions with strain rate larger than the strain rate $0.1\dot{\gamma}_{\max}(z)$ as shown in Figure 2.3 corresponding to the region of shear band. While [1] showed that for rotation rate 0.01 rps, the shear band is well established above shear rate $\dot{\gamma} > 0.01 \text{ s}^{-1}$, of our analysis shown in the latter sections are in the shear band center is obtained by $\dot{\gamma} > 0.8\dot{\gamma}_{\max}(z)$ at different heights in the system. This is defined as the region where the local shear stress τ becomes independent of the local strain rate $\dot{\gamma}$ and τ/p becomes constant. We also extend our studies to the shear-rate dependence in critical state which is effective for critical state data for wider regions of shear band (Sec. 2.4.4). This shear rate dependence is analyzed in the regions of strain rate ($\dot{\gamma}$) larger than the $0.1\dot{\gamma}_{\max}(z)$ at a given height z . These data include the region from the center to the tail of the shear band, with typical cut-off factors $s_c = 0.8$ or 0.1 , respectively, as shown in Figure 2.3, and explained in Sec. 2.4.4.

2.3. TIME SCALES

Dimensional analysis is often used to define the characteristic time scales for different physical phenomena that the system involves. Even in a homogeneously deforming granular system, the deformation of individual grains is not homogeneous. Due to geometrical and local parametric constraints at grain scale, grains are not able to displace as affine continuum mechanics dictates they should. The flow or displacement of granular materials on the grain scale depends on the timescales for the local phenomena and interactions. Each time scale can be obtained by scaling the associated parameter with a combination of particle diameter d_p and material density ρ . While some of the time

scales are globally invariant, others are varying locally. The dynamics of the granular flow can be characterized based on different time scales depending on local and global variables. First, we define the time scale related to contact duration of particles which depends on the contact stiffness k as given by [1]:

$$t_k = \sqrt{\frac{\rho d_p^3}{k}}. \quad (2.6)$$

In the special case of a linear contact model, this is invariant and thus represents a global time scale too. Two other time scales are globally invariant, the cohesive time scale t_c , i.e. the time required for a single particle to traverse a length scale of $d_p/2$ under the action of an attractive capillary force and the gravitational time scale t_g , i.e. the elapsed time for a single particle to fall through half its diameter d_p under the influence of the gravitational force. The time scale t_c could vary locally depending on the local capillary force f_c . However, the capillary force is weakly affected by the liquid bridge volume while it strongly depends on the surface tension of the liquid σ . This leads to the cohesion time scale as a global parameter given by:

$$t_c = \sqrt{\frac{\rho d_p^4}{f_c}} \propto \sqrt{\frac{\rho d_p^3}{\sigma}}, \quad (2.7)$$

with surface tension σ and capillary force $f_c \approx \pi \sigma d_p$. The corresponding time scale due to gravity which is of significance under small confining stress close to the free surface is defined as:

$$t_g = \sqrt{\frac{d_p}{g}}. \quad (2.8)$$

The global time scales for granular flow are complemented by locally varying time scales. Granular materials subjected to strain undergo constant rearrangement and thus the contact network re-arranges (by extension and compression and by rotation) with a shear rate time scale related to the local strain rate field:

$$t_{\dot{\gamma}} = \frac{1}{\dot{\gamma}}. \quad (2.9)$$

Finally, the time for rearrangement of the particles under a certain pressure constraint is driven by the local pressure p . This microscopic local time scale based on pressure is:

$$t_p = d_p \sqrt{\frac{\rho}{p}}. \quad (2.10)$$

As the shear cell has an unconfined top surface, where the pressure vanishes, this time scale varies locally from very low (at the base) to very high (at the surface). Likewise, the strain rate is high in the shear band and low outside, so that also this time scale varies between low and high, respectively.

Dimensionless numbers in fluid and granular mechanics are a set of dimensionless quantities that have a dominant role in describing the flow behavior. These dimensionless numbers are often defined as the ratio of different time scales or forces, thus signifying the relative dominance of one phenomenon over another. In general, we expect

five time scales (t_g , t_p , t_c , t_γ and t_k) to influence the rheology of our system. Note that among the five time scales discussed here, there are ten possible dimensionless ratios of different time scales. We propose four of them that are sufficient to define the rheology that describes our results. Interestingly, all these four dimensionless ratios are based on the common time scale t_p . Thus, the time scale related to confining pressure is important in every aspect of the granular flow. All the relevant dimensionless numbers in our system are discussed in brief in the following two sections of this paper for the sake of completeness, even though not all are of equal significance.

2.4. RHEOLOGY OF DRY GRANULAR MATERIALS

2.4.1. EFFECT OF SOFTNESS IN THE BULK OF THE MATERIALS

We study here the effect of softness on macroscopic friction coefficient for different gravity in the system. Thus the pressure proportional to gravity is scaled in dimensionless form p^* [1] given by:

$$p^* = \frac{pd_p}{k}. \quad (2.11)$$

This can be interpreted as the square of the ratio of time scales, $p^* = t_k^2/t_p^2$, related to contact duration and pressure respectively. Figure 2.4 shows the macroscopic friction coefficient as a function of the dimensionless pressure p^* and the dashed line is given by:

$$\mu_p(p^*) = \mu_o f_p(p^*) \text{ with } f_p(p^*) = \left[1 - (p^*/p_o^*)^\beta\right], \quad (2.12)$$

where, $\beta \approx 0.50$, $\mu_o = 0.16$, $p_o^* \approx 0.90$. p_o^* denotes the limiting dimensionless pressure around the correction due to softness of the particles, where the correction is not applicable anymore, since $f_p \leq 0$ for $p^* \geq p_o^*$ [34]. We have used this fit, as our data range is too limited to derive the functional form of the fit. This is shown by the solid line in Figure 2.4 with the plotted data from our present simulation (\blacktriangleleft) and with data for different gravity in the system [1] which we use to describe other corrections for dry non-cohesive materials. Despite the deviation of data for different gravity from the trend for small p^* , the agreement with our data is reasonable. The dashed line represents the softness correction as proposed by [1]. The effect of softness is dominant in regions of large pressure where the pressure time scale t_p dominates over the stiffness time scale t_k and thus the data in plot are corresponding to higher than a critical pressure ($p_g^* > 4$, explained in Sec. 2.4.3). Here, the compressible forces dominate over the rolling and sliding forces on the particles, the flow being driven by squeeze. Thus, the macroscopic friction coefficient decreases with softness.

2.4.2. EFFECT OF INERTIAL NUMBER

For granular flows, the rheology is commonly described by the dimensionless inertial number [35]:

$$I = \dot{\gamma}d_p/\sqrt{p/\rho}, \quad (2.13)$$

which can be interpreted as the ratio of the time scales, t_p for particles to rearrange under pressure p , and the shear rate time scale t_γ for deformation due to shear flow, see Sec. 2.3. It has been shown both experimentally [35–37] and in simulations [38] that for

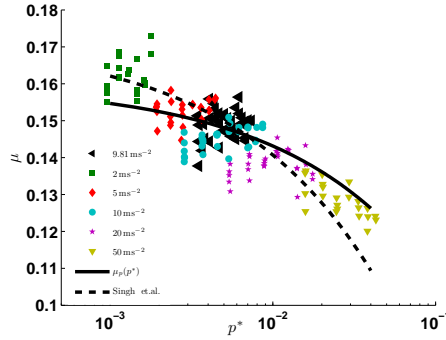


Figure 2.4: Local friction coefficient μ as a function of softness p^* for data with different gravity g [1] and our data (represented by \blacktriangleleft) for $p_g^* > 4$. The solid line represents the function $\mu_p(p^*)$ given by Eq. 2.12.

intermediate inertial numbers (in the range $I \leq I_o$), the macroscopic friction coefficient follow the so-called $\mu(I)$ rheology:

$$\mu_I(I) = \mu_o + (\mu_\infty - \mu_o) \frac{1}{1 + I_o/I}, \quad (2.14)$$

We assume the combined effect of softness and inertial number given as $\mu(p^*, I) = \mu_I(I) f_p$ and thus analyse μ/f_p as a function of I , see Figure 2.5. We compare our data for non-cohesive materials which is shown to be in agreement with the trend of data obtained from [1] for different external rotation rates. The black solid line corresponds to the data in the shear band center ($\dot{\gamma} > 0.8\dot{\gamma}_{\max}$) fitted by Eq. 2.14 with $\mu_o = 0.16$, $\mu_\infty = 0.40$ and $I_o = 0.07$ which are in close agreement with the fitting constants explained in [34]. Note that these fitting constants change with the range of I that are included in the fitting. Given that we do not have data for very high inertial number from our simulations, our present fit shows $I_o \approx 0.07$ and hence the fit is valid for $I \leq I_o$.

2.4.3. EFFECT OF GRAVITY CLOSE TO THE FREE SURFACE

In this section, we investigate the effect of the another dimensionless number p_g^* on local friction coefficient, given by:

$$p_g^* = \frac{p}{\rho d_p g}. \quad (2.15)$$

This can be interpreted as the square of the ratio of time scales, $p_g^* = t_g^2/t_p^2$, related to gravity and pressure respectively. The effect of inertial number and softness correction are eliminated by scaling μ by the correction factors μ_I and f_p respectively and studying the effect of p_g^* on the scaled friction coefficient. Figure 2.6 shows μ scaled by $\mu_I f_p$ as a function of dimensionless pressure p_g^* for different gravity g (different p^*) and different rotation rates Ω (different I), including our data for $g = 9.81 \text{ ms}^{-2}$ and $\Omega = 0.01 \text{ rps}$ which is also in agreement with other data set. The data for different slower rotation rates and different gravitational accelerations g agree well with our new data set, while the higher

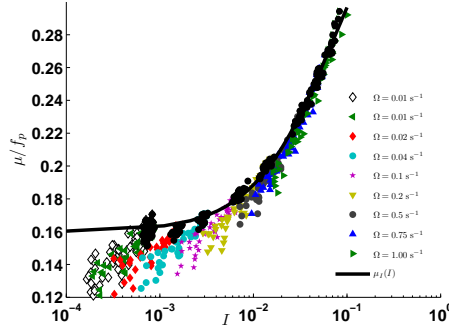


Figure 2.5: Local friction coefficient μ scaled by the softness correction f_p as a function of inertial number I . Different colors indicate different rotation rate Ω with our data represented by \diamond . Black circles represent the data in the center of the shear band ($\dot{\gamma} > 0.8\dot{\gamma}_{\max}$), other data are shown for $\dot{\gamma} > 0.1\dot{\gamma}_{\max}$. The solid line represents the function $\mu_I(I)$ given by Eq. 2.14.

rotation rates deviate. Note that the higher rotation rates are in a different regime where kinetic theory works and hence agreement with the generalized rheology is not expected strictly. All the data for different gravity and slower rotation rates collapse and these can be fitted by the solid line given by the correction $f_g(p_g^*)$ where:

$$\mu_g(p_g^*) = \mu_o f_g(p_g^*) \quad \text{with} \quad f_g(p_g^*) = \left[1 - a' \exp\left(-\frac{p_g^*}{p_{go}^*}\right) \right], \quad (2.16)$$

where, $a' \approx 0.71$ is the relative drop in friction coefficient at $p_g^* = 0$, $p_{go}^* \approx 1.19$ is the dimensionless pressure at which the friction coefficient drops below $0.74\mu_o$ and $f_g(p_g^*)$ is the correction corresponding to the dimensionless pressure p_g^* . Due to lack of confining stress close to the free surface ($p_g^* < 4$), the macroscopic friction coefficient exponentially decreases with decrease in p_g^* . Here, the gravity time scale t_g dominates over the pressure time scale t_p . Thus, while the effect of gravity close to the free surface is dominant for $p_g^* < 4$, $p_g^* \approx 4$ is the critical pressure above which the effect of softness p^* is significant as explained in Sec. 2.4.1.

2.4.4. SHEAR RATE DEPENDENCE IN CRITICAL STATE FLOW

After having quantified the dependence of the macroscopic friction on inertial number and softness, another correction was proposed in [1], taking into account a reduced, relaxed friction correction in very slow quasi-static flow. The same phenomena was addressed in [18, 31, 39] using non-local constitutive relations. Figure 2.7 is a representation of this correction $f_q(I)$ where:

$$\mu_q(I) = \mu_o f_q(I) \quad \text{with} \quad f_q(I) = \left[1 - \exp\left(-\left(\frac{I}{I^*}\right)^{\alpha_1}\right) \right], \quad (2.17)$$

where, $I^* = (4.85 \pm 1.08) \times 10^{-5}$ for very small inertial numbers ($I \leq I^*$) and $\alpha_1 = 0.48 \pm 0.07$. This correction is in inspiration with [31] where I^* scales linearly with the external

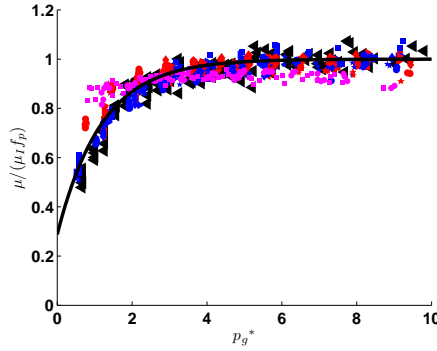


Figure 2.6: Local friction coefficient μ scaled by softness correction f_p and the inertial number correction μ_I as a function of dimensionless pressure p_g^* for data with different gravity g . Blue markers indicate different g with legends given in Figure 2.4, red markers indicate different slower rotation rates $\Omega \leq 0.5$ and magenta markers indicate faster rotation rates $\Omega > 0.5$ rps. Different marker shapes denote different rotation rates, as labelled in Figure 2.5, with the new simulation data ($\Omega = 0.01$ rps) represented by \blacktriangleleft . The solid line represents the function $f_g(p_g^*)$ given by Eq. 2.16.

shear rate and thus is proportional to the local strain-rate and the granular temperature. Although the data represented in Figure 2.7 (black \diamond and red \circ) include $\dot{\gamma}_c(z) > 0.1\dot{\gamma}_{\max}(z)$, the fitted solid line given by $f_q(I)$ correction corresponds to data in the shear band center as well as outside center (for $\dot{\gamma}_c(z) > 0.1\dot{\gamma}_{\max}(z)$) which are all in the critical state. Typically, we study the local effect for data inside the shear band center ($\dot{\gamma}_c(z) > 0.8\dot{\gamma}_{\max}(z)$) which corresponds to the data given by red \circ which are invariant to the effect of small inertial number which allows us to assume $f_q(I) \approx 1.0$. Hence, in the following sections, we do not take into consideration the correction $f_q(I)$, though we mention it.

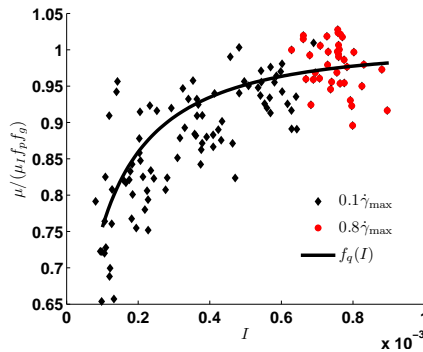


Figure 2.7: Local friction coefficient μ scaled by correction factors f_p , f_g and μ_I as a function of inertial number I for dry non-cohesive materials with data for $p^* > 0.003$. The solid line represents the function $f_q(I)$ given by Eq. 2.17.

2.5. RHEOLOGY OF WET-COHESIVE GRANULAR MATERIALS

2.5.1. BOND NUMBER

The Bond number (Bo) is a measure of the strength of the adhesive force relative to the compressive force. A low value of Bo (typically much less than 1) indicates that the system is relatively unaffected by the attractive forces; high Bo indicates that the attractive force dominates in the system. Thus Bo is a critical microscopic parameter that controls the macroscopic local rheology of the system. While the conventional way of defining the Bond number as the ratio of the time scales t_c and t_g [19] is appropriate for single particles, or close to the free surface, we define the local Bond number relative to the confining force:

$$Bo(p) = \frac{f_c^{\max}}{p d_p^2}, \quad (2.18)$$

defined as the square of the ratio between timescales related to pressure t_p and wetting time scale t_c . $f_c^{\max} = 2\pi r \sigma \cos\theta$ is the maximum capillary force between a pair of particles, where r is the effective radius of the interacting pair of particles. This provides an estimate of the local cohesion intensity by comparing the maximum capillary pressure allowed by the contact model f_c^{\max}/d_p^2 with the local pressure. A low to high transition of local Bond number from the bottom of the shear cell to the free surface is as a result of the change in time scale related to pressure t_p from $t_p \ll t_c$ to $t_p \gg t_c$ respectively. Subsequently, we define the global Bond number Bo_g as a measure of the strength of cohesion in the system as:

$$Bo_g = \frac{f_c^{\max}}{p^{\text{mean}} d_p^2}, \quad (2.19)$$

where, p^{mean} is the mean pressure in the system. This is an experimentally measurable quantity and is related to quantifying the system as a whole. The global Bond number corresponding to surface tension of liquid defined in Eq. 2.3 is given by:

$$Bo_g \in [0.0, 0.06, 0.12, 0.24, 0.36, 0.60, 1.28, 1.94, 2.54, 3.46] \quad (2.20)$$

EFFECT OF LOCAL BOND NUMBER

The properties of the particles and the interstitial fluid strongly affect the macroscopic behavior of granular materials. The local macroscopic friction is studied as a function of local Bond number Bo for different wet cohesion intensity. Figure 2.8 shows the macroscopic friction coefficient as a function of the local Bond number Bo for different wet cohesion. It is evident that the friction coefficient increases with local Bond number with a constant value μ_o in the low Bond number limit. For frictionless wet cohesive materials, the rheology can be defined by a linear fitting function given by:

$$\mu_c(Bo) = \mu_o f_c(Bo) \quad \text{with} \quad f_c(Bo) = (1 + aBo), \quad (2.21)$$

where, $\mu_o = 0.15$ is the macroscopic friction coefficient in the high pressure limit [11] and $a \approx 1.47$. This is shown by the solid line in Figure 2.8. However, it is observed that the data deviate from the solid fitting line in the high Bond number or low pressure limit. This deviation is explained by the small pressure correction $f_g(p_g^*)$ as explained in Sec. 2.4.3 and discussed in details in the next section.

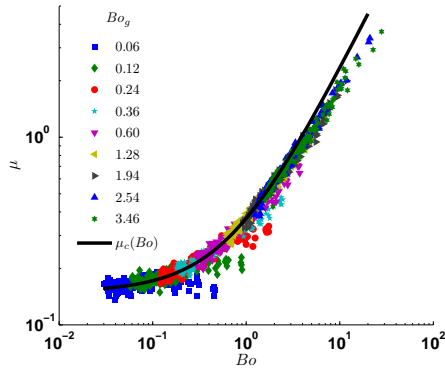


Figure 2.8: Local friction coefficient μ as a function of the local Bond number Bo for wet cohesive materials. The solid line represents the function $\mu_c(Bo)$ given by Eq. 2.21.

2.5.2. EFFECT OF GRAVITY CLOSE TO THE FREE SURFACE

This section is an extension of the effect of gravity close to free surface explained in Sec. 2.4.3. Figure 2.6 shows the dependence of the local friction coefficient on the local scaled pressure p_g^* for dry non-cohesive materials and this effect is small in the high pressure limit. With an attempt to separate the effect of Bond number on the rheology of cohesive materials, we plot the local friction coefficient μ scaled by the Bond number correction f_c and other corrections μ_I and f_p , as a function of scaled pressure p_g^* as shown in Figure 2.9. The solid line is given by Eq. 2.16, where the non-cohesive function fits for the wet data as well.

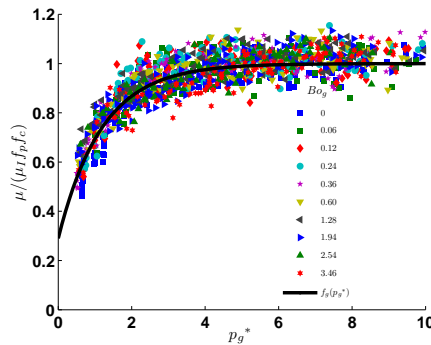


Figure 2.9: $\mu / (\mu_I f_p f_c)$ as a function of dimensionless pressure p_g^* for different global Bond number. The solid line represents the function given by Eq. 2.16.

2.6. RHEOLOGICAL MODEL

We studied the rheology of dry and wet granular materials in terms of different dimensionless numbers and the trends are combined and shown to collectively contribute to the rheology as multiplicative functions given by:

$$\mu(I, p^*, p_g^*, Bo) = \mu_I(I) f_g(p_g^*) f_q(I) f_c(Bo) f_p(p^*). \quad (2.22)$$

Thus, a general(ized) multiplicative rheology function is proposed for the macroscopic friction coefficient, dependent on four dimensionless numbers p^* , p_g^* , I , Bo .

This rheological model is based on constant liquid bridge volume at all contacts and we do not take into account liquid redistribution among contacts [14, 15]. This is a simplified approach to establish the generalised rheology and we are working further on liquid redistribution and will analyse its effect on the rheology. However, the cohesion time scale is only weakly affected by the liquid bridge volume and mainly depends on the surface tension of the liquid. Preliminary results using a liquid redistribution model show that in this state, 40% of the contacts in the shear band center become dry, resulting in a higher probability of dry contacts with micro-contact local Bond number $Bo = 0$. This results in a lower local Bond number in the shear band center. Our present rheological model is shown to be valid for a wide range of Bond number and thus use of a liquid redistribution model is expected to shift data further, towards the lower Bond numbers but is expected to follow the same trends.

For a full constitutive law, one also needs to take into account the solid volume fraction also. For dry granular shear flow [1, 34], the constitutive relations for the volume fraction given by corrections (to first order) based on dimensionless numbers p^* and I as follows:

$$\phi(I, p^*) = \phi_c \left(1 + \frac{p^*}{p_c^*}\right) \left(1 - \frac{I}{I_c}\right), \quad (2.23)$$

where, $\phi_c \approx 0.65$ is the critical or the steady state density under shear, in the limit of vanishing pressure and inertial number. $I_c = 0.85$ is the inertial number corresponding to strain rate when the dilation turns to fluidization. $p_c^* = 0.33$ is the typical pressure for which softness leads to huge densities. Though the volume fraction in an inhomogeneous system is a field (fluctuating around a mean value), its local values are captured by the above equation in terms of the local dimensionless numbers. The above relation shows that the volume fraction decreases (and the friction increases) when the quasi-static regime is exceeded. However, the generalised rheology is expected to be valid everywhere in the inhomogeneous system where the system has been sheared long enough to reach the critical state, irrespective of their different volume fraction. The volume fraction increases with increase in confining stress as shown in [1, 34]. In Chapter 4, we show that the volume fraction remains constant (weakly decreasing) for small Bo and increases linearly (approximately) with higher Bo . When looking closer, one observes that the volume fraction only slightly decreases with decrease in Bo , in contrary to the results of [40], where the volume fraction strongly decreases with cohesion (or inverse of confining stress) in the quasi-static regime. Note that we have very weak friction and no rolling resistance in our system which explains the insignificant effect of confining stress on volume fraction. Stable, loose microstructures require both of these mechanisms to

be active to show considerable effect. For completeness, our goal being to define the rheology of granular materials in a continuum framework and thus overall constitutive relations mentioned above are to implemented in continuum solvers. Appendix A summarizes the implementation of the constitutive relation in the continuum solver for dry non-cohesive granular materials.

2.7. LOCAL VISCO-PLASTICITY

Visco-plasticity is characterized by a yield stress, below which the materials will not deform, and above which they will deform and flow according to different constitutive relations. Visco-plastic models include many fluid models like the Bingham plastic, the Herschel Bulkley model and the Casson model. Granular fluid, being a classification of the Bingham plastic fluid with a pressure dependent viscosity. However, unsaturated granular materials, being heterogeneous systems, the term viscosity is not relevant in real sense though mentioned about effective viscosity in [3]. Thus we introduce viscoplasticity of granular materials as a substitute term. We introduce the local visco-plasticity η of granular materials which is the ratio of the shear stress to the shear rate as an alternative to μ . To see the combined effect of pressure and strain rate on the local visco-plasticity, we analyse them as functions of the inertial number. For a given pressure, the inertial number is proportional to the shear rate. Thus, the analysis of local visco-plasticity as a function of the inertial number for small pressure ranges can be interpreted as the analysis of visco-plasticity vs strain rate. We define the dimensionless local visco-plasticity as:

$$\eta^* = \frac{\eta}{\sqrt{d_p k \rho}} = \frac{\mu p / \dot{\gamma}}{\sqrt{d_p k \rho}} = \frac{\mu \sqrt{p^*}}{I} \quad (2.24)$$

Since we here focus on the data in the center of the shear band, the dependence on shear rate in the critical state flow which includes data outside the shear band center can be neglected ($f_q(I \geq I^*) \approx 1$) and thus the rheological model for the local friction coefficient given by Eq. 2.22 is simplified by:

$$\mu(p^*, p_g^*, Bo) = \mu_I(I) f_g(p_g^*) f_c(Bo) f_p(p^*). \quad (2.25)$$

The dimensionless variable η^* can be related to three time scales namely, contact duration t_k , strain rate related time scale $t_{\dot{\gamma}}$ and pressure related time scale t_p as $\eta^* = \mu t_{\dot{\gamma}} t_k / t_p^2$.

Alternatively, the flow rules of granular materials can be approximated as that of a power-law fluid with inertial number inversely proportional to shear rate as given by:

$$\eta^* = K I^{\alpha-1}, \quad (2.26)$$

where, $K = \mu \sqrt{p^*} I^{-\alpha}$ is the flow consistency and α is the flow behavior index. The flow rules of granular materials are pretty straightforward at high pressures with $\alpha \approx 0$. However, deviations are observed from the power-law behavior at small pressures. More details on the flow rules at large and small pressure are explained in Sec. 2.7.1 and 2.7.1 respectively.

Figure 2.10 shows the local visco-plasticity η^* as a function of the inertial number I for different global Bond numbers. The data shown correspond to all the data close to the shear band center for different heights. The inertial number is lowest at an intermediate height, and increases towards surface and base. With increasing inertial number, the visco-plasticity decreases, indicating that granular materials flow like non-Newtonian fluids, specifically shear-thinning fluids. It is also evident from the figure that the flow behavior is different at large and small confining pressure.

2.7.1. PREDICTION OF LOCAL VISCO-PLASTICITY

PREDICTION OF STRAIN RATE

Various numerical and experimental results suggest the presence of shear bands in granular materials subjected to relative motion [41, 42]. Often this shear band is considered as a thin layer of localized strain rate, separating rigid blocks of constant velocity. Investigations on the shear band formation reveal that its characteristics are influenced by a number of factors including density, confining pressure, particle size and shape, friction, anisotropy of the material and cohesion [42, 50]. The shear band thickness and the distance from the center decrease as the confining pressure increases [43]. Constitutive relations exist for many shear band properties [44], which suggests a pathway to finding analytical solutions.

In this section, we discuss an analytical approach to get stress and strain rate correlations from the physics of granular materials and compare our analytical solution with the numerical results for different wet cohesion using the generalized μ function for the macroscopic friction, see Eq. 2.22 and 2.25. The magnitude of the strain rate is given by Eq. 2.4. It is assumed that the velocity component u_ϕ is slowly varying in z -direction ($\partial u_\phi / \partial z \approx 13\%$ of $(\partial u_\phi / \partial r - u_\phi / r)$ in the shear band center), so $\partial u_\phi / \partial z$ is small (by one order of magnitude) and is neglected with an approximation, so that

$$\dot{\gamma} \approx \frac{1}{2} \left(\frac{\partial u_\phi}{\partial r} - \frac{u_\phi}{r} \right). \quad (2.27)$$

In the shear band region, the non-dimensionalized angular velocity profile $\omega = u_\phi / (2\pi r \Omega)$ at every height can be well approximated by an error function [45–48]:

$$\omega = A + \text{Berf} \left(\frac{r - R_c}{W} \right), \quad (2.28)$$

where $A \approx B \approx 0.5$, W and R_c are the width and the position of the shear band, respectively at different heights. Most surprising is the fact that the fit works equally well for a wide range of I , p^* , Bo etc. [50]. Eq. 2.28 substituted in Eq. 2.27 can be simplified as a first order expansion of the derivative of the error function as:

$$\dot{\gamma} = \frac{\sqrt{\pi} r \Omega}{W} \exp \left[- \left[\frac{r - R_c}{W} \right]^2 \right]. \quad (2.29)$$

The shear rate at the center of the shear band ($r = R_c$) is thus given as:

$$\dot{\gamma}_{\max} = \frac{\sqrt{\pi} R_c \Omega}{W}. \quad (2.30)$$

The pressure for the given geometry is increasing linearly from the free surface, *i.e.* varies hydrostatically with the depth inside the material. Further, we obtain the non-dimensional inertial number from the predicted strain rate and pressure, so that

$$I_{\max} = \frac{\dot{\gamma}_{\max} d_p}{\sqrt{p/\rho}} \propto \frac{\dot{\gamma}_{\max} d_p}{\sqrt{H-z}}, \quad (2.31)$$

ignoring the small variations in the bulk density.

PREDICTION OF VISCO-PLASTICITY OF MATERIALS UNDER LARGE PRESSURE

The predicted local visco-plasticity from Eqs. 2.24 and (2.25) can be simplified with $f_g(p_g^*) \approx 1$ under large pressure, $\mu_I(I) \approx \mu_o$ for quasistatic states and $f_p(p^*) \approx 1$ for the relatively stiff particles ($0.002 < p^* < 0.01$) studied in our system and thus can be written as:

$$\eta^* = \frac{\mu_o \sqrt{p^*}}{I} \left[1 + aBo \right]. \quad (2.32)$$

For dry non-cohesive materials, $Bo = 0$ and $\sqrt{p^*}$ is slowly changing at high pressure. For wet cohesive materials, the magnitude of visco-plasticity is thus determined by the term $f_c(Bo)$. However, the flow behavior index for wet materials is also constant under high confining pressure for the same reason as stated for dry materials as $Bo \propto 1/p$. Table 2.2 shows the value of the index $\alpha - 1$ for different Bo_g . Under high confining pressure, α is independent of cohesion and $\alpha \approx 0$, $\alpha - 1$ corresponding to the slope of the red dash-dotted lines in Figure 2.10. Thus, $\eta^* \propto I^{-1}$ and $\alpha \approx 0$ confirms that both dry and wet granular materials behave like a power law fluid under large confining pressure.

Table 2.2: Table showing the flow behavior index under large pressure constraint (red dash-dotted lines fitted to Figure 2.10)

Bo_g	0.0	0.06	0.12	0.24	0.36	0.60	1.28	1.94	2.54	3.46
$\alpha - 1$	-0.94	-0.81	-0.92	-0.82	-0.89	-1.00	-0.93	-1.10	-1.23	-1.09

PREDICTION OF VISCO-PLASTICITY OF MATERIALS UNDER SMALL PRESSURE

Wet cohesive materials confined to small pressure near the surface show more interesting behavior. Here, the pressure and strain rate are very small, *i.e.* large t_p and $t_{\dot{\gamma}}$ make confining pressure and strain rate less dominant, so that t_g and t_c are the two interacting time scales. The rheology is now strongly dependent on the corrections $f_g(p_g^*)$ and $f_c(Bo)$ but not on the correction $f_p(p^*) \approx 1$ ($p^* < 0.005$) under small confining pressure. The strain rate close to the center of the shear band and free surface is almost constant since the shear band is wide so that $f_q \approx 1$ while $\mu_I \approx \mu_o$. We use this simplified constant strain rate to predict the visco-plasticity near the surface of the shear cell where the pressure is very small. The visco-plasticity for wet cohesive materials confined to small pressure is more intricate and is predicted by from Eqs. 2.24 and (2.25) with $f_p(p^*) \approx 1$ as:

$$\eta^* = \frac{\mu_o \sqrt{p^*}}{I} \left[1 + aBo \right] \left[1 - a' \exp\left(-\frac{p_g^*}{p_{go}^*}\right) \right]. \quad (2.33)$$

Figure 2.10 shows the prediction of visco-plasticity at small pressure as given by the green solid lines. Non-cohesive materials upto weakly cohesive materials ($Bo_g < 0.60$), at low pressure, are less viscous than those at high pressure, as shown in the figure. For global Bond number $Bo_g = 0.60$, materials for a given inertial number have the same visco-plasticity independent of pressure. For even higher cohesion ($Bo_g > 0.60$), the flow behavior changes qualitatively. Though, the visco-plasticity decreases with the inertial number ($\eta^* \propto I^{-\delta}$), even for cohesive materials, the qualitative decay power δ decreases towards zero ($\delta \rightarrow 0$). For a given inertial number, the material near the surface has higher visco-plasticity than in the bulk and at the base. Materials confined by small pressure become reduced shear thinning with increase in cohesion. This is represented by the direction of black arrows marked with Bo_g in Figure 2.10. Thus, granular materials have different shear-thinning properties depending on the local confining pressure and Bond number.

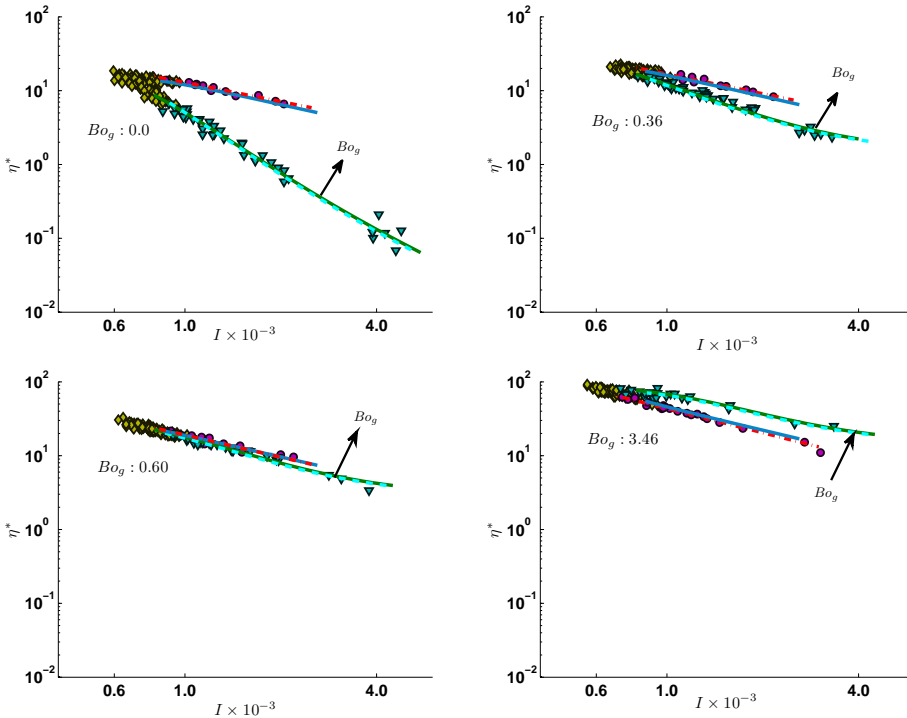


Figure 2.10: Local visco-plasticity η^* as a function of inertial number I for different global Bond number Bo_g . Different symbols represent data for different pressure, ∇ : $p^* \geq 0.006$, \diamond : $0.002 < p^* < 0.006$ and \circ : $p^* \leq 0.002$. The lines (dash-dotted red) and (solid green) are the fittings and the predictions obtained for $p^* \geq 0.006$ and $p^* \leq 0.002$ respectively. The lines (solid blue) and (dashed cyan) are the predictions obtained from the analytical solutions for $p^* \geq 0.006$ and $p^* \leq 0.002$ respectively.

ANALYTICAL PREDICTION OF VISCO-PLASTICITY

We extract the position and the width of the shear band R_c and W respectively from the fit function in Eq. 2.28. Both position and width of the shear band depend on the height in the system and the position moves inwards with increasing height (decreasing pressure). Predictions of the position of the shear band center as a function of height is given in [49]. Since the analytical prediction discussed here is not significantly affected by this varying position of the shear band, we use the mean shear band position \bar{R}_c for our prediction. The shear band moves inward with increase in global Bond number [50]. Thus the mean shear band position \bar{R}_c decreases with increasing Bo_g (not shown here).

The width of the shear band is predicted as function of height as given by [44]:

$$W(z) = W_{\text{top}} \left[1 - \left(1 - \frac{z}{H} \right)^2 \right]^\beta, \quad (2.34)$$

where $\beta = 0.6$ for non-cohesive materials and $0.5 < \beta < 0.7$ for cohesive materials are fitted well by our data. Assuming the pressure varying hydrostatically and the bulk density as $\rho_b = 0.6\rho$, we translate Eq. 2.34 to W as a function of p . Substituting Eqs. 2.30 and 2.34 in Eq. 2.31 and rearranging, we get the inertial number I_{max} in the shear band center as a function of the local pressure p . Further, by substituting p , we get η_{max}^* in the shear band center and thus obtain a quantitatively accurate prediction of η_{max}^* (I_{max}), plotted as blue solid lines and cyan dashed lines in Figure 2.10.

The results show that the analytical solution is in good agreement with our numerical results. Focusing on the slope of the small pressure line, we observe that it changes with increasing cohesion in the same way as shown by numerical data. It is observed from the analytical solution that this change in slope is governed by μ . Thus, the shear-thinning rate for materials under small pressure depends on local friction coefficient, which depends on the corrections $f_g(p_g^*)$ and $f_c(Bo)$.

2.7.2. ELIMINATING THE EFFECT OF COHESION AND GRAVITY

Under larger confining pressure (as stated in Sec. 2.7.1), with increase in cohesion, the visco-plasticity of the granular fluid increases, however, the flow behavior remains qualitatively the same even for very high cohesion. For materials confined to large pressure, where \sqrt{p} is slowly varying, the visco-plasticity is inversely proportional to the strain rate and approximately also to the inertial number. At smaller pressure, the materials are more free only under the effect of gravity, with less dominant forces due to particle contacts. Therefore, cohesion is relatively more dominant for higher local Bond numbers, resulting in the qualitative change in shear thinning rate (α). Thus the flow of materials is affected by both dimensionless numbers Bo and p_g^* at the same time. Then, the granular fluid appears to no longer behave like a power-law fluid. Several of these rheological correction factors make the flow behavior even more non-linear under small pressure. In order to see the rheology of the granular fluid under small pressure, which is devoid of the effect of these dimensionless numbers, we rescale the local dimensionless visco-plasticity η^* by $f_c(Bo)$ and $f_g(p_g^*)$ and analyse it as a function of inertial number. Figure 2.11(a) shows the dimensionless visco-plasticity η^* scaled by $f_c(Bo)$ as a function of inertial number for different cohesion. All the data for different cohesion collapse to a single plot for the triad of different pressure scales. Further, we rescale $\eta^*/f_c(Bo)$ by

$f_g(p_g^*)$ and plot it as a function of inertial number for different cohesion as shown in Figure 2.11(b). The fitted solid line corresponding to the data at large pressure is given by Eq. 2.26 with $\alpha = 0$ and $K \approx 0.01$. Furthermore, the fitted dashed line corresponding to the data at small pressure is given by Eq. 2.26 with $\alpha = -1$ and $K \approx 5.6 \times 10^{-6}$. This is explained theoretically by substituting p^* in Eq. 2.13 and using Eq. 2.33 with constant friction coefficient μ_0 yielding:

$$\frac{\eta^*}{f_c(B_0)f_g(p_g^*)} = \frac{\mu_0 \dot{\gamma} d_p^{3/2}}{I^2} \sqrt{\frac{\rho}{k}}, \quad (2.35)$$

Thus, for slowly varying strain rate at small pressure, η^* is proportional to I^{-2} and is represented by Eq. 2.26 with $\alpha = -1$. This eventually explains the earlier observations by [32].

Thus, the flow behavior for granular materials in a simple hypothetical case with high confining stress constant friction coefficient can be approximated by that of a power-law fluid flow behavior. However, for more realistic systems, e.g., unit operations at low stress, several other factors influence the flow rheology, e.g., near to the free surface. Thus, under small pressure, granular materials behave more interestingly and complex than a power-law fluid.

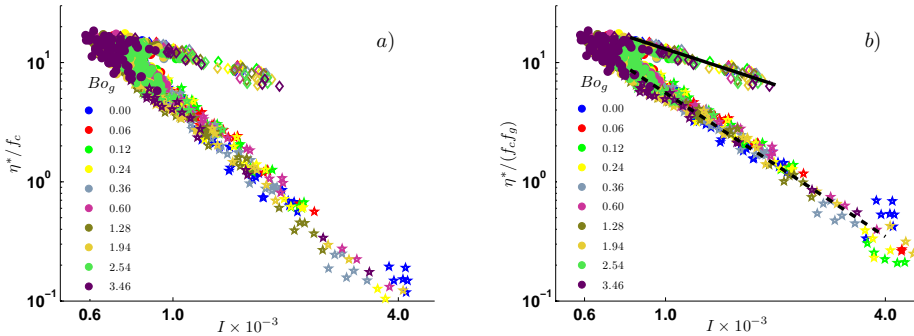


Figure 2.11: a) Dimensionless local visco-plasticity η^* scaled by the Bond number correction f_c as a function of the inertial number I . b) Dimensionless local visco-plasticity η^* scaled by the Bond number correction f_c and small pressure correction f_g as a function of the inertial number I . Different symbols represent data for different pressure, \diamond : $p^* \geq 0.006$, \bullet : $0.002 < p^* < 0.006$ and \star : $p^* \leq 0.002$ respectively. The fitted solid and dashed lines for large and small pressure are given by Eq. 2.26 with $\alpha = 0$ and $\alpha = -1$ respectively.

2.8. DISCUSSIONS AND CONCLUSIONS

The rheology of dry as well as wet granular materials (in the pendular regime) has been studied by simulations using the discrete element method in steady state shear. Our results show that the conventional $\mu(I)$ rheology must be modified to take into account other factors such as cohesion, contact softness, corrections at small pressures where gravity dominates, and a generalised inertial number dependence for very slow quasi-static flow (creep) in the tails of the shear bands. The trends are combined and shown

to collectively contribute to the rheology as multiplicative functions, *i.e.* ignoring one contribution can lead to inconsistent results. This new generalized rheological model applies to a wide range of parameters from dry non-cohesive to strongly cohesive materials, and contains also both the small and the large pressure limits. Note that additional contributions from viscous forces should be included in case of rapid flow. Our ongoing work shows that the generalised rheology is independent of system configuration, pressure or volume control, in the critical state and is applicable for both homogeneous simple shear and inhomogeneous systems like the split bottom shear cell. Given this is justified, the shear thinning behavior for granular materials is valid for every locally reached critical state, irrespective of the system configuration in moderate to low pressure and dense regime.

Furthermore, we study the visco-plasticity as a function of inertial number for granular fluids of varying cohesive strength. Most strikingly, the cohesive strength not only increases the magnitude of the visco-plasticity, but also decreases the shear thinning rate, but only for material under small confining pressure *e.g.* close to the free surface. This variable shear thinning behavior of granular materials under low stress, close to a free surface, is attributed to the higher local Bond number *i.e.* it is a low pressure effect. Thus, the flow rheology (friction and visco-plasticity) is predicted by the proposed rheology model for dry and wet granular materials under both low and high confining stress. Further, we develop an analytical solution for the visco-plasticity using the proposed rheology (with some simplifications) and show that the results are in good agreement with our numerical analysis. Materials become reduced shear thinning with an increase in cohesion at high Bond numbers under small confining pressure.

Finally, it is shown that the effect of each of the dimensionless numbers can be eliminated by rescaling, and thus the visco-plasticity of a simple system with a (small) constant friction coefficient is predicted as that of a power-law fluid.

As an outlook, we aim to implement the generalized rheological model in a continuum description of the split-bottom shear cell geometry. A successful implementation is only the first step for validation and paves the way to use this rheological model in industrial applications for material flow descriptions. We aim to also include the higher order effect of the Bond number in the generalized rheology. We included the small pressure (free surface) correction in the rheology, as an effect of gravity. It is to be noted that even in a micro-gravity system, both pressure and gravity change identically and thus the corresponding correction term remains the same as in a system with high gravity. Thus this correction corresponds to an effect active at interfaces or at the free-surface. Next step is to perform the micro-structural analysis also for our system [50] and in particular close to the free surface in order to understand the change in shear thinning rate. Another open question concerns the creep correction and its relation to the micro-structure and granular temperature. Last, the present rheology has to be merged to kinetic theory in the rapid, collisional flow regime [6], which presents an open challenge.

REFERENCES

- [1] A. Singh, V. Magnanimo, K. Saitoh, and S. Luding, *New Journal of Physics* **17**, 043028 (2015).

- [2] A. Thornton, T. Weinhart, S. Luding, and O. Bokhove, *The European Physical Journal E* **35**, 1 (2012).
- [3] S. Roy, S. Luding, and T. Weinhart, *New Journal of Physics* **19**, 043014 (2017).
- [4] A. Thornton, T. Weinhart, V. Ogarko, and S. Luding, *Computer Methods in Materials Science* **13**, 1 (2013).
- [5] T. Weinhart, R. Hartkamp, A. Thornton, and S. Luding, *Physics of Fluids* **25**, 070605 (2013).
- [6] D. Vescovi and S. Luding, *Soft Matter* **12**, 8616 (2016).
- [7] C. Bonnoit, J. Lanuza, A. Lindner, and E. Clement, *Physical Review Letters* **105**, 108302 (2010).
- [8] N. Huang, and D. Bonn, *Journal of Fluid Mechanics* **590**, 497 (2007).
- [9] N. Huang, G. Ovarlez, F. Bertrand, S. Rodts, P. Coussot, and D. Bonn, *Physical Review Letters* **94**, 28301 (2005).
- [10] A. Lemaître, J. N. Roux, and F. Chevoir, *Rheologica Acta* **48**, 925 (2009).
- [11] S. Roy, A. Singh, S. Luding, and T. Weinhart, *Computational Particle Mechanics* **3**, 449 (2015).
- [12] R. Schwarze, A. Gladkyy, F. Uhlig, and S. Luding, *Granular Matter* **15**, 455 (2013).
- [13] C. D. Willett, M. J. Adams, S. A. Johnson, and J. Seville, *Langmuir* **16**, 9396 (2000).
- [14] R. Mani, D. Kadau, D. Or, and H. J. Herrmann, *Physical Review Letters* **109**, 248001 (2012).
- [15] M. Scheel, R. Seemann, M. Brinkmann, M. Di Michiel, A. Sheppard, and S. Herminghaus, *Journal of Physics: Condensed Matter* **20**, 494236 (2008).
- [16] N. Berger, E. Azéma, J. F. Douce, and F. Radjai, *Europhysics Letters* **112**, 64004 (2016).
- [17] Y. Gu, S. Chialvo, and S. Sundaresan, *Physical Review E* **90**, 032206 (2014).
- [18] G. Koval, J. N. Roux, A. Corfdir, and F. Chevoir, *Physical Review E* **79**, 21306 (2009).
- [19] M. E. Weber, R. Clift, and J. R. Grace, *Bubbles, drops, and particles* (Academic Press, 1978).
- [20] N. J. Wagner and J. F. Brady, *Physics Today* **62**, 27 (2009).
- [21] N. Y. C. Lin, B. M. Guy, M. Hermes, C. Ness, J. Sun, W. C. K. Poon, and I. Cohen, *Physical Review Letters* **115**, 228304 (2015).
- [22] A. Fall, F. Bertrand, G. Ovarlez, and D. Bonn, *Journal of Rheology* **56**, 575 (2012).

- [23] A. Fall, F. Bertrand, D. Hautemayou, C. Mezière, P. Moucheron, A. Lemaitre, and G. Ovarlez, *Physical Review Letters* **114**, 098301 (2015).
- [24] R. Mari, R. Seto, J. F. Morris, and M. M. Denn, *Proceedings of the National Academy of Sciences* **112**, 15326 (2015).
- [25] A. Thornton, T. Weinhart, S. Luding, and O. Bokhove, *International Journal of Modern Physics C* **23**, 124001 (2012).
- [26] T. Weinhart, A. Thornton, S. Luding, and O. Bokhove, *Granular Matter* **14**, 289 (2012).
- [27] S. Schöllmann, *Physical Review E* **59**, 889 (1999).
- [28] X. Wang, H. P. Zhu, and A. B. Yu, *Granular Matter* **14**, 411 (2012).
- [29] E. Woldhuis, B. P. Tighe, and W. Saarloos, *The European Physical Journal E: Soft Matter and Biological Physics* **28**, 73 (2009).
- [30] S. Roy, S. Luding, and T. Weinhart, *Procedia Engineering* **102**, 1531 (2015).
- [31] S. Luding, *Particuology* **6**, 501 (2008).
- [32] S. Luding, *Particulate Science and Technology* **26**, 33 (2008).
- [33] S. Luding and F. Alonso-Marroquin, *Granular Matter* **13**, 109 (2011).
- [34] S. Luding, A. Singh, S. Roy, D. Vescovi, T. Weinhart, and V. Magnanimo, in *Proceedings of the 7th International Conference on Discrete Element Methods* (Springer, 2016) pp. 13–19.
- [35] G. D. R. MiDi, *The European Physical Journal E* **14**, 341 (2004).
- [36] Y. Forterre and O. Pouliquen, *Annual Review of Fluid Mechanics* **40**, 1 (2008).
- [37] P. Jop, Y. Forterre, and O. Pouliquen, *Nature* **441**, 727 (2006).
- [38] O. Pouliquen, C. Cassar, P. Jop, Y. Forterre, and M. Nicolas, *Journal of Statistical Mechanics: Theory and Experiment* **2006**, P07020 (2006).
- [39] K. Kamrin and G. Koval, *Physical Review Letters* **108**, 178301 (2012).
- [40] S. Khamseh, J. N. Roux, and F. Chevoir, *Physical Review E* **92**, 022201 (2015).
- [41] D. Fenistein and M. van Hecke, *Nature* **425**, 256 (2003).
- [42] D. L. Henann and K. Kamrin, *Proceedings of the National Academy of Sciences* **110**, 6730 (2013).
- [43] M. Bolton, *Géotechnique* **37**, 219 (1986).
- [44] A. Ries, D. E. Wolf, and T. Unger, *Physical Review E* **76**, 051301 (2007).

- [45] S. Cohen-Addad, R. Höhler, and O. Pitois, *Annual Review of Fluid Mechanics* **45**, 241 (2013).
- [46] J. A. Dijksman and M. van Hecke, *Soft Matter* **6**, 2901 (2010).
- [47] D. Fenistein, J. W. van de Meent, and M. van Hecke, *Physical Review Letters* **92**, 94301 (2004).
- [48] S. Luding, *Granular Matter* **10**, 235 (2008).
- [49] T. Unger, J. Török, J. Kertész, and D. E. Wolf, *Physical Review Letters* **92**, 214301 (2004).
- [50] A. Singh, V. Magnanimo, K. Saitoh, and S. Luding, *Physical Review E* **90**, 022202 (2014).
- [51] B. Crüger, V. Salikov, S. Heinrich, S. Antonyuk, V. Sutkar, N. Deen, and J. Kuipers, *Particuology* **25**, 1 (2016).
- [52] O. I. Imole, D. Krijgsman, T. Weinhart, V. Magnanimo, E. C. Montes, M. Ramaioli, and S. Luding, *Powder Technology* **287**, 108 (2016).
- [53] S. von Kann, J. H. Snoeijer, D. Lohse, and D. van der Meer, *Physical Review E* **84**, 060401 (2011).



3

EFFECT OF COHESION ON LOCAL COMPACTION

This chapter results from an ongoing investigation of the effect of cohesion on the compaction of sheared soft wet granular materials. We compare dry non-cohesive and wet moderately-to-strongly cohesive soft almost frictionless granular materials and report the effect of cohesion between the grains on the local volume fraction. We study this in a three dimensional, unconfined, slowly sheared split-bottom ring shear cell, where materials while sheared are subject to compression under the confining weight of the material above. Our results show that inter-particle cohesion has a considerable impact on the compaction of soft materials. Cohesion causes additional stresses, due to capillary forces between particles, leading to an increase in volume fraction due to higher compaction. This effect is not visible in a system of infinitely stiff particles. In addition, acting oppositely, we observe a general decrease in volume fraction due to increased cohesion for frictional particle, which we attribute to the role of contact friction that enhances dilation.

3.1. INTRODUCTION

Unsaturated granular media of particles with interstitial liquid in the form of bridges between particle pair, display bulk cohesion, which can be tuned using different liquids with varying surface tension. Earlier studies have been on density correlation in terms of fractal structure of aggregates for dry cohesive powders [1]. Cohesive grains being sensitive to stress intensity as well as direction exhibit much larger variations in their equilibrium densities. Moreover, adhesion would enhance the role of sliding and rolling friction, because the limiting values for tangential contact forces and rolling moments are both proportional to the elastic repulsive part of the normal force. Fournier et al. [2] observed that wet granulates are significantly less densely packed than dry granular materials, but the packing densities in only weakly dependent on the amount of wetting liquid, an obvious reason being that the forces exerted by the liquid bridges are very

This chapter has been published in EPJ Web of Conferences **140**, (2017) [14].

weakly dependent on bridge volume [3]. At small liquid content and after sufficient equilibration, the interior of the wet granulate is expected to be characterized by a network of liquid bridges connecting adjacent grains. It is clear that the connectivity of this network of liquid bridges is of importance for the mechanics of the wet granular materials, be it directly due to the capillary forces itself or due to the enhancement of the mutual friction between the grains by the increased internal pressure. For the wet granular materials, this pressure increase is of the order $\Delta p \approx \sigma/r$ given by the Laplace-Young equation, where r is a typical radius of the grains and σ is the surface tension of liquid. The local volume fraction of the bulk on macro-scale is connected to the pressure gradient and is thus proportional to σ .

We study here the packing fraction in the critical state for non-cohesive to strongly cohesive systems by varying the surface tension of the liquid. Details of the simulation set-up is given in Sec. 3.2.1. Wet granular materials are cohesive and particles can stick together and form local agglomerates, due to formation of clusters of particles for very cohesive systems, as shown in Figure 3.1 and 3.4(c). Figure 3.1 shows the top view of the split bottom shear cell geometry with colors blue to red indicating z coordinate values of the particles. It is observed from the figure that some particles form clumps near the surface while the particles near the base are seen through the hollow region. Hence, the system is highly inhomogeneous in its spatial distribution.

3.2. MODEL SYSTEM

3.2.1. GEOMETRY

Split-Bottom Ring Shear Cell: We use MercuryDPM [4, 5], an open-source implementation of the Discrete Particle Method, to simulate a shear cell with annular geometry and a split bottom plate, as explained in [6]. Earlier studies used similar rotating set-ups, including [7, 8]. The geometry of the system consists of an outer cylinder (radius $R_o = 110$ mm) rotating around a fixed inner cylinder (radius $R_i = 14.7$ mm) with a rotation frequency of $\Omega = 0.01$ rotations per second. The granular material is confined by gravity between the two concentric cylinders and the bottom plate, with a free top surface. The bottom plate is split at radius $R_s = 85$ mm. Due to the split at the bottom, a narrow shear band is formed. It moves inwards and widens towards the flow surface. This set-up thus features a wide shear band away from the bottom and the wall which is free from boundary effects. The shear cell is filled up to a height of $H \approx 40$ mm under dry conditions, with particles of mean diameter $d_p = \langle d \rangle \approx 2.2$ mm, polydispersity $d_{\max}/d_{\min} = 2.0$ and homogeneous size distribution with width of $1 - \langle d \rangle / \langle d^2 \rangle = 0.04$, where a is the particle radius. Thus, the shear band remains far away from the inner wall. The inter-particle friction coefficient is $\mu_p = 0.01$ and other parameters are detailed in [6].

In earlier studies [9], a quarter of this system ($0^\circ \leq \phi \leq 90^\circ$) was simulated using periodic boundary conditions. In order to save computation time, here we simulate only a smaller section of the system ($0^\circ \leq \phi \leq 30^\circ$) with appropriate periodic boundary conditions in the angular coordinate, unless specified otherwise. We have observed no noticeable effect on the macroscopic behavior in comparisons between simulations done with a smaller (30°) or larger (90°) opening angle. Note that for very strong attractive forces, the system becomes inhomogeneous and loses its radial symmetry: i.e. agglomeration

of particles occurs. Then, particles interact on a larger length scale and thus the above statement is not true anymore.

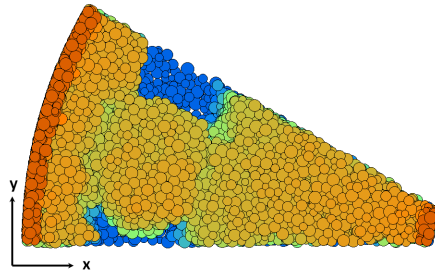


Figure 3.1: Top view of highly cohesive wet granular materials ($Bo_g = 34.6$). Different colors are the measure of low (blue), medium (green), high (yellow) and walls (red) z-coordinate of the particles.

3.2.2. CONTACT MODEL AND PARAMETERS

We use a linear visco-elastic frictional contact model in combination with Willet's capillary bridge model [3, 6, 10]. In order to see the effect of varying cohesive strength on the macroscopic rheology of wet materials, we vary the intensity of the maximum capillary force $f_{\text{cap}}^{\text{max}} = \pi d \sigma \cos \theta$, by varying the surface tension of the liquid σ , while keeping the volume of liquid bridges constant, ($V_b = 75$ nl), corresponding to a liquid saturation of 8% of the voidage. We compare here the volume fractions of non-cohesive to moderate to strongly cohesive granular materials, with surface tension of liquid ranging from $\sigma = 0 \text{ Nm}^{-1}$, up to $\sigma = 5 \text{ Nm}^{-1}$ for strongly cohesive systems. The contact angle is fixed at $\theta = 20^\circ$.

3.3. DIMENSIONLESS NUMBERS

The effects of varying shear rate, pressure, stiffness and cohesion can be modelled using three dimensionless numbers, expressed as a ratio of time-scales as given in Tab. 3.1, where the subscripts $\dot{\gamma}$, p , k and c denote strain-rate, pressure, stiffness and cohesion respectively [10]. In addition, we define the *global* Bond number as $Bo_g = f_{\text{cap}}^{\text{max}} / (p_{\text{mean}} d_p^2)$, where p_{mean} is the mean pressure in the system (at about half filling height $H/2$).

Table 3.1: Dimensionless numbers for the model

Dimensionless number	Definition	Time scale ratios
Inertial number I	$\frac{\dot{\gamma} d_p}{\sqrt{p/\rho}}$	$t_p / t_{\dot{\gamma}}$
Softness p^*	$\frac{p d_p}{k}$	$(t_k / t_p)^2$
Local Bond number Bo	$\frac{f_{\text{cap}}^{\text{max}}}{p d_p^2}$	$(t_p / t_c)^2$

3.4. RHEOLOGICAL MODEL

The macroscopic quantities are obtained by spatial coarse graining with temporal averaging of the system in steady state as detailed in [6, 10]. We study the effect of the above mentioned dimensionless numbers on the local volume fraction ϕ in the critical state [10]. The local volume fraction is expected to be dependent on various factors like the dilation, compression and the inter-particle friction. In the following sections, we discuss more of the effect of each dimensionless number on the local volume fraction.

3

3.4.1. NON-COHESIVE GRANULAR MATERIALS

For dry granular materials, $Bo = 0$, the rheology only depends on p^* and I . The dependence of the macroscopic friction coefficient $\mu = \tau/p$ on p^* and I has been studied in [9, 10]. In order to complete the rheology for soft, compressible particles, a relation for the solid volume fraction (packing fraction) as function of pressure and shear rate is missing for dry non-cohesive materials. In [11], the following dependency was observed:

$$\phi(I, p^*) = \phi_o f_I(I) f_p(p^*) \quad (3.1)$$

with the critical or steady state density under shear, first order i.e., in the limit of vanishing pressure and inertial number, $\phi_o = 0.64$, $f_p(p^*) = (1 + p^*/p_o^*)$, $f_I(I) = (1 - I/I_o)$. The typical strain rate for which dilation would turn to fluidization is $I_o = 0.85$, and the typical pressure level for which softness leads to huge densities is $p_o^* = 0.33$ [11]. Note that both correction functions are first order, i.e. they are valid only for sufficiently small arguments. Because of slow quasistatic flows in our simulations, no strong dilation is observed, i.e., no strong dependence of ϕ on the local shear rate. On the other hand, too large inertial numbers would fully fluidize the system so that the rheology should be that of a granular fluid, for which kinetic theory applies, while too large pressure would lead to enormous overlaps, for which the contact model and the particle simulation with pair forces become questionable.

3.4.2. COHESIVE GRANULAR MATERIALS

In cohesive flows, attractive forces enhance the local stresses acting on the particles and adds an attractive force which acts as an effective confinement and increased compression, i.e. increased volume fraction (at least for our nearly-frictionless spheres). Rough and frictional particles should display stronger dilatancy, a reduced volume fraction under shear. Having low inter-particle friction, we observe an overall increase in local volume fraction with Bo (plot not shown here). This overall effect is distinguished as contribution from compression of soft particles and due to structural changes in presence of friction as discussed in the following subsections.

EFFECT OF COHESION ON SOFT PARTICLES

In cohesive flows, cohesion enhances the compressive pressure acting on the particles. This can be quantified as follows: we split the net pressure into two components, $p = p_{\text{rep}} - p_{\text{cap}}$, denoting the respective contributions of repulsive and cohesive contact forces. The ratio between the total cohesive contribution and the total pressure is given by the local bond number, $Bo = p_{\text{cap}}/p$, and thus $p_{\text{rep}} = (1 + Bo)p$. As the geometrical compression (deformation at each contact) is related to the *repulsive* stress, it is the compressive

pressure p_{rep} that has to be considered in the softness factor f_p . Thus, the modified local softness correction for cohesive systems is given as:

$$f_p(p_{\text{rep}}^*) = f_p((1 + Bo)p^*) \quad (3.2)$$

For dry non-cohesive system when $Bo = 0$, one has $f_p((1 + Bo)p^*) = f_p(p^*)$. This is similar in spirit with the modified inertial number as presented in [12], which takes into account the cohesive contribution in confining stress. A similar modification in the inertial number is also required in the inertial regime weakly effective in the quasistatic regime.

GENERALIZED EFFECT OF COHESION

In addition to the effect of cohesion on the softness of particles, cohesion also changes the microstructure [1, 2] in presence of rolling and sliding friction. To study this additional effect, we analyse the local packing fraction ϕ scaled by f_I and f_p as a function of the local Bond number Bo as shown in Figure 3.2. All the data shown in Figure 3.2 correspond to the critical state, though a shear band is not clearly defined in strongly cohesive systems ($Bo_g > 3.46$). It is observed from Figure 3.2 that all data for different Bo_g collapse, following a trend and the dependence is given by the solid line in Figure 3.2 as:

$$f_c(Bo) = \left[1 - \left(\frac{Bo}{Bo_c} \right)^\alpha \right] \quad (3.3)$$

where, $\phi_o = 0.65$, $\alpha = 0.57$ and $Bo_c = 729$ denotes the limiting Bond number above which the correction is not applicable anymore. The dash-dotted line represents a linear fit $f_c^{\text{lin}}(Bo)$ that ignores the larger Bo data, with $\alpha = 1$. Note that due to different friction $\mu_p = 0.5$, $\phi_o = 0.60$, $\alpha = 0.71$ and $Bo_c = 42.63$ for the dashed fit in Figure 3.2 corresponding to the data from [13] for frictional monodisperse particles.

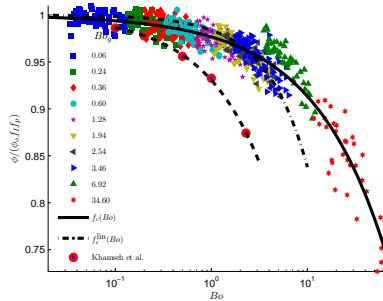


Figure 3.2: Scaled local packing fraction $\phi/(\phi_o f_I f_p)$ as a function of the local Bond number Bo showing the general decrease in scaled local volume fraction with cohesion. The solid line is given by Eq. 3.3 with parameters given in Tab. 3.2. The dash-dotted line corresponds to a simple linear fit $f_c^{\text{lin}}(Bo) = 1 - Bo/62$ corresponding to the data with $Bo < 3$. The dashed line corresponds to the fit for the data from [13].

To confirm the effect of cohesion on the compressibility of soft particles, we re-plot Figure 3.2 in another possible way, i.e., $\phi/(\phi_o f_I f_c)$ as a function of $(1 + Bo)p^*$ as shown in Figure 3.3. In a way, this is the effect of compression of soft particles with increasing

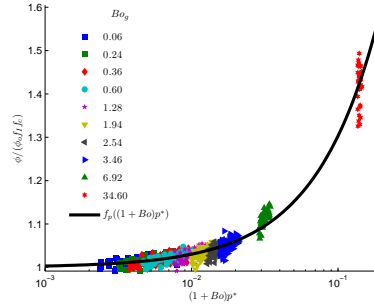


Figure 3.3: Scaled local packing fraction $\phi/(\phi_o f_I f_c)$ as a function of $(1 + Bo)p^*$ showing the effect of compaction of soft particles with increasing cohesion. The solid line is given by Eq. 3.2.

cohesion which is given by the function $f_p((1 + Bo)p^*)$ as shown by the solid line in the figure.

Table 3.2: Coefficients for the model

Dimensionless number	Corrections	Coefficients
Critical volume fraction (ϕ_o)		$\phi_o = 0.65$
Inertial number (I)	$f_I = \left(1 - \frac{I}{I_o}\right)$	$I_o = 0.85$
Softness (p_{rep}^*)	$f_p = \left[1 + \frac{p_{\text{rep}}^*}{p_o^*}\right]$	$p_o^* = 0.33$
Cohesion (Bo)	$f_c = \left[1 - \left(\frac{Bo}{Bo_c}\right)^\alpha\right]$	See Sec. 3.4.2.

Thus the complete rheology for the local volume fraction is given as:

$$\phi(I, p^*, Bo) = \phi_o f_I(I) f_p((1 + Bo)p^*) f_c(Bo) \quad (3.4)$$

In the case of rigid particles, $p^* \rightarrow 0$ so that Eq. 3.4 reduces to $\phi_{\text{stiff}} = \phi(I, 0, Bo) = \phi_o f_I f_c$.

DISCUSSION

Cohesion can either contribute to a decrease or an increase in the local volume fraction of sheared materials, depending on the inter-particle friction and the softness of materials. Note that compression is prevailing for soft particles but is negligible when $p^* > 0$ in the limit of infinite stiffness, when the local volume fraction is expected to increase with Bo . Berger et al. [12] uses contact dynamics for simulation which assumes that particles are infinitely stiff. Khamseh et al. [13] also shows that the volume fraction decreases for higher cohesion where the simulations are done using DEM with very stiff glass beads of Young modulus $E = 70$ GPa, so that for both, the softness effect is negligible.

Figure 3.4 (a), (b) and (c) show the contour plot of the spatial distribution of local packing fraction with the magnitude given by the color map for different $Bo_g = 0, 1.94$ and 34.6 , respectively. Focusing on the shear band center, the mean volume fraction is close to 0.65 for non-cohesive materials as shown in Figure 3.4(a). In comparison, the

mean volume fraction of the strongly cohesive materials is 0.75 in Figure 3.4(c). The vertical center of mass of the materials decreases by 25% from non-cohesive (a) to strongly cohesive (c) materials.

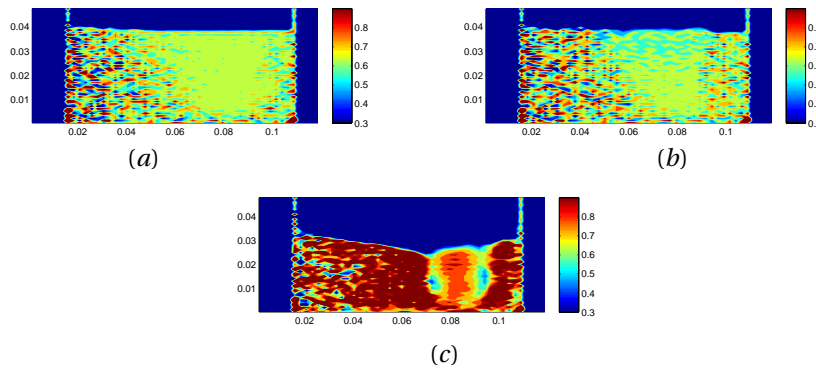


Figure 3.4: Contour plot of volume fraction for (a) $Bo_g = 0.0$, (b) $Bo_g = 1.94$ and (c) $Bo_g = 34.6$ in the $r-z$ plane. Color-bar represents the local volume fraction ϕ . Both (a) and (b) are homogeneous in angular direction, while (c) displays cohesion-induced compression and inhomogeneity (granulation) of materials.

3.5. CONCLUSION

We studied the local packing fraction of dry and wet granular materials as a function of dimensionless numbers, namely, the inertial number I , the softness p^* and the Bond number Bo . Focus is on the effect of cohesion (quantified by the Bond number). Earlier studies have shown that the packing fraction of dry granular materials is to the first order linearly dependent on I and p^* .

We observe that the cohesive stress contributes to the softness for wet granular materials. This leads to an additional linear increment of local volume fraction with Bo . This effect is prevailing for soft particles and becomes negligible in the limits of stiff particles. Additionally, the local volume fraction decreases as a power law dependence on the local Bond number Bo . This is a more general effect of Bo on the local volume fraction related to the structural changes and increasing friction force of the materials.

Our results show that for strongly cohesive systems, our almost frictionless materials are overall densely compacted and center of mass of the bed drops by approximately 25%. The coordination number increases with local volume fraction. However, the trends are not clear enough and to have a complete understanding of the rheology, the dependence of the coordination number and the granular temperature on p^* , I and Bo should be studied.

REFERENCES

- [1] E.A. Gilabert, J.N. Roux, A. Castellanos, *Physical Review E* **75**, 11303 (2007).
- [2] Z. Fournier, D. Geromichalos, S. Herminghaus, M.M. Kohonen, F. Mugele,

- M. Scheel, M. Schulz, B. Schulz, C. Schier, R. Seemann et al., *Journal of Physics: Condensed Matter* **17**, S477 (2005).
- [3] C.D. Willett, M.J. Adams, S.A. Johnson, J. Seville, *Langmuir* **16**, 9396 (2000).
- [4] A. Thornton, T. Weinhart, S. Luding, O. Bokhove, *International Journal Modern Physics C* **23**, 1240014 (2012).
- [5] T. Weinhart, A. Thornton, S. Luding, O. Bokhove, *Granular Matter* **14**, 289 (2012).
- [6] S. Roy, A. Singh, S. Luding, T. Weinhart, *Computational Particle Mechanics* **3**, 449–462 (2016).
- [7] X. Wang, H.P. Zhu, A.B. Yu, *Granular Matter* **14**, 411 (2012).
- [8] E. Woldhuis, B.P. Tighe, W. Saarloos, *The European Physical Journal E: Soft Matter and Biological Physics* **28**, 73 (2009).
- [9] A. Singh, V. Magnanimo, K. Saitoh, S. Luding, *New Journal of Physics* **17**, 043028 (2015).
- [10] S. Roy, S. Luding, T. Weinhart, *New Journal of Physics* **19**, 043014 (2017).
- [11] S. Luding, A. Singh, S. Roy, D. Vescovi, T. Weinhart, V. Magnanimo, *The 7th International Conference on Discrete Element Methods* (2016).
- [12] N. Berger, E. Azéma, J.F. Douce, F. Radjai, *Europhysics Letters* **112**, 64004 (2016).
- [13] S. Khamseh, J.N. Roux, F. Chevoir, *Physical Review E* **92**, 022201 (2015).
- [14] S. Roy, S. Luding, T. Weinhart, *EPJ Web of Conferences* **140**, 03065 (2017).

4

MICRO-MACRO TRANSITION AND SIMPLIFIED CONTACT MODELS FOR WET GRANULAR MATERIALS

Wet granular materials in a quasi-static steady state shear flow have been studied with discrete particle simulations. Macroscopic quantities, consistent with the conservation laws of continuum theory, are obtained by time averaging and spatial averaging of ensembles of particles. Initial studies involve understanding the effect of liquid content and liquid properties like the surface tension on the macroscopic quantities. Two parameters of the liquid bridge contact model have been studied as the constitutive parameters that define the structure of this model (i) the rupture distance of the liquid bridge model, which is proportional to the liquid content, and (ii) the maximum adhesive force, as controlled by the surface tension of the liquid. Subsequently a correlation is developed between these micro parameters and the steady state cohesion in the limit of zero confining pressure. Furthermore, as second result, the macroscopic torque measured at the walls, which is an experimentally accessible parameter, is predicted from our simulation results as a dependence on the micro-parameters. Finally, the steady state cohesion of a realistic non-linear liquid bridge contact model scales well with the steady state cohesion for a simpler linearized irreversible contact model with the same maximum adhesive force and equal energy dissipated per contact.

4.1. INTRODUCTION

Granular media are collections of microscopic grains having athermal interactions through dissipative, frictional or cohesive contact forces. External force leads to granular flow under the condition of applied shear stress exceeding the yield shear stress. After a finite shear strain, at constant rate, a steady state establishes with a typically lower shear

This chapter has been published in Computational Particle Mechanics 3, 4 (2016) [2].

stress, depending on both strain rate and pressure [1]. Most studies in granular physics focus on dry granular materials and their flow rheology. However, wet granular materials are ubiquitous in geology and many real world applications where interstitial liquid is present between the grains. Simplified models for capillary clusters [3, 4] and wet granular gases [5] were introduced before. The rheology of flow for dense suspension of non-Brownian particles have been studied in Ref. [6–8]. Granular shear band formation has been extensively probed in [9, 10] where narrow shear bands are exhibited near the boundaries. We study the local rheology of weakly wetted granular materials in the quasistatic regime with the Discrete Element Method (DEM) using the open-source package MercuryDPM [11, 12] in a split-bottom shear cell set-up. In contrast to the Couette cell, here the relative motion is confined to particles in a wide shear band away from the walls [13, 14]. We study partially saturated systems in the pendular regime, with a very low level of water content, where the formation of liquid bridges between particle pairs leads to development of microscopic tensile forces. This tensile forces generated at particle level results in cohesion at macroscopic scale. Many studies have been done for liquid bridge in the pendular regime to understand the effect of liquid bridge volume and contact angle on different macroscopic quantities like the steady state cohesion, torque and shear band properties [15–19] and wet granulation [55, 56]. Other studies for unsaturated granular media observe fluid depletion in shear bands [20, 21]. However, there is no theoretical framework or concrete model available yet that defines the exact correlation between the micro parameters like the liquid bridge volume and the surface tension of the liquid with the steady state cohesion.

4

In order to develop a micro-macro correlation for the liquid bridge contact model, we initially study the structure of the micro contact model. How is the structure of the liquid bridge contact model affected by the microscopic parameters? How does this influence the steady state cohesion? Here we study in detail on the effect of these parameters on the macro results. For example, the effect of maximum interaction distance, or the distance at which the liquid bridge between two interacting particles ruptures, is studied by varying the liquid content. On the other hand other parameters like surface tension of the liquid and contact angle affect the magnitude of force acting between the particles when in contact [17, 22]. Various surface tension of liquids give a large scale variation of the capillary force and this allows us to study the effect of maximum force on the macroscopic properties. Furthermore, in the consecutive analysis, we make an attempt to re-obtain the macro-rheology results in the shear band center from the torque, torque being an experimentally measurable quantity.

The liquid bridge interactions between the particles are defined by the free-surface equilibrium shapes and stability of the bridge configuration between them [23–25]. Phenomenologically, even the simplified models of liquid bridges are quite complex in nature. We have several reasons to look for a simpler linear adhesive contact model that can replace a complex liquid bridge contact model. Can one get away from the complexities by choosing an oversimplified contact model which can be solved analytically? What are the relevant key parameters and features of different contact models that results in the same bulk properties of the material? Improving the computational efficiency for wet granular materials by replacing the non-linear interactions of liquid bridges with a simpler linear one is also a possible reason, though not a major one. But in what way can

a non-linear model like the liquid bridge contact model be replaced by a linear model? When can we say that the two different contact models are analogous? Therefore, we compare the realistic liquid bridge model with an equivalent simple linear adhesive contact model [42] that would give the same macroscopic effect.

The results in this paper are organized in three main parts. In Sec. 4.3.1 of this paper we study the effect of varying liquid bridge volume and surface tension of the liquid on the macroscopic properties, the focus being to find a micro-macro correlation from this study. Most strikingly, we see a well defined relationship between these micro parameters and the macro properties like the steady state cohesion of the bulk material and macro-torque required under shear, neglecting the effect of fluid depletion in shear bands [20, 21] in quasistatic flow. In Sec. 4.3.2 of this paper we show the derivation of macro torque from the boundary shear stress. In this section we also compare this torque with the torque calculated from forces due to contacts on the wall particles. In Sec. 4.4 of this paper, we discuss about the analogy of two different contact models, with a goal to understand which parameters at microscopic scale would give the same macroscopic behavior of the system.

4.2. MODEL SYSTEM

4.2.1. GEOMETRY

Split- Bottom Ring Shear Cell: The set-up used for simulations consists of a shear cell with annular geometry and a split in the bottom plate, as shown in Figure 4.1. Some of the earlier studies in similar rotating set-up include [26–28]. The geometry of the system consists of an outer cylinder (radius $R_o = 110$ mm) rotating around a fixed inner cylinder (radius $R_i = 14.7$ mm) with a rotation frequency of $\Omega = 0.01$ s⁻¹. The granular material is confined by gravity between the two concentric cylinders, the bottom plate, and a free top surface. The bottom plate is split at radius $R_s = 85$ mm into a moving outer part and a static inner part. Due to the split at the bottom, a shear band is formed at the bottom. It moves inwards and widens as it goes up, due to the geometry. This set-up thus features a wide shear band away from the wall, free from boundary effects, since an intermediate filling height ($H = 36$ mm) is chosen, so that the shear band does not reach the inner wall at the free surface.

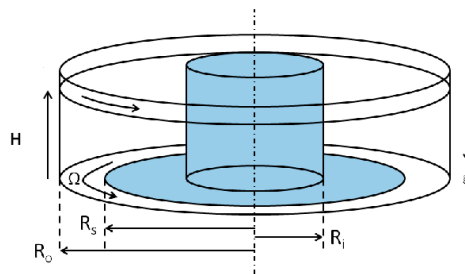


Figure 4.1: Shear cell set-up.

Table 4.1: Model parameters

Parameter	Symbol	Value
Number of particles	N	11119
Sliding friction coefficient	μ_p	0.01
Elastic stiffness	k	120 Nm^{-1}
Viscous damping coefficient	γ_o	$0.5 \times 10^{-3} \text{ kgs}^{-1}$
Angular frequency	Ω	0.01 s^{-1}
Particle density	ρ	2000 kgm^{-3}
Mean particle diameter	d_p	2.2 mm
Contact angle	θ	20°

In earlier studies [1, 29, 30], similar simulations were done using a quarter of the system ($0^\circ \leq \phi \leq 90^\circ$) using periodic boundary conditions. In order to save computation time, here we simulate only a smaller section of the system ($0^\circ \leq \phi \leq 30^\circ$) with appropriate periodic boundary conditions in the angular coordinate, unless specified otherwise. We have observed no noticeable effect on the macroscopic behavior in comparisons between simulations done with a smaller (30°) and a larger (90°) opening angle. Note that for very strong attractive forces, the above statement is not true anymore.

4.2.2. MICROSCOPIC MODEL PARAMETERS

In presence of a small amount of liquid in a dense granular material, bridges are formed at the contact points between the particles. The surface energy of these bridges leads to an attractive force between the particles, which is absent in dry granular materials. Thus, wetting changes a granular system from one with only repulsive inter-particle interactions to one with both repulsive and attractive interactions [31]. With the change in microscopic physical interactions in wet granular materials, the macroscopic behavior is also expected to differ from the dry materials. Therefore, we choose to vary some of the characteristic specifications of a liquid bridge model to understand the effect on macroscopic properties. All the particle specifications and the fixed interaction parameters for the contact models are given in Table 4.1. All the variable interaction parameters which include the liquid bridge volume V_b and the surface tension of the liquid σ are discussed in this section.

BULK SATURATION AND LIQUID BRIDGE VOLUME

The bulk material can be characterized by different states such as the dry bulk, adsorption layers, pendular state, funicular state, capillary state or suspension depending on the level of saturation [32, 33]. In this paper we intend to study the phenomenology of liquid bridge between particles in the pendular state, where the well separated liquid bridges exist between particle pairs without geometrical overlap. In this section, we discuss about the critical bulk saturation of granular materials and the corresponding liquid bridge volumes in the pendular state.

The bulk saturation S^* is defined as the ratio of liquid volume to void volume of the bulk [34, 35]. The demarcation between the pendular state and the more saturated fu-

nicular state is given by the saturation $S^* \approx 0.3$ [34]. For each particle pair with a liquid bridge, a dimensionless volume φ^* can be defined as the ratio of the volume of the liquid bridge at the contact, V_b to the volume of the two contacting particles, $2V_p$:

$$\varphi^* = \frac{V_b}{2V_p} = \frac{V_b}{2(\frac{\pi}{6}d_p^3)} \quad (4.1)$$

Assuming the liquid is homogeneously distributed throughout the material, the bulk saturation S^* is obtained from the dimensionless volume φ^* and the bulk porosity ϵ from the following equation [34, 35]:

$$S^* = \pi \frac{1-\epsilon}{\epsilon^2} \varphi^* \quad (4.2)$$

With a bulk porosity of the material $\epsilon = 0.4$ and a mean particle diameter d_p of 2.20 mm, the maximum liquid bridge volume in the pendular regime is approximately 284 nl. In order to study the influence of liquid content on the macroscopic properties, we analyzed the system for the following set of liquid bridge volumes V_b :

$$V_b \in [0, 1, 2, 4.2, 8, 14, 20, 75, 140, 200] \text{ nl} \quad (4.3)$$

which are seen to be well within the pendular regime. The corresponding saturation:

$$S^* \in [0, 0.001, 0.002, 0.004, 0.008, 0.015, 0.021, 0.079, 0.148, 0.211] \quad (4.4)$$

In order to investigate the functional form of steady state cohesion beyond this state, a few more simulations for higher V_b are done:

$$V_b \in [500, 1000] \text{ nl} \quad (4.5)$$

for which the pendular assumption is not valid anymore.

SURFACE TENSION OF LIQUID

Surface tension results from the greater attraction of liquid molecules towards each other than towards air. It is the tendency of liquids to lower their state of energy which makes it acquire the least possible surface area at the surface with higher inter liquid molecules attraction. As a result, cohesive properties of liquids are reflected in surface tension which makes it an interesting parameter to study. This effect will be discussed in detail in Sec. 4.2.3. The effect of surface tension on the macroscopic properties is studied for the following range of surface tension values:

$$\sigma \in [0, 0.02, 0.04, 0.06] \text{ Nm}^{-1} \quad (4.6)$$

Surface tension of most of available liquid-air interfaces at 20°C are in this range. To explore the functional behavior of steady state cohesion beyond this state, a few more simulations for intermediate and higher σ are done:

$$\sigma \in [0.01, 0.10, 0.50, 1.00] \text{ Nm}^{-1} \quad (4.7)$$

4.2.3. LIQUID BRIDGE CONTACT MODEL

The contact and non-contact forces for interacting particles can be described by a combination of an elastic contact model for the normal repulsive force and a non-linear irreversible adhesive non-contact model for the adhesive force. Figure 4.2 represents a sketch of the combined liquid bridge contact model as a function of the overlap between the two particles. The liquid bridge adhesive force acts between the particles once the

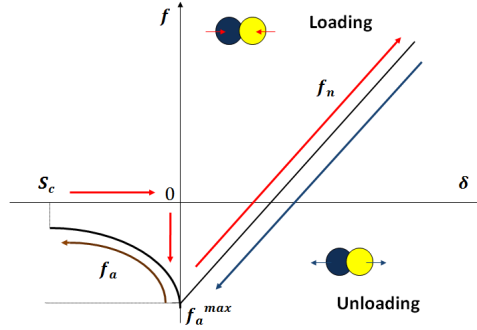


Figure 4.2: Liquid capillary bridge model. The red lines represent the loading direction, the blue line represents the unloading direction when the particles are in contact and the brown line represents the unloading for the non-contact particles with short-range interaction force.

contact is established. When the particles are in contact, the attractive force is given by Eq. 4.12. This is independent of the liquid bridge volume and depends on the surface tension of the liquid, radius of particles and contact angle. There is no cohesive force between the particles during approach. As the liquid bridge only forms once the particles come in contact with each other, the cohesive force starts acting and remains constant during overlap between particles $\delta > 0$. Normal contact repulsive force acts between the particles in contact in addition, given by:

$$f_n = k\delta + \sigma_o\dot{\delta}, \quad (4.8)$$

where k is the elastic stiffness, σ_o is the viscous damping coefficient and δ is the overlap between the particles. The normal contact forces for the liquid bridge model are explained in Sec. 4.2.3

LIQUID BRIDGE CAPILLARY FORCE MODEL

The capillary pressure difference sustained across the liquid-air interface due to surface tension can be described by the non-linear Laplace-Young equation [25]. This relates the pressure difference to the shape of the surface under the criterion of minimum Gibbs free energy [36]. The capillary force in a pendular bridge originates from the axial component of this force. Another component that contributes to the capillary force is due to the hydrostatic pressure. Many previous studies have calculated capillary forces based on the numerical solution of the Laplace-Young equation and also reported experimental results [22, 25]. The magnitude of liquid bridge capillary force depends on the volume of the liquid bridge between the particles, the contact angle θ , surface tension σ ,

the effective radius of the particles r and the separation distance S , $S = -\delta$. With these parameters we approximate the inter-particle force f_c of the capillary bridge according to [22]. The experimental results are fitted by a polynomial to obtain the dependence of capillary forces on the scaled separation distance. During approach of the particles, the normal contact force for this model is given by:

$$f = \begin{cases} 0 & \text{if } \delta < 0; \\ -f_a^{\max} + f_n & \text{if } \delta \geq 0. \end{cases} \quad (4.9)$$

During separation of the particles, the normal contact force for this model is given by:

$$f = \begin{cases} 0 & \text{if } \delta < -S_c; \\ -f_a & \text{if } -S_c \leq \delta < 0; \\ -f_a^{\max} + f_n & \text{if } \delta \geq 0, \end{cases} \quad (4.10)$$

where f_n is the normal repulsive force given by Eq. 4.8. The adhesive force for the liquid bridge model is the capillary force given by:

$$f_a = (f_a)_{\text{liq}} = \frac{(f_a^{\max})_{\text{liq}} \left(\frac{d}{d_p}\right)}{1 + 1.05\bar{S} + 2.5\bar{S}^2}, \quad (4.11)$$

where the separation distance is normalised as $\bar{S} = S\sqrt{(d/2V_b)}$, S being the separation distance. The maximum capillary force between the particles when they are in contact ($S = 0$) is given by:

$$(f_a^{\max})_{\text{liq}} = \pi d_p \sigma \cos \theta, \quad (4.12)$$

where, d_p is the mean particle diameter. The effective diameter of two interacting spherical particles of different size can be estimated as the harmonic mean of the two particle diameter according to the Derjaguin approximation [37], yielding the effective diameter of the two interacting particles of diameter d_i and d_j :

$$d = \frac{2d_i d_j}{d_i + d_j}, \quad (4.13)$$

however, the mean size is not varied here. This model equation is applicable for mono-disperse particles [15, 22] which has been actually extended to poly-disperse system of particles Ref. [17]. As proposed by [38], the critical separation distance S_c between the particles before the bridge ruptures is given by:

$$(S_c)_{\text{liq}} = \left(1 + \frac{\theta}{2}\right) V_b^{1/3} \quad (4.14)$$

The liquid bridge capillary force as a function of separation distance is shown in Figure 4.3 for different liquid bridge volumes. The liquid bridge capillary force decreases in magnitude with increasing separation distance between the particles till the bridge ruptures. The rupture distance is proportional to $V_b^{1/3}$ as stated in Eq. 5.3.

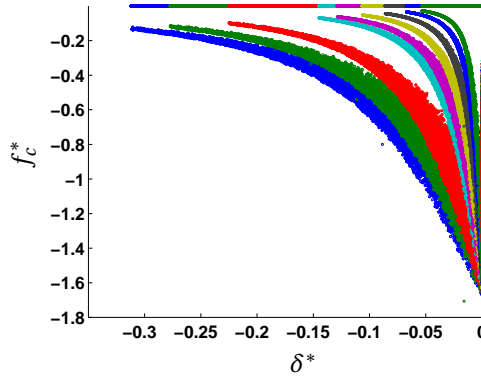


Figure 4.3: f_c^* as a function of δ^* . Different colors represent different liquid bridge volumes.

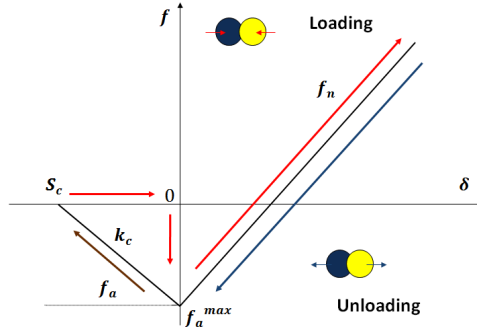


Figure 4.4: Linear irreversible contact model. The red lines represent the loading direction, the blue line represents the unloading direction when the particles are in contact and the brown line represents the unloading for the non-contact particles with short-range interaction force.

LINEAR IRREVERSIBLE CONTACT MODEL

In Sec. 4.4 we introduce a simple linear irreversible contact model as proposed by [42] and shown in Figure 4.4 which can be compared with the non-linear liquid bridge interaction model. For the linear irreversible contact model, the normal forces between particles during approach and separation are given by Eqs. 4.9 and 4.10 respectively, where for the linear irreversible contact model,

$$f_a = (f_a)_{\text{lin}} = (f_a^{\text{max}})_{\text{lin}} + k_c \delta, \quad (4.15)$$

$$(S_c)_{\text{lin}} = (f_a^{\text{max}})_{\text{lin}} / k_c, \quad (4.16)$$

where $(f_a^{\text{max}})_{\text{lin}}$ is the maximum adhesive force and k_c is the adhesive stiffness. The tangential force contact model is explained in details in our earlier studies [29].

Table 4.2: Non-dimensionalization of parameters

Parameter	Symbol	Scaled term	Scaling term
Capillary force	f_c	f_c^*	f_g
Particle overlap	δ	δ^*	d_p
Shear stress	τ	τ^*	f_g/d_p^2
Pressure	P	P^*	f_g/d_p^2
Steady state cohesion	c	c^*	f_g/d_p^2
Liquid bridge volume	V_b	V_b^*	d_p^3
Surface tension	σ	σ^*	f_g/d_p
Rupture distance	S_c	S_c^*	d_p
Torque	T_z	T_z^*	$f_g d_p$
Angular rotation	θ_{rot}	θ_{rot}^*	2π
Adhesive Energy	E	E^*	$f_g d_p$

4.2.4. DIMENSIONAL ANALYSIS

To formulate all the modeling equations in a constructive way, we express them in nondimensionalized form. All the length scale parameters are scaled by the mean particle diameter $d_p = 2.20$ mm. The forces are scaled in terms of the gravitational force acting on a single particle $f_g = V_p \rho g \approx 1.0939 \times 10^{-4}$ N. Note that the other relevant scaling parameter is the surface tension force $f_\sigma = \pi d_p \sigma \cos \theta$ on a single particle trapped in the rim of the droplet. Table 4.2 shows all the parameters in their dimensionless form and the corresponding scaling terms used in the equations. The angular rotation of the shear cell after a given time to study the dynamic evolution of torque is scaled in terms of radians covered in one complete rotation (2π). The dynamics of the system can be characterized by the time scale defined by the contact duration between two particles $t_{\text{con}} = \sqrt{\frac{m_p}{k}}$, where m_p is the mean mass of a particle. Since we do all our macro-rheology analysis in steady state, characterization of dynamics of the system is not required. The main objectives of nondimensionalization is to simplify the equations in terms of unit less quantities and define the system intrinsically.

4.3. MICRO MACRO TRANSITION

To extract the macroscopic properties, we use the spatial averaging approach detailed in [39–41]. The averaging is performed over toroidal volume, over many snapshots of time assuming rotational invariance in the tangential ϕ -direction. The averaging procedure for a three dimensional system is explained in [40, 41]. This spatial coarse-graining method was used earlier in [1, 29, 30, 41, 42]. The simulation is run for 200 s and temporal averaging is done when the flow is in steady state, between 80 s to 200 s, thereby disregarding the transient behavior at the onset of the shear.

4.3.1. STEADY STATE COHESION AND ITS CORRELATION WITH LIQUID BRIDGE VOLUME AND SURFACE TENSION

From the history of research in soil mechanics, the steady state shear stress approaches a *zero* value in zero pressure limit, showing a non-linear dependence of the shear stress as a function of the normal stress. However, a finite cohesion value is often extrapolated linearly in the yield state as well as in the steady state zero pressure limit by applying Mohr Coulomb theory [47, 48]. The concept of yield state cohesion is rather significant and is discussed in [43–46]. A detailed description of granular microstructure provides the key for understanding the quasistatic rheology of granular materials [49–51]. In our present study, we consistently focus on the effect of micro parameters on this cohesion in the steady state by a linear interpolation in the zero pressure limit, applying Mohr Coulomb theory neglecting the low pressure data. In a geometrical set-up like the split-bottom shear cell, the critical or steady state is achieved inside the shear band center after long enough shear. In earlier studies [15, 29, 39, 40], the shear band region was identified by the criterion of large shear rate, *e.g.* higher than a critical shear rate of 0.08 s^{-1} . In this paper, the shear band center region is defined by shear rates higher 80% of the maximum for different heights in the shear cell. Figure 4.5 displays the dependence of scaled yield stress τ^* for the particles in the shear band region on scaled pressure P^* for 75 nl liquid bridge volume. A linear trend is observed neglecting the different behavior for data at very low pressure ($P^* < 4.42$). This is fitted well by a linear function:

$$\tau^* = \mu P^* + c^* \quad (4.17)$$

where μ is the macroscopic friction coefficient and c^* is the steady state cohesion obtained from the plot. Next, we fit the data for shear stress as a function of pressure as given by Eq. 4.17 and obtain the value of steady state cohesion and macroscopic friction μ . The macroscopic friction coefficient is constant for lower surface tension, including $\sigma^* = 0$ for linear elastic model (not shown in figure), but increases for $\sigma^* \gtrsim 2$ for a given liquid bridge volume as shown in Figure 4.6(a). When the surface tension of the material is very high ($\sigma^* \gtrsim 1.00$), materials protrude out of the top surface to form a hump in the region of the shear band (data not shown). For our analysis of surface tension in the range $0.020\text{--}0.040 \text{ Nm}^{-1}$, the macroscopic friction coefficient is constant at $\mu \approx 0.15$. In this range, the macroscopic friction coefficient is also independent of the liquid bridge volume as shown in Figure 4.6(b).

For dry cohesionless systems, the dependence of shear stress on pressure is linear without an offset, *i.e.* $c^* = 0$. In the presence of interstitial liquid between the particles in the pendular regime, cohesive forces increase with increasing liquid bridge volume. This results in a positive steady state cohesion c^* as given by Eq. 4.17, see Figure 4.5. Increase in microscopic surface tension of liquid results in an increasing shear stress and thus steady state cohesion increases.

Earlier studies on wet granular materials have shown that the presence of liquid bridges between the particles results in an increasing steady state cohesion of the materials [15, 16, 18, 29]. Our earlier studies show that the steady state cohesion c^* increases non-linearly with increasing liquid bridge volume. Here, the steady state cohesion is studied in more detail, including very small liquid bridge volumes, including the (practically impossible) limit of 0 nl liquid bridge volume as given in Eq. 4.3. Note that there

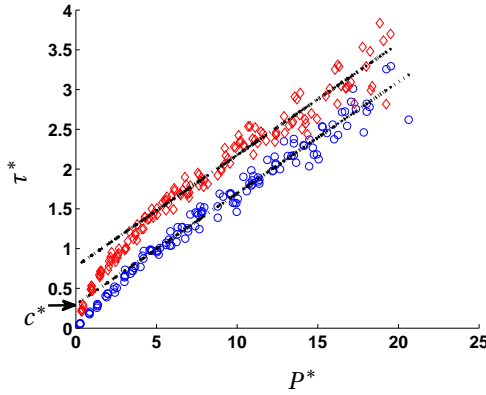


Figure 4.5: Steady state shear stress τ^* plotted against pressure P^* for surface tension of liquid $\sigma = 0.020 \text{ Nm}^{-1}$ (blue \circ) and $\sigma = 0.060 \text{ Nm}^{-1}$ (red \diamond). The dotted line represents the fitting function as given by Eq. 4.17 for $P^* > 4.42$ where $\mu = 0.15$ is the macroscopic friction coefficient, $c^* = 0.2655$ for $V_b = 75 \text{ nl}$ and $\sigma = 0.020 \text{ Nm}^{-1}$.

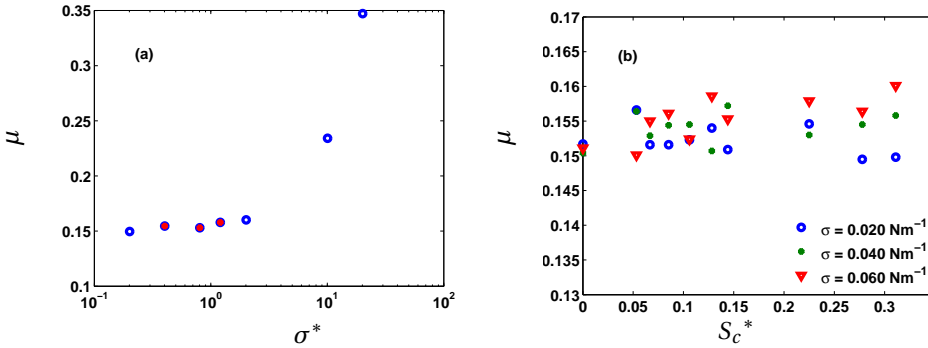


Figure 4.6: Macroscopic friction coefficient μ as a function of (a) scaled surface tension of liquid σ^* for $V_b = 75 \text{ nl}$ (b) scaled rupture distance S_c^* for different σ . The red dots in figure (a) correspond to the σ in legend of figure (b).

is a finite cohesive strength for $V_b \rightarrow 0 \text{ nl}$ liquid bridge volume. This is due to the microscopic capillary bridge force that acts between particles even at 0 nl liquid bridge volume as given by Eq. 4.12. This is called the steady state critical cohesion c_0^* for a given surface tension of liquid. This value depends on the maximum force acting between two particles when they are in contact as given by Eq. 4.12. The additional cohesion for higher liquid bridge volume is due to the non-contact capillary forces between the particles that are active upto the distance when the liquid bridge ruptures. This is dependent on the surface tension of the liquid and the volume of the liquid bridge. Thus, the steady state cohesion of granular materials for a given liquid bridge volume can be written as:

$$c^* = c_0^* + c'^* \tag{4.18}$$

where c'^* is the additional cohesion for liquid bridge volume $V_b > 0$. Figure 4.7(a) shows

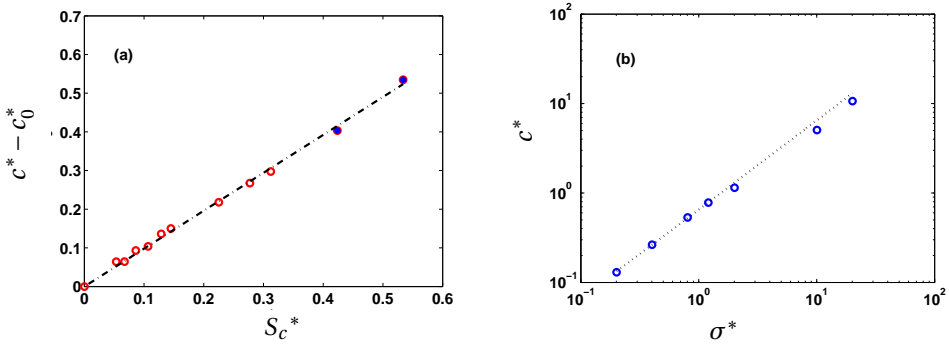


Figure 4.7: (a) Steady state incremental cohesion $c^* - c_0^*$ as a function of S_c^* for $\sigma = 0.020 \text{ Nm}^{-1}$. The dotted line represents the fitting function given by Eq. 4.19. The data with solid symbols represent the liquid bridge volume outside the pendular regime. (b) steady state cohesion c^* as a function of σ^* for $V_b = 75 \text{ nl}$. The dotted line represents the fitting function given by Eq. 4.20.

4

$(c^* - c_0^*)$ as a linear function of S_c^* , fitted by:

$$c^* - c_0^* = aS_c^* \quad (4.19)$$

where $a = 0.98$ for $\sigma = 0.020 \text{ Nm}^{-1}$. Next we study the dependence of this constant on the surface tension of liquid.

Figure 4.7(b) shows the dependence of steady state cohesion on σ^* for $V_b = 75 \text{ nl}$. The steady state cohesion can be described by:

$$\ln c^* = \alpha \ln \sigma^* + k \quad (4.20)$$

where $\alpha \approx 1.00$, $k = -0.4240$. Therefore, the steady state cohesion is linearly proportional to the surface tension and can be written as:

$$c^* = b\sigma^* \quad (4.21)$$

where $b = \exp(k)$. The above equation is valid in the limit of zero surface tension ($\sigma^* = 0$) which represents the simple linear elastic contact model. For higher surface tension of liquid, the results deviate from the fitted function of linear dependence as seen from Figure 4.7(b). As given by Eq. 4.19 and 4.20, the steady state cohesion is dependent on liquid bridge volume expressed in terms of maximum interaction distance S_c^* between the particles and the maximum adhesive force expressed in terms of surface tension of the liquid σ^* . So in the later sections of this paper we study the dependence of macroscopic parameters on the micro parameters S_c^* representing scaled rupture distance and σ^* representing scaled maximum force for all contact models.

Figure 4.8 shows the dependence of $\frac{c^* - c_0^*}{\sigma^*}$ on S_c^* for different surface tension. The scaled steady state cohesion is linearly dependent on the rupture distance. This can be fitted by a straight line equation given by:

$$\frac{c^* - c_0^*}{\sigma^*} = \frac{c^* - c_0^*}{(f_a^{\max})_{\text{liq}}^* l(\pi \cos \theta)} = pS_c^* \quad (4.22)$$

where $p = 2.1977$ as obtained from the fitting shown in Figure 4.8; the offset is very small and can be neglected. Though the data actually do not show a good collapse, a plot of the function $c^*/\sigma^* = pS_c^* + c_0^*/\sigma^*$ show a good collapse, signifying that c_0^* has significant error in the fitting.

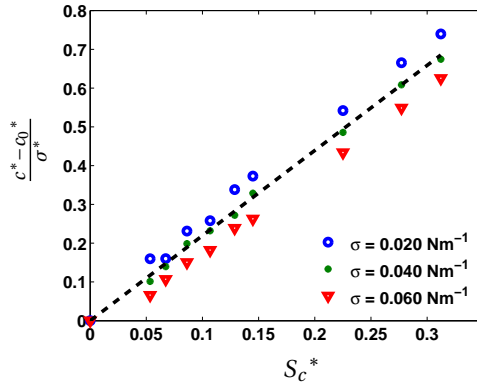


Figure 4.8: Steady state scaled incremental cohesion $\frac{c^* - c_0^*}{\sigma^*}$ as a function of S_c^* for different surface tension. The dotted line represents the fitting function given by Eq. 4.22.

This subsection shows that the macroscopic characteristics of the liquid bridge model are determined by the maximum interacting force between the particles and the rupture distance. The steady state cohesion scales linearly with the surface tension of liquid *i.e.* the maximum force between the particles. For a given maximum force, the cohesion scaled with the surface tension of liquid is also a linear function of the rupture distance of the liquid bridge.

4.3.2. MACROSCOPIC TORQUE ANALYSIS FROM THE MICRO PARAMETERS

The strength, cohesion and flow properties of granular materials are strongly influenced by the presence of capillary cohesion. Due to the cohesive properties of these wet materials, the shear stress increases and, as a result, partially saturated wet materials require higher torques for deformation (shear) *e.g.* in a shear cell. Loosely speaking, torque is a measure of the shear stress or force acting on the particles at the wall and thus can be used to find an estimate of shear stress in the shear band. To study solely the effect of capillary cohesion on the torque, the other parameters like the particle friction is kept very small in our simulations, with $\mu_p = 0.01$. Earlier studies [16, 29, 52, 53] show that the average torque acting on the rotating part of the shear cell increases with increasing moisture content. In this section we perform a detailed analysis of the macroscopic torque as a function of the micro parameters in order to understand its connection with the steady state cohesion of the material.

The walls and the bottom plates of the shear cell consist of particles with a prescribed position. The particles forming the inner wall are stationary while the particles forming the outer wall rotate around the z -axis with frequency Ω . All the particles forming the inner and outer wall are identified as $\mathcal{C}_{\text{inner}}$ and $\mathcal{C}_{\text{outer}}$, respectively. The micro torque is

calculated based on the contact forces on the fixed particles on the moving (outer) and stationary (inner) parts of the shear cell. Thus the net inner and outer torque are calculated by summing up the torques for all the contacts with respect to the axis of rotation of the shear cell. Note that the torque T_{outer} and T_{inner} are almost equal in magnitude and opposite in direction. The net torque is obtained from the average magnitude of the outer wall torque and the inner wall torque. We multiply the total torque by a factor of $\frac{2\pi}{\pi/6}$ in order to get the torque for the whole system from the obtained torque of our simulations in a 30° section. Thus the torque is given by:

$$\vec{T} = \frac{2\pi}{\pi/6} \times \frac{1}{2} \left[\left(\sum_{i=1}^N \sum_{j \in \mathcal{C}_{\text{outer}}} \vec{c}_{i,j} \times \vec{f}_{i,j} \right) - \left(\sum_{i=1}^N \sum_{j \in \mathcal{C}_{\text{inner}}} \vec{c}_{i,j} \times \vec{f}_{i,j} \right) \right], \quad (4.23)$$

4

where N represents the number of particles, \vec{c}_{ij} is the position of the contact point and \vec{f}_{ij} is the interaction force. Only the z -component of the torque vector T_z is of interest as required for shearing the cell in the angular direction. We compare the dynamic torque evolution in Figure 4.9 for different liquid bridge volumes 4 nl and 200 nl respectively. The torque evolution shown for 200 nl liquid bridge volume is consistently higher than that of 4 nl. Note that the torque evolution shown is upto a very short rotation of 0.03 times, to focus on the short time with a higher save count. The steady state is reached at a later stage (rotation of 0.08 times) [54] and our steady state analysis is done at an even later stage of rotation between 0.8 to 2 times of rotation. The results of torque evolution are qualitatively comparable with the experimental results as given by [54] where the rheology of weakly vibrated granular materials is explored.

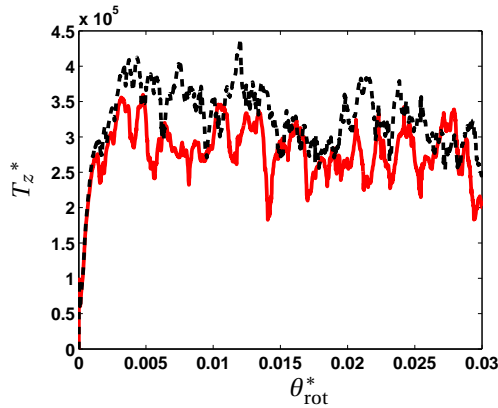


Figure 4.9: T_z^* as a function of scaled angular rotation $\theta_{rot}^* = \Omega \Delta t / 2\pi$ for surface tension of liquid $\gamma = 0.020 \text{ Nm}^{-1}$ for $V_b = 4 \text{ nl}$ (red solid) and $V_b = 200 \text{ nl}$ (black dash).

Figure 4.10 shows T_z^* as a function of σ^* for different liquid bridge volumes. We observe that the resultant torque depends linearly on the surface tension of the liquid. The fit parameter l from the figure, the rate of increase of torque with surface tension, depends on the liquid bridge volume. This fit parameter l scales with the interaction distance S_c^* (plot not shown here).

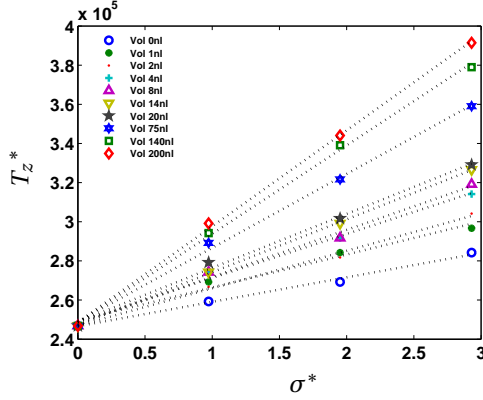


Figure 4.10: Steady state torque T_z^* as a function of σ^* . The dotted lines represent the fitting functions for different liquid bridge volumes given by equation $T_z^* = l\sigma^* + t$ where $t = 2.48 \times 10^5$ and l increases with increasing liquid bridge volume.

Next, we compare the results of the steady state cohesion as obtained from the fitting function explained in Sec. 4.3.1 with the calculated (measured) torque. We write the scalar form of the torque on the plane through the shear band center, derived from steady state cohesion as T_{macro} :

$$T_{\text{macro}} = \frac{1}{2} \left[\int_{A_o} r dA - \int_{A_i} r dA \right] (\mu P_{\text{avg}} + c), \quad (4.24)$$

where A_o denotes the outer wall surface, A_i denotes the inner wall surface and P_{avg} is the mean pressure inside the shear band approximately 250 Pa for a filling height of 36 mm. Here we calculate the average torque as a difference between the outer wall torque and the inner wall torque. Note that here we make an approximation of both the inner and outer wall shear stress to be equal to the mean shear stress inside the shear band $\mu P_{\text{avg}} + c$. In reality, the mean shear stress on the inner wall is much higher than the mean shear stress on the outer wall, thus balancing the net torque due to different areas. Figure 4.11 shows a comparison of the two torque given by the scalar z -component of Eq. 4.23 and Eq. 4.24 respectively as a function of rupture distance S_c^* , for surface tension of liquid 0.020 Nm^{-1} . Both torques increase linearly with the rupture distance, showing a good agreement. However, the torque calculated from the shear band stress T_{macro}^* is an outcome of many approximations. Thus, here we give more stress on the qualitative agreement of the two torque measured from different sources. The steady state cohesion is proportional to the measured torque. The latter is an experimentally measurable quantity and thus we can get an estimation of the steady state cohesion of the material from the experimentally measured torque.

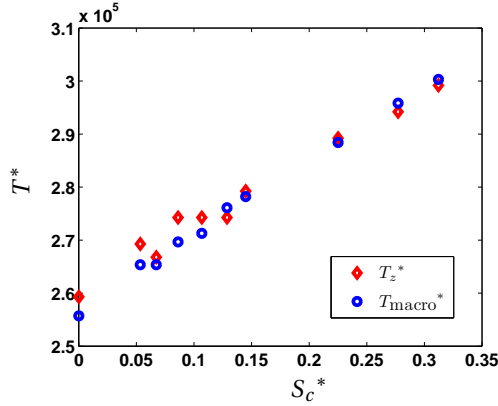


Figure 4.11: Torque calculated numerically from Eq. 4.23 scaled as T_z^* as compared with the scalar form of scaled macro torque T_{macro}^* as calculated from the shear stress at the center of the shear band, given by Eq. 4.24.

4.4. AN ANALOGOUS LINEAR ADHESIVE CONTACT MODEL FOR COHESIVE PARTICLES

In this section we aim to determine the key microscopic parameters for a linear contact model [42] that is macroscopically analogous to the liquid bridge contact model used before. An explanation of this linear adhesive contact model is given in [42]. The linear adhesive contact model is similar to the liquid bridge contact model in terms of a jump-in force and an irreversibility in the loading and unloading path. However, note that unlike the liquid bridge contact model, the force for the linear adhesive contact model has no finite force at the maximum interaction distance S_c^* . Thus, although we state the linear adhesive model as an analogous counter-part of the liquid bridge model, they are indeed not absolutely identical. Figure 4.12 shows the force-overlap distribution for the two contact models showing the loading and unloading directions of forces which are reversible at $\delta^* > 0$ and irreversible at $\delta^* < 0$ when the particles form new contacts. However, the path is reversible at $\delta^* < 0$ when the particles approach or move away from each other without rupture of the liquid bridge. Unlike the linear adhesive contact model, the capillary force in the liquid bridge contact model is a function of the interacting particle radius. Hence, a scattered distribution of force is observed in the liquid bridge contact model, as shown by the blue data in Figure 4.12.

As discussed in Sec. 4.3.1, the steady state cohesion for the liquid bridge model is controlled by the rupture distance of the liquid bridge, which is proportional to the liquid bridge volume, and the magnitude of the maximum interaction force, which is governed by the surface tension of the liquid. Assuming that the non-linear liquid bridge capillary force can be replaced by a simple linear adhesive force between the particles with the same macro characteristics, we compare the steady state cohesion of the two models in Sec. 4.4.1.

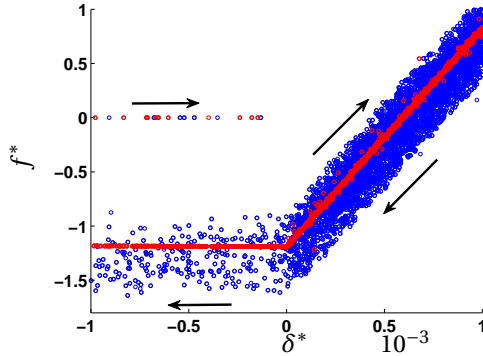


Figure 4.12: Force-overlap diagram for the liquid bridge model (blue) as compared with the analogous linear adhesive contact model (red), zoomed in near the contact point i.e. the rupture distance is at much larger negative values. The arrows show the loading and the unloading directions for all forces. The schematic diagram for the mentioned contact models are given in Figures 4.2 and 4.4 respectively.

4.4.1. EQUAL MAXIMUM FORCE AND INTERACTION DISTANCE

The key parameters that define the cohesive force of a linear adhesive contact model are the maximum adhesive force and the adhesive stiffness, see Eq. 4.15. Several simulations have been run for the linear adhesive contact model in the same numerical set-up with the same maximum adhesive force as used in the liquid bridge model ($(f_a^{\max})_{\text{liq}} = (f_a^{\max})_{\text{lin}}$) and adhesive stiffness that would result in the same interaction range for different liquid bridge volumes for different surface tension of liquid. The force-overlap for contacts with $\delta^* < 0$ for the two comparable contact models with equal interaction distance are shown in Figure 4.13. The adhesive stiffnesses that are equivalent to the liquid bridge volumes as given by Eq. 4.3 for surface tension $\sigma = 0.020 \text{ Nm}^{-1}$ for equal interaction distance are given by:

$$k_c \in [0.21, 0.26, 0.41, 0.46, 0.56, 0.69, 0.88, 1.11, \infty] \text{ Nm}^{-1} \quad (4.25)$$

The results for the steady state cohesion c^* , as scaled by σ^* for the liquid bridge model and the linear adhesive contact model are shown in Figure 4.15. The results are not really analogous as seen from the figure as the intercepts for the fitting lines of the two models are different, while they are parallel. The fitting parameters for the relation:

$$\frac{c^* - c_0^*}{\sigma^*} = gS_c^* + h \quad (4.26)$$

are $g = 2.1716$ and $h \approx 0$ for the liquid bridge contact model, $g = 2.0984$ and $h = 0.2226$ for the linear adhesive contact model.

So for a given liquid bridge volume and a given surface tension of liquid, the linear adhesive contact model with the same maximum force and same interaction distance has a higher cohesion.

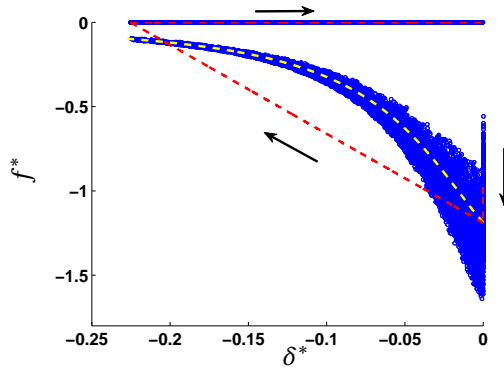


Figure 4.13: Scaled adhesive force f^* (f_a^* for linear adhesive model and f_c^* for liquid bridge model) as a function of δ^* for the linear adhesive contact model (red), compared with the liquid bridge model (blue), for equal maximum force and equal interaction distance. The yellow line represents the force for the liquid bridge contact model for mean particle diameter d_p as a function of δ^* . The arrows show the loading and the unloading directions for the short-range forces.

4

4.4.2. EQUAL MAXIMUM FORCE AND ADHESIVE ENERGY

Equal maximum force and interaction distance was discussed in Sec. 4.4.1, but here the steady state cohesion for the two models with an equal maximum adhesive force and equal adhesive energy E^* are considered. The total energy dissipated or the work done to pull-off the particles against adhesive force for a given contact model is obtained by the total area under the force-overlap relation for $\delta^* < 0$, see Figure 4.14. A linear adhesive contact model analogous to the liquid bridge contact model is obtained with the equal maximum force with surface tension $\sigma = 0.020 \text{ Nm}^{-1}$ and the adhesive stiffness adjusted to have the equal adhesive energy:

$$k_c \in [0.25, 0.29, 0.39, 0.74, 0.84, 1.10, 1.49, 2.11, 2.95, \infty] \text{ Nm}^{-1} \quad (4.27)$$

The force-overlap for contacts with $\delta^* < 0$ for the two comparable contact models with equal adhesive energy are shown in Figure 4.14. Figure 4.15 shows the dependence of $\frac{c^* - c_0^*}{\sigma^*}$ on rupture distance S_c^* for the liquid bridge model (blue), compared with the two cases of the linear adhesive contact model with equal interaction distance (red) and equal adhesive energy dissipated per contact (green). The linear contact model with equal energy has a lower interaction distance. The functional behavior of the steady state cohesion using the linear irreversible contact model for small interaction range can be understood from this. As observed from Figure 4.15, the cohesion is a non-linearly dependent on the rupture distance S_c^* at low interaction distance and becomes linear for higher range.

Figure 4.16 shows the dependence of steady state cohesion on total adhesive energy for the liquid bridge model, compared with the two cases of linear adhesive contact model with equal interaction distance (red) and equal adhesive energy dissipated per contact (green). As seen from the figure, for a given maximum force which is determined by the surface tension of the liquid, the steady state cohesion c^* is equal for the the liquid bridge model and the linear contact model with equal energy. The steady state

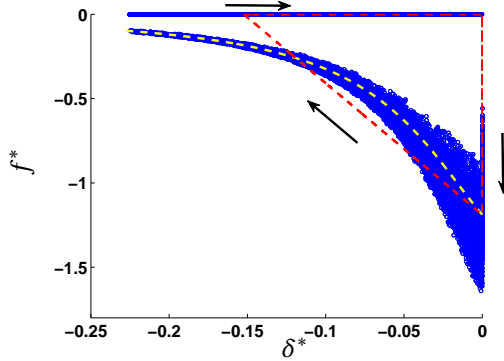


Figure 4.14: Scaled adhesive force f^* (f_a^* for linear adhesive model and f_c^* for liquid bridge model) as a function of δ^* for the linear adhesive contact model (red), compared with the liquid bridge model (blue), for equal maximum force and equal adhesive energy dissipated per contact. The yellow line represents the force for the liquid bridge contact model for mean particle diameter d_p as a function of δ^* . The arrows show the loading and the unloading directions for the short-range forces.

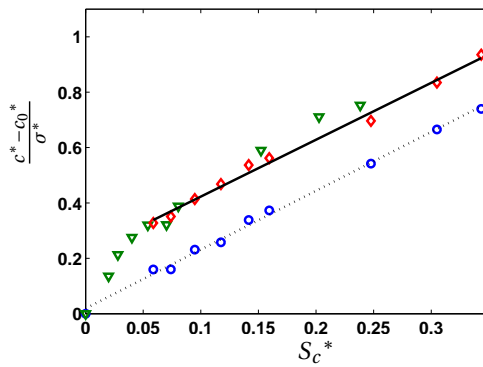


Figure 4.15: $\frac{c^* - c_0^*}{\sigma^*}$ as function of S_c^* for the liquid bridge model (blue) and the linear adhesive contact model with equal interaction distance (red) and equal adhesive energy dissipated per contact (green) for $\sigma = 0.020 \text{ Nm}^{-1}$. The dotted and the solid lines represent the fitting function given by Eq. 4.26 with $h = 0$ and $h = 0.2226$ respectively.

cohesion for the linear contact model with equal interaction distance is higher as it has higher adhesive energy than the liquid bridge model. However, all the data for the three cases as explained above collapse and functionally behave the same.

4.4.3. DIFFERENT MAXIMUM FORCE FOR THE TWO CONTACT MODELS

In the earlier subsections, results show that for a given maximum force the steady state cohesion for the two contact models functionally behave the same under equal force and equal energy conditions. To study the functional form for the two models under different maximum force conditions, we compare the macroscopic behavior of the linear adhesive contact model to the liquid bridge model results for different surface tension.

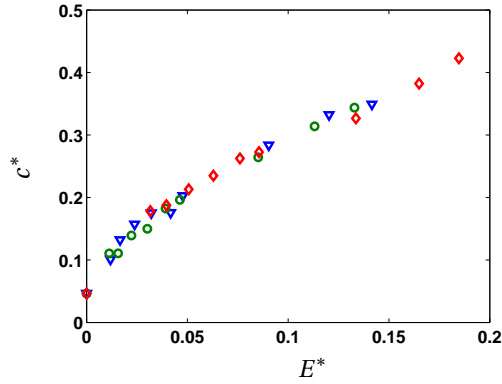


Figure 4.16: c^* as a function of E^* for the liquid bridge model (blue) and the linear adhesive contact model with equal interaction distance (red) and equal adhesive energy dissipated per contact (green) for $\sigma = 0.020 \text{ Nm}^{-1}$.

Linear model simulations equivalent to surface tension 0.040 Nm^{-1} and 0.060 Nm^{-1} are run with an equivalent adhesive stiffness 2 times and 3 times of that given by Eq. 4.25 keeping the interaction distance the same. Figure 4.17 shows a comparison of the force-overlap for the two contact models for surface tension of liquid 0.020 Nm^{-1} and 0.040 Nm^{-1} .

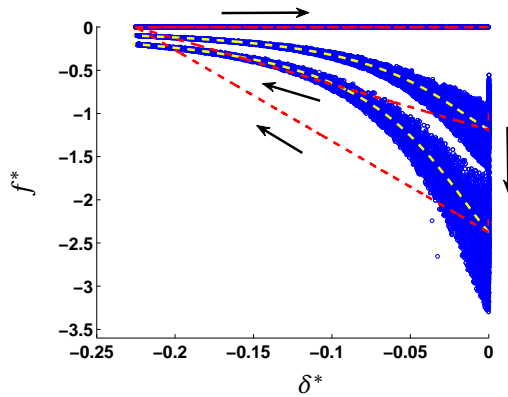


Figure 4.17: Scaled adhesive force f^* (f_a^* for linear adhesive model and f_c^* for liquid bridge model) as a function of δ^* for the linear adhesive contact model (red), compared with the liquid bridge model (blue) for different maximum force and equal interaction distance. The yellow lines represent the force for the liquid bridge contact model for mean particle diameter d_p as a function of δ^* . The arrows show the loading and the unloading directions for the short-range forces.

Figure 4.18(a) shows the dependence of steady state cohesion on the adhesive energy dissipated by the particles per contact for different f_a^{\max} for the liquid bridge model and the linear adhesive contact model. For the same energy dissipated per contact, a higher surface tension of the liquid results in a higher macroscopic cohesion. Figure 4.18(b)

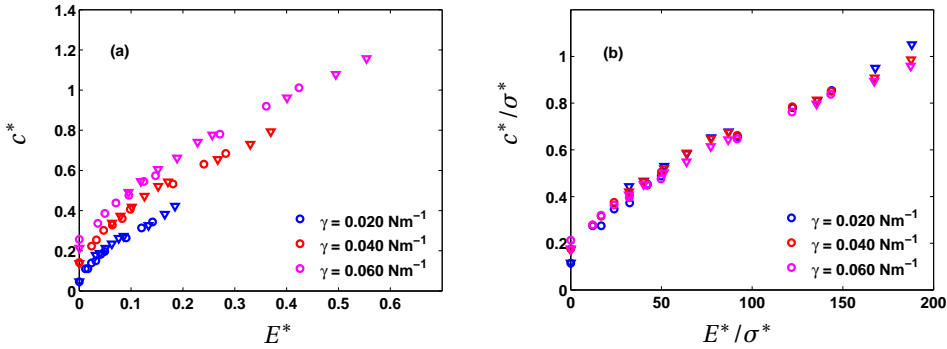


Figure 4.18: (a) c^* as a function of E^* for different surface tension of liquid. (b) $\frac{c^*}{\sigma^*}$ as a function of $\frac{E^*}{\sigma^*}$ for different surface tension of liquid as compared with the linear irreversible model. Different symbols denote \circ liquid bridge model and ∇ linear adhesive contact model.

shows that $\frac{c^*}{\sigma^*}$ is a function of $\frac{E^*}{\sigma^*}$ for a given surface tension, or maximum force.

4.5. CONCLUSION

We observed a correlation between the steady state cohesion and the microscopic parameters of the liquid bridge model. The micro-parameters are the liquid bridge volume, the liquid surface tension, the contact angle (which was kept constant) and the size of particles (i.e. curvature, which was also not varied). A detailed study of the effect of liquid bridge volume and surface tension of liquid is done in this paper. These microscopic parameters control the cohesion in wet granular materials in different ways. We found that the steady state cohesion of the system is proportional to the maximum adhesive force, which was varied by modifying the surface tension. On the other hand, we found that the steady state cohesion is also linearly dependent on the maximum interacting distance between the particles, which depends on the volume of the liquid bridge. From these results we have obtained a good micro-macro correlation between the steady state cohesion and the microscopic parameters studied.

We analyzed the effect of cohesion on the wall torque required to rotate the system at a given rate. The torque and the steady state cohesion of the system are proportional and show similar linear dependence on the microscopic parameters.

Finally, an analogy was established between the liquid bridge model and a simpler linear adhesive contact model; even though these two models have different micro-macro correlations, the steady state cohesion for the two models are the same if the maximum force and the total adhesive energy dissipated per contact for the two models are matched, irrespective of the shape of the attractive force function acting between the particles. In this way one can always replace a non-linear liquid bridge force by a simpler linear one and obtain identical macroscopic properties in less computational time.

Furthermore, results for the two types of contact models with equal energy and different magnitude of maximum force show that they have different steady state cohesion. Therefore, adhesive energy is not the sole microscopic condition for the two con-

tact models to have same steady state cohesion. Instead, we observe that both adhesive energy and cohesion scale linearly with the maximum adhesive force. In this way we can determine the steady state cohesion from the two microscopic parameters, the adhesive energy and the maximum force.

In this paper our study was focused on the micro-macro correlations and comparing different contact models. It would be interesting to also study the forces and their probability distributions for wet cohesive systems. Future studies will aim at understanding the microscopic origin and dynamics of the contacts and liquid bridges throughout the force network(s) and also the directional statistics of the inter-particle forces inside a shear band. The effect of liquid migration on the macro properties and a continuum description for a similar model will be studied in the near future.

4

REFERENCES

- [1] A. Singh, V. Magnanimo, K. Saitoh, S. Luding, *Physical Review E* **90**, 022202 (2014).
- [2] S. Roy, A. Singh, S. Luding, T. Weinhart, *Computational Particle Mechanics* **3**, 449 (2016).
- [3] N. Mitarai, H. Nakanishi, *Europhysics Letters* **88**, 64001 (2009).
- [4] S. Ulrich, T. Aspelmeier, K. Roeller, A. Fingerle, S. Herminghaus, A. Zippelius, *Physical Review Letters* **102**, 148002 (2009).
- [5] S. Strauch, S. Herminghaus, *Soft Matter* **8**, 8271 (2012).
- [6] N. Huang, G. Ovarlez, F. Bertrand, S. Rodts, P. Coussot, D. Bonn, *Physical Review Letters* **94**, 028301 (2005).
- [7] N. Huang, D. Bonn, *Journal of Fluid Mechanics* **590**, 497 (2007).
- [8] C. Bonnoit, J. Lanuza, A. Lindner, E. Clement, *Physical Review Letters* **105**, 108302 (2010).
- [9] D. Howell, R. Behringer, C. Veje, *Physical Review Letters* **82**, 5241 (1999).
- [10] W. Losert, L. Bocquet, T. Lubensky, J.P. Gollub, *Physical Review Letters* **85**, 1428 (2000).
- [11] A. Thornton, D. Krijgsman, R. Fransen, S. Gonzalez, D. Tunuguntla, A. te Voortwis, S. Luding, O. Bokhove, T. Weinhart, *EnginSoft's SBE&S Magazine* **10**, 48 (2013).
- [12] A. Thornton, T. Weinhart, S. Luding, O. Bokhove, *International Journal of Modern Physics C* **23**, 1240014 (2012).
- [13] P. Schall, M. van Hecke, *Annual Review Fluid Mechanics* **42**, 67 (2010).
- [14] D. Fenistein, M. van Hecke, *Nature* **425**, 256 (2003).
- [15] R. Schwarze, A. Gladkyy, F. Uhlig, S. Luding, *Granular Matter* **15**, 455 (2013).

- [16] A. Gladkyy, R. Schwarze, *Granular Matter* **16**, 911 (2014).
- [17] S. Herminghaus, *Advances in Physics* **54**, 221 (2005).
- [18] V. Richefeu, M.S.E. Youssofi, F. Radjai, *Theoretical and Numerical Unsaturated Soil Mechanics*, pp. 83–91 (2007).
- [19] P. Darabi, T. Li, K. Pougatch, M. Salcudean, D. Grecov, *Chemical Engineering Science* **65**, 4472 (2010).
- [20] R. Mani, D. Kadau, D. Or, H.J. Herrmann, *Physical Review Letters* **109**, 248001 (2012).
- [21] R. Mani, D. Kadau, H.J. Herrmann, *Granular Matter* **15**, 447 (2013).
- [22] C.D. Willett, M.J. Adams, S.A. Johnson, J.P. Seville, *Langmuir* **16**, 9396 (2000).
- [23] A.M. Alencar, E. Wolfe, S.V. Buldyrev, *Physical Review E* **74**, 026311 (2006).
- [24] V.A. Lubarda, *Acta Mechanica* **226**, 233 (2015).
- [25] F. Soulie, F. Cherblanc, M.S. El Youssofi, C. Saix, *International Journal for Numerical and Analytical Methods in Geomechanics* **30**, 213 (2006).
- [26] S. Schöllmann, *Physical Review E* **59**, 889 (1999).
- [27] X. Wang, H. Zhu, A. Yu, *Granular Matter* **14**, 411 (2012).
- [28] E. Woldhuis, B.P. Tighe, W. van Saarloos, *The European Physical Journal E: Soft Matter and Biological Physics* **28**, 73 (2009).
- [29] S. Roy, S. Luding, T. Weinhart, *Procedia Engineering* **102**, 1531 (2015).
- [30] A. Singh, V. Magnanimo, K. Saitoh, S. Luding, *New Journal of Physics* **17**, 043028 (2015).
- [31] M. Scheel, R. Seemann, M. Brinkmann, M. Di Michiel, A. Sheppard, B. Breidenbach, S. Herminghaus, *Nature Materials* **7**, 189 (2008).
- [32] N. Mitarai, F. Nori, *Advances in Physics* **55**, 1 (2006).
- [33] A. Denoth, *Journal of Glaciology* **28**, 357 (1982).
- [34] T. Weigert, S. Ripperger, *Particle & Particle Systems Characterization* **16**, 238 (1999).
- [35] H. Schubert, *Kapillarität in porösen Feststoffsystemen* (Springer, 1982).
- [36] M.A. Erle, D. Dyson, N.R. Morrow, *AIChE Journal* **17**, 115 (1971).
- [37] B. Derjaguin, *Colloid & Polymer Science* **69**, 155 (1934).
- [38] G. Lian, C. Thornton, M.J. Adams, *Journal of Colloid and Interface Science* **161**, 138 (1993).

- [39] S. Luding, *Particulate Science and Technology* **26**, 33 (2008).
- [40] S. Luding, *Particology* **6**, 501 (2008).
- [41] S. Luding, F. Alonso-Marroquín, *Granular Matter* **13**, 109 (2011).
- [42] A. Singh, V. Magnanimo, S. Luding, arXiv:1503.03720, to be re-submitted (2016).
- [43] J.F. Labuz, A. Zang, *Rock Mechanics and Rock Engineering* **45**, 975 (2012).
- [44] R.M. Nedderman, *Statics and kinematics of granular materials* (Cambridge University Press, 2005).
- [45] M. Budhu, *Soil Mechanics Fundamentals (Imperial Version)* (John Wiley & Sons, 2015).
- [46] X.L. Yang, J.H. Yin, *International Journal of Non-Linear Mechanics* **41**, 1000 (2006).
- [47] N. Berger, E. Azéma, J.F. Douce, F. Radjai, *Europhysics Letters* **112**, 64004 (2016).
- [48] F. Radjai, V. Richefeu, *Philosophical Transactions of the Royal Society of London A: Mathematical, Physical and Engineering Sciences* **367**, 5123 (2009).
- [49] C. Voivret, F. Radjai, J.Y. Delenne, M.S. El Youssoufi, *Physical Review Letters* **102**, 178001 (2009).
- [50] P. Rognon, J.N. Roux, D. Wolf, M. Naaïm, F. Chevoir, *Europhysics Letters* **74**, 644 (2006).
- [51] P.G. Rognon, J.N. Roux, M. Naaïm, F. Chevoir, *Journal of Fluid Mechanics* **596**, 21 (2008).
- [52] A. Bouwman, M. Henstra, J. Hegge, Z. Zhang, A. Ingram, J. Seville, H. Frijlink, *Pharmaceutical Research* **22**, 270 (2005).
- [53] A. Obraniak, T. Gluba, *Physicochemical Problems of Mineral Processing* **48**, 121 (2012).
- [54] G.H. Wortel, J.A. Dijkstra, M. van Hecke, *Physical Review E* **89**, 012202 (2014).
- [55] S. Eckhard, M. Fries, S. Antonyuk, S. Heinrich, *Advanced Powder Technology* **28**, 185–196 (2017).
- [56] M. Dosta, S. Dale, S. Antonyuk, C. Wassgren, S. Heinrich, *Powder Technology* **299**, 87–97 (2016).

5

LIQUID RE-DISTRIBUTION IN SHEARED WET GRANULAR MEDIA

Shearing wet granular systems causes a re-distribution of the interstitial liquid, which can change the material's bulk behavior. Using the Discrete Element Method (DEM), we study the early transients, the intermediate states and the long-term evolution of liquid re-distribution for various material parameters and two different initial wetting conditions in an inhomogeneous split-bottom ring-shear cell featuring a wide shear-band away from the system walls. In our model, liquid exists in two states, either in liquid bridges between particles or in liquid films on the particle surfaces. Under deformations like shear, the liquid is re-distributed due to the rupture of existing and formation of new liquid bridges. As new model parameter, a liquid bridge limit-volume is imposed to avoid clustering of liquid.

Studying the effect of the local shear rate on the liquid re-distribution, two distinct effects are observed: For small amounts of shear, i.e. small strain amplitude, the interstitial liquid is randomly re-distributed locally, while for larger amounts of shear, liquid is transported diffusively away from the shear zone. The local re-distribution quickly results in a characteristic probability distribution of liquid bridge volumes, independent of the initial wetting conditions, while the mean liquid bridge volume depends on the limit-volume. Although the shear driven diffusive liquid transport is active from the beginning, it dominates the transport on the long term, when the liquid moves out of the shear band, making the shear band dry. Ongoing theoretical analysis suggest a competition of drift and diffusive mechanisms in a different set of coordinates that can explain our observations.

5.1. INTRODUCTION

The microstructure of confined granular media is typically inhomogeneous, anisotropic and disordered [1, 2]. Under external loading, these systems exhibit a non-equilibrium jamming transition from a solid-like to a liquid-like state [3–5] when the applied shear

Roy, S., Luding, S. and Weinhart, T., Liquid re-distribution in sheared wet granular media, submitted.

stress or energy exceeds the shear resistance or inter-particle energy, and materials start to flow. The microstructure is disturbed and re-arranged completely during this process. Thus, the internal structure of the granular medium changes continuously when subjected to shear. This internal structure is influenced by polydispersity, related structural features and frictional properties of the granular particles, which thus play a crucial role in determining their flow dynamics [6–9]. For example, shear tests of both drained and undrained sand show a state transformation, depending on the initial packing density, before it reaches a critical state [10–12]. This state transformation corresponds to a local maximum in the evolution of the coordination number. In a typical consolidated-drained condition, the pore water can drain out of the soil easily, causing volumetric strains in the soil and reaching the same critical state irrespective of the initial configuration.

Wet granular media are collections of grains containing unsaturated interstitial fluid, with athermal interactions through cohesive capillary, repulsive elastic and dissipative contact forces. These capillary interactions are dependent on intrinsic properties of the contact force model, namely, the maximum capillary force and the maximum interaction distance [13]. External forces lead to granular flow if the applied shear stress exceeds the yield stress, eventually leading to a lower critical state shear stress after finite shear strain [14–16]. A simple constitutive relation for the critical-state shear stress is constituted by the bulk cohesion and the macro friction coefficient [13, 17]. The bulk cohesion is correlated with the *Bond number* or *adhesion index*, measured as the squared ratio of stress to wetting time scales [13, 18]. This bulk cohesion was analysed in terms of the force and fabric anisotropies [18] for wet granular materials. In our previous studies, a generalized rheology shows that the steady-state shear stress is factorized into a product of functions of different dimensionless numbers [16, 19], if a simplistic situation is assumed where all contacts have an equal liquid bridge volume. The liquid in the system is thus not treated as a separate entity, rather the contact model takes into account the effect of liquid capillary bridges.

Recent results by Mani et al. [20] show from experiments and simulations that the liquid content decreases within wet shear bands. This is a diffusion-driven phenomenon occurring at larger amount of shear, which causes the liquid to be transported away from the shear band. However, much remains unexplored on the initial re-distribution of the liquid which happens within a smaller shear strain and is one major focus of our discussion. Within small shear strain, the liquid volume is conserved within the shear band, while the liquid is locally re-distributed. This prompts us to look for a liquid migration model in our DEM simulations where liquid moves between contacts due to shear-driven liquid bridge formation and rupture. Note that liquid transport fluxes are also driven by Laplace pressure changes [21–24], either through the vapor phase or through the wetting layers on the beads [25]. However, this mode of liquid transport is excluded from the discussion in this paper.

Understanding the role of shear on the re-distribution of liquid in wet granular materials is of considerable technological importance for applications in many fields, such as civil engineering, pharmaceutical research, agronomy, etc., especially in process equipments subjected to inhomogeneous shear. One important application is the flow in industrial mixers and granulators. Note that, the initial liquid distribution can vary signifi-

cantly: initial homogeneous liquid bridge volume in all contacts is observed if the initial wet sample is prepared by allowing equilibration by suction before shear. Conversely, another extreme situation is observed if all liquids are present in form of liquid films and the initial sample is given minimum equilibration time before shear [20]. We study here the transients of liquid re-distribution upon shear, considering these two extremes of initial conditions. The question that comes to our mind is whether the liquid distribution reaches a steady (or critical) state which is independent of the initial configuration. In order to check this, we are investigating here the transient of liquid re-distribution for wet granular media, after both small and large shear strains.

The paper is organized as follows: Section 5.2 describes the geometry of the system, details of the contact force models, the liquid migration model, and the different initial conditions for our simulations. Section 5.3 presents the methodology for the micro-macro transition in the transient state and for locating the shear band in the system. Section 5.4.1 and 5.4.2 describe our results giving an illustration of the small shear transients of liquid re-distribution from different initial conditions towards an intermediate pseudo-critical state of liquid distribution. Furthermore, we describe the effect of the different parameters, e.g., the width of the shear band, liquid bridge limit-volume on the transient evolution as well as intermediate pseudo-critical state and the saturation in Section 5.4.3, 5.4.4 and 5.4.5, respectively. Finally, Section 5.4.6 gives an overview of the state beyond the liquid re-distribution transient when the liquid migrates out of the shear band by a shear rate dependent diffusive process on very large shears. We draw our conclusions in Section 5.5.

5.2. SYSTEM

5.2.1. GEOMETRY

The set-up used for simulations consists of a shear cell with annular geometry and a split in the bottom plate, as explained in [13, 15, 16, 19, 26–28, 30, 32]. The system consists of an outer cylinder (radius $R_o = 110$ mm) rotating around a fixed inner cylinder (radius $R_i = 14.7$ mm) with a rotation frequency of $\Omega = 0.19$ s⁻¹. Note that we use a relatively fast rotation to save our computational time. However, this is well below the dynamic flow limit. The granular material is confined by gravity between the two concentric cylinders and the bottom plate, with a free top surface. The bottom plate is split at radius $R_s = 85$ mm into a moving outer part and a static inner part. Due to the split at the bottom, a shear band is formed at the bottom at R_s . It moves inwards and widens with increasing height, due to the geometry. This set-up features a wide shear band away from the wall, free from boundary effects, if an intermediate filling height ($H \approx 40$ mm) is chosen. The focus of our study here is the liquid re-distribution inside the system and the shear band in particular. While earlier simulations were done with a angular section of 90° [14, 28, 30, 32] or 30° [13, 16, 19], very few simulations are done using the whole shear cell [31, 33].

5.2.2. DEM MODEL

Our approach towards a microscopic understanding of macroscopic particulate material behavior is the modeling of particles using the so-called discrete element method

(DEM). We use the open source code MercuryDPM [34, 35] and in the following subsections, describe the particles and the contact model for our DEM simulations.

PARTICLES

The annular space in the split bottom geometry mentioned above is filled with $N = 133892$ polydispersed spherical glass beads with density $\rho_p = 2000 \text{ kg m}^{-3}$ up to height $H \approx 40 \text{ mm}$. The particle mean diameter is $r_p = \langle r \rangle = 1.1 \text{ mm}$ and a homogeneous size distribution with $r_{\min}/r_{\max} = 1/2$ and width $1 - \langle r \rangle^2 / \langle r^2 \rangle \approx 0.04$ is chosen.

CONTACT MODEL FOR WET PARTICLES

We use a phenomenological contact model combining a linear visco-elastic repulsive force and a hysteretic non-linear liquid bridge capillary force proposed by Willet et al. [36] based on the particle specifications, contact properties, liquid properties and liquid saturation in the system [13]. The normal contact force between particles i and j is characterized by the linear elastic repulsive and dissipative forces and is given by $f_n^{i,j} = k\delta - \gamma_o\dot{\delta}$. The capillary force $f_c^{i,j}$ between particles i and j is given as:

$$f_c^{i,j} = \frac{f_c^{\max} \frac{r_{\text{eff}}}{r_p}}{1 + 1.05\bar{S} + 2.5\bar{S}^2}, \quad (5.1)$$

where the separation distance is normalised as $\bar{S} = S\sqrt{(r_p/V_b)}$, $S = \max(0, |\vec{r}_i - \vec{r}_j| - (r_i + r_j))$ being the separation distance between two particles i and j , where \vec{r}_i and \vec{r}_j are the position vectors of the two particles respectively. The effective radius r_{eff} of the two interacting spherical particles can be estimated as the harmonic mean of the two particle radii r_i and r_j according to the Derjaguin approximation [37], yielding the effective radius:

$$r_{\text{eff}} = \frac{2r_i r_j}{r_i + r_j}. \quad (5.2)$$

The maximum capillary force between the particles when they are in contact ($S = 0$) is given by $f_c^{\max} = 2\pi r_p \sigma \cos\theta$.

The adhesive force of the contact model is determined by three parameters: surface tension σ and contact angle θ of the liquid (both of which determine the maximum adhesive force) and the liquid bridge volume V_b (which determines how the force depends on the separation distance) [13]. The error of this capillary force model is within the limit of the 4% for the liquid bridge limit-volume $V_{\max} = 0.001 r_p^3$ [36]. The fixed parameters of the contact model are given in Table 5.1. Bridges form when particles come into contact, and rupture when the separation distance exceeds S_c . As proposed by Lian et al. [38], the critical separation distance S_c at which the bridge ruptures is given by:

$$S_c = \left(1 + \frac{\theta}{2}\right) V_b^{1/3} \quad (5.3)$$

Table 5.1: Parameters

Description	Quantity
Surface Tension (σ)	0.01 Nm^{-1}
Elastic stiffness (k)	120 Nm^{-1}
Contact angle (θ)	20°
Sliding friction coefficient (μ_p)	0.01
Viscous damping coefficient (γ_o)	$5 \times 10^{-3} \text{ kgs}^{-1}$

5.2.3. LIQUID MIGRATION MODEL

In our present study, we extend this model to account for liquid migration [13, 16, 19]. The methodology is quite straightforward as proposed by Mani et al. [20, 39]: liquid is transferred locally whenever contacts are formed or broken. The particles and the liquid are considered two different entities in the system. Liquid is either associated with a particle as a thin liquid film of volume V_f^i , or with a contact as a liquid bridge of volume V_b^{ij} . We describe the liquid migration model in the following sub-sections.

LIQUID BRIDGE FORMATION

When two particles come into contact (i.e. overlap), a new liquid bridge is formed from the liquid contained in the particle films. Since there can be some liquid volume V_{\min} trapped in the roughness of the grains [24, 40], to contribute, V_f^i must be larger or equal to V_{\min} . Therefore, the available liquid for bridge formation is $V_f^i - V_{\min}$. Since, V_{\min} is fixed and trapped in the particles, without loss of generality, we assume $V_{\min} = 0$ for our simulations. The volume V_b^{ij} transferred to the liquid bridge is therefore:

$$V_b^{ij} = \min(V_f^i + V_f^j, V_{\max}), \quad (5.4)$$

where $V_{\max} = \beta r_p^3$ is the liquid bridge limit-volume, imposed in our simulations as an additional parameter to avoid unbounded clustering of liquid by coalescence. This model is designed for small liquid contents and large contact angles with fast and easy transport of fluid on the surface. Figure 5.1 shows a schematic figure of liquid bridge formation.

The excess volume, $V_f^i + V_f^j - V_b^{ij}$ remains as film volume in the interacting particles, in proportion to the existing volume per particle. The appropriate value for V_{\max} can be estimated by different arguments. An upper bound for β is due to the maximal pore-space available, which implies for random close packing of monodisperse spheres that $\beta \approx 0.33$, if all pore space would be filled by liquid. However, we rather assume poor saturation and localisation of liquid at the contacts, and thus consider, following the arguments from [40], that $\beta = 0.058$. Thus, liquid bridges remain in the pendular limit, filling less than 6% of the pore space [36, 40]. Beyond the pendular regime, a considerably more complex expression for the liquid bridge force is given for greater volumes and contact angles [36], however, the difference to our simple expression is below 20% even for much larger β , so that we refrain from using a too complex expression and stick to

Eq.5.1. The local attractive force, as quantified by the Bond number Bo , does not change with liquid volume for either capillary force model, and only few liquid bridges are assumed to grow really large. Nevertheless, we explore below the effect of the maximum volume V_{\max} on the liquid re-distribution, using different β in the range:

$$\beta \in [0.03, 0.08, 0.15, 0.23, 0.45, 0.60]. \quad (5.5)$$

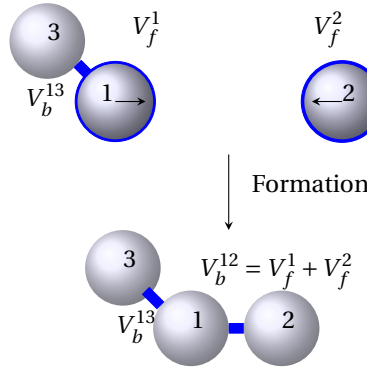


Figure 5.1: Liquid bridge formation ($V_b^{12} < V_{\max}$).

LIQUID BRIDGE RUPTURE

When the distance between two particles i and j with a liquid bridge in between exceeds the rupture distance of the liquid bridge, the liquid bridge ruptures and the bridge volume is distributed to the neighboring contacts:

$$V_b^{mn,new} = \min(V_b^{mn,old} + V_b^{ij} / (2N_c^m), V_{\max}), \quad (5.6)$$

where $m \in i, j$ and n denotes the neighboring particles in contact and N_c^m is the number of neighboring contacts associated with the particles m . Figure 5.2 shows a schematic representation of liquid bridge rupture. If the maximum volume V_{\max} is reached, the remaining liquid is added to the film volumes V_f^i and V_f^j . Thus, total liquid volume conservation is ensured.

5.2.4. INITIAL CONDITIONS

We begin our simulations with a pre-shear preparation history, where we allow particles to fall freely into the system under gravity. At this stage, particles are dry without any liquid on them. After free falling, the particles are allowed to relax to reach a ratio of kinetic to potential energy below 10^{-3} . After relaxation, the kinetic energy of the system becomes negligible while there is still a finite elastic potential energy, which contributes to the total energy of the sample. After the complete preparation and relaxation of the sample, we add liquids to the particles and start shearing. The potential energy of the

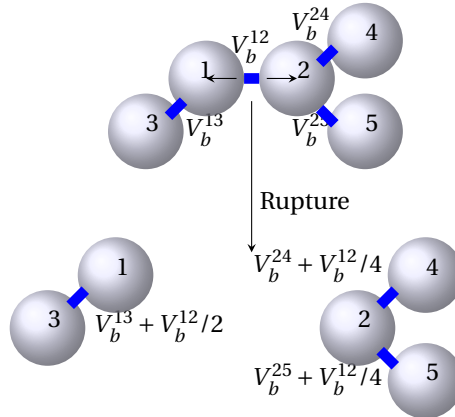


Figure 5.2: Liquid bridge rupture ($V_b^{ij,new} < V_{max}$, where $i \in 1, 2$ and $j \in 3, 4, 5$).

sample is increasing after addition of the liquid, depending on the saturation, while the kinetic energy remains the same at the commencement of shear.

At the commencement of shear, each particle is assigned with an initial liquid film volume V_f^0 . If not specified otherwise, we have $V_f^0 = 50$ nl in our system for standard simulations discussed in this paper. On shearing, the kinetic energy increases drastically and the elastic potential energy changes slowly until they reach a steady state. In order to understand how liquid re-distributes, we simulate the two extreme cases of initial liquid distribution: (i) 100% liquid distribution in the form of liquid films (**initial condition A**) and (ii) 100% liquid distribution in the form of liquid bridges (**initial condition B**). Initial condition A is initialized by distributing the total amount of liquid volume uniformly among all the particles as liquid film at the start of the simulation. This amounts to $V_f^0 = 50$ nl liquid film volume per particle. Initial condition B is done by distributing the same amount of liquid volume as in initial condition A, uniformly among all the existing contacts as liquid bridges. The contacts here include both the physical contacts and the long distance interacting contacts between the particles that are within the range of rupture distance of the liquid bridge. It is obvious that when the wet sample is allowed with long equilibration time, even the long distance interacting contacts would be filled in with liquid bridges due to suction pressure gradient. Thus, it is a logical assumption to distribute the liquid into not only the mechanical contacts, but also the long range interaction contacts within the range of rupture distance of the liquid bridge.

Granular materials with interstitial liquid can be classified as dry bulk, adsorption layers, pendular state, funicular state, capillary state, or suspension, depending on the level of saturation [41, 42]. In our present work, we intend to study the phenomenology of liquid bridge re-distribution between particles in the pendular state, where well-separated liquid bridges exist individually, without geometrical overlap. In order to study the influence of liquid content on the liquid re-distribution, we vary the initial liquid film

volume V_f^0 on the particles given as :

$$V_f^0 \in [10, 20, 40, 50, 80, 100] \text{ nl} \quad (5.7)$$

While varying V_f^0 , we keep the liquid bridge limit-volume constant with $V_{\max} = 40$ nl ($\beta = 0.03$). While varying β according to Eq. 5.5, we keep the initial liquid film volume constant with $V_f^0 = 50$ nl. As a standard simulation in this paper, we keep the initial liquid film volume $V_f^0 = 50$ nl and the liquid bridge limit-volume constant with $\beta = 0.03$, if not specified otherwise. The bulk saturation is 1.28% for this standard case, with a bulk porosity of $\epsilon \approx 0.35$ measured from the simulations.

5.3. MICRO-MACRO TRANSITION

To extract macroscopic properties from DEM, we use the spatial coarse-graining approach. This technique was used earlier in [14, 30, 32] The averaging is performed over toroidal volumes, over several snapshots of time, assuming rotational invariance in the tangential direction. The averaging procedure for a three dimensional system is explained in [13, 15]. The simulation is run for a total time of 22 s and transient data are obtained by temporal averaging of every 5 snapshots with a step of 0.015 s, starting from the onset of the shear. We obtain the macroscopic local quantities like shear rate $\dot{\gamma}$, liquid bridge volume V_b , liquid film volume V_f and the contact number C_w for further analysis. We distinguish between the contacts with liquid bridges and without which is significant for wet granular materials.

5.3.1. IDENTIFYING THE SHEAR BAND

We analyze the evolution of the liquid bridge volumes for initial conditions A and B as explained in Section 5.2.4. The objective is to study the transients of liquid re-distribution under shear. Thus, we focus on the region inside the shear band where dry systems reach a critical state after large enough shear. We define the shear band region by accumulating all local points having shear rate higher than a threshold value. This threshold value varies at every height and is defined as a fraction α of the maximum shear rate at the center of the shear band at a given height, $\dot{\gamma}_{\max}(z)$. Thus, we consider the shear band region as all local points having shear rate $\dot{\gamma}(r, z) \geq \alpha \dot{\gamma}_{\max}(z)$ as shown in Figure 5.3. For dry granular systems, the critical state is achieved at a constant pressure p and local shear rate condition over regions with shear rate larger than a certain α (dependent on the duration of shear) corresponding to the region of system that was sufficiently sheared to be re-structured.

5.3.2. WET SHEAR BAND PHENOMENOLOGY

While the shear band is well established above this shear rate for wet granular materials also, our analysis of liquid re-distribution shown in the latter sections are averaged over the shear band region corresponding to $\alpha = 0.4$ at different heights in the system. Additionally, the relative shear rate threshold α is varied from 0 to 0.8 to inversely vary the width of the shear band to see its effect. Thereby, we extract local data (shown by the red dots) corresponding to the regions as marked by the shaded area in Figure 5.3. We see

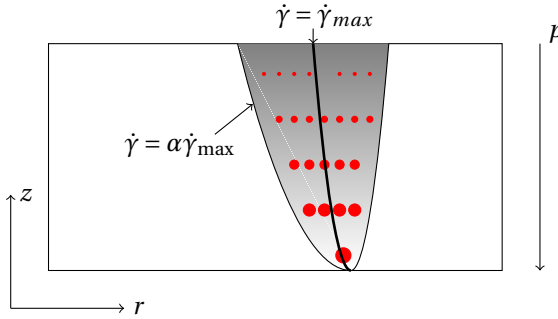


Figure 5.3: Schematic diagram of simulation set-up showing the shear band. Red dots showing the local points for our analysis with size of the dots given by the local pressure. The grey shaded area denotes the shear band ($\dot{\gamma} > \alpha \dot{\gamma}_{max}$) and the bold line shows the shear band center ($\dot{\gamma} = \dot{\gamma}_{max}$).

the evolution of the macro quantities like the mean liquid bridge volume $\langle V_b \rangle$ and the contact number C_w corresponding to the region inside the shear band as a function of local shear γ . We then analyse the transients for the shear band evolution to obtain the transients for liquid re-distribution inside the shear band.

5.4. RESULTS

5.4.1. TRANSIENTS FOR LIQUID RE-DISTRIBUTION

In this section, we describe the transients for liquid re-distribution for unsaturated granular materials subjected to shear with different initial conditions for initial conditions A and B as explained earlier. For our analysis on the re-distribution of the liquid bridges, we obtain the histogram distribution of the liquid bridge volume at different times with 100 bins of the histograms. We show the overlay of the histograms of liquid bridge volume distribution at different times with lines instead of the bars as shown in Figure 5.4.

We obtain the global shear $\gamma_g = 2\pi R_o \Omega \Delta t / (R_o - R_i)$ by scaling the distance traversed by a particle on the outer wall $2\pi R_o \Omega \Delta t$ in time Δt by the distance between the annular space $R_o - R_i$. We use that scaling factor as this is very simple and dependent on the geometry of the system. There can be other length scales like the the width of shear band, which is about half this geometry dependent scale $R_o - R_i$, or the particle diameter $2r_p$ which is about 40 times smaller. Figure 5.5(a) shows the evolution of liquid bridge volume distribution over global shear γ_g for initial condition A. Initially, the mean distribution of liquid bridge volume is lower than the intermediate pseudo-critical state distribution of liquid bridge volume. The system starts with all liquid volumes in the form of liquid film and hence the initial liquid bridge distribution number is lower than the intermediate pseudo-critical state. The smaller liquid bridge volumes have a higher count than the larger liquid bridge volumes but an accumulation in number of the liquid bridge limit-volumes ($V_b = V_{max}$) is found. With increasing shear, liquid from the bridges with limit-volume is re-distributed to the smaller liquid bridges, so that the overall liquid volume is almost conserved inside the shear band in this small shear strain.

Figure 5.5(b) shows the liquid bridge volume re-distribution over global shear for initial condition B. Initially, the distribution of liquid bridge volume is non-uniform, with

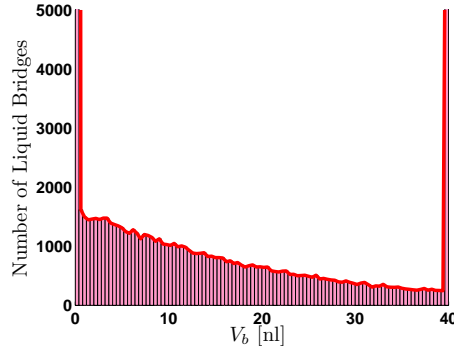


Figure 5.4: Overlaying of the histogram of liquid bridge volume distribution with lines for $\dot{\gamma}(r, z) \geq \alpha \dot{\gamma}_{\max}(z)$ and $\alpha = 0.4$ after 6.03 s ($\gamma_g = 8.23$) for initial condition A.

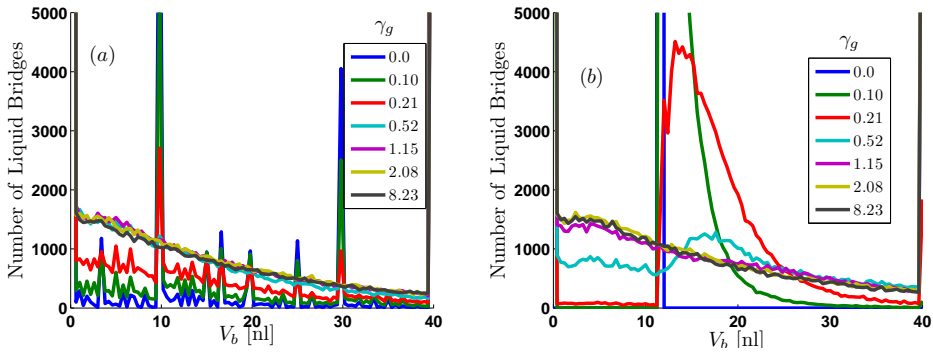


Figure 5.5: Liquid bridge volume distribution for different initial conditions (a) 100% liquid film (initial condition A) and (b) 100% liquid bridge (initial condition B) for $\dot{\gamma}(r, z) \geq \alpha \dot{\gamma}_{\max}(z)$ and $\alpha = 0.4$.

a high count of the intermediate liquid bridge volumes between 10 to 20 nl (higher than the intermediate pseudo-critical state), the initial liquid bridge volume being $V_b^0 \approx 11$ nl. Other liquid bridges have lower count (lower than the intermediate pseudo-critical state) at the initial state. With increasing global shear, liquid from the intermediate volume of liquid bridges are re-distributed to other liquid bridges and the overall liquid volume is conserved inside the shear band in this small shear strain. Comparing Figure 5.5(a) and (b), it is observed that initial condition A reaches the equilibrium state faster than initial condition B. Note that the local shear γ inside the shear band center and near the split position of the shear cell is of the same order and approximately 2 times the value of the global shear γ_g . Thus, the legends shown in Figure 5.5(a) and (b) in terms of global shear are not the quantitative representation of the local shear inside the shear band. The evolution of the two limits, the number of contacts with $V_b = 0$ (given by the red and blue \diamond) and $V_b = V_{\max}$ (given by the red and blue \circ) are shown in Figure 5.6. Irrespective of the different transients behavior, both the number of dry contacts and the contacts with liquid bridge limit-volume reach the same value given by the plateau in the intermediate

pseudo-critical state.

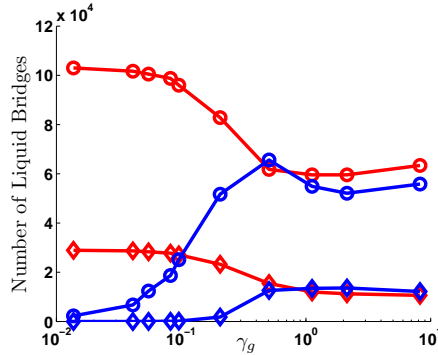


Figure 5.6: Number of dry contacts $V_b = 0$ for initial conditions A and B (red and blue \circ respectively) and number of liquid bridges of volume $V_b = V_{\max}$ for initial conditions A and B (red and blue \diamond , respectively) as a function of global shear γ_g for $\dot{\gamma}(r, z) \geq \alpha \dot{\gamma}_{\max}(z)$ and $\alpha = 0.4$.

Figure 5.6 shows the number of dry contacts for initial conditions A and B (given by the red and blue \circ) and the number of maximal liquid bridge contacts for initial conditions A and B (given by the red and blue \diamond) as a function of the global shear γ_g . Irrespective of the different transients behavior, both the number of dry contacts and the maximal liquid bridge contacts reach the same value given by the plateau in the intermediate pseudo-critical state.

5.4.2. LIQUID RE-DISTRIBUTION IN PSEUDO-CRITICAL STATE

Liquid re-distribution in unsaturated granular media is associated with the formation of new liquid bridges and the rupture of existing liquid bridges. Figure 5.7 shows a comparison of the distribution of the liquid bridge volumes after 6.01 s for the two different initial conditions A and B. Evidently, an intermediate state is reached where the rate of liquid bridge formation is balanced by the rate of liquid bridge rupture and is arrived, irrespective of the initial distribution of the liquid in the system. Here, we focus at the whole shear band region ($\dot{\gamma}(r, z) > 0.4 \dot{\gamma}_{\max}(z)$), and confirm that the system reaches an intermediate state independent of the initial conditions. In Section 5.4.3 we focus on the liquid re-distribution in the different regions of the shear band.

Figure 5.8(a) shows the mean liquid bridge volume per wet contact $\langle V_b \rangle$ as a function of local shear inside the shear band for initial conditions A and B. For each initial condition, the data points collapse onto a single curve. Figure 5.8(b) shows the wet contacts per particle C_w as a function of shear for initial conditions A and B. Again, the data collapse for each initial condition. Thus, the change in mean liquid bridge volume per wet contact over shear observed inside the shear band center for initial conditions A and B is an intrinsic phenomenon undergone by each local point inside the shear band before they reach the intermediate pseudo-critical state. Initial condition A shows a decrease in mean liquid bridge volume per contact with increasing shear. This can be related to Figure 5.5(a) as the liquid bridge limit-volumes (V_{\max}) are distributed to more number of smaller bridges until they reach the intermediate pseudo-critical value. Starting with an

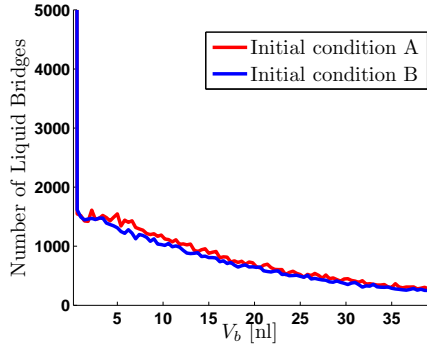


Figure 5.7: Overlay of the liquid bridge volume distribution for initial condition A (red) and initial condition B (blue) for $\dot{\gamma}(r, z) \geq \alpha \dot{\gamma}_{\max}(z)$ and $\alpha = 0.4$ after 6.03 s ($\gamma_g = 8.23$).

5

initial uniform liquid bridge volume distribution of $V_b^0 \approx 11$ nl, initial condition B shows an initial increase in mean liquid bridge volume per contact with increasing shear until it reaches a peak mean volume of liquid bridge approximately $V_b^p \approx 28$ nl. Further, the mean liquid volume per contact decreases with increasing shear until they reach the intermediate pseudo-critical state $V_b^c \approx 17$ nl. Both initial conditions A and B reach the same intermediate state in terms of mean liquid bridge volume per wet contact. The number of wet contacts per particle show an inverse functional behavior as $\langle V_b \rangle$, as the liquid saturation remains constant, but reach the same intermediate state too for initial conditions A and B. The total elastic potential energy of the system also reaches the same state for the two initial conditions, irrespective of the different energy they have in the transients, which depends on the number of dry and wet contacts in the transients.

During the process of re-distribution of liquid, the liquid volume is approximately conserved inside the shear band within small shear strain, when diffusion is less dominating than drift. The liquid bridge volumes are re-distributed during the process of contact breaking and formation. For initial condition A, as observed in Figure 5.6, a significant number of liquid bridges have the limit-volume. Subsequently, more smaller liquid bridges are formed at the cost of rupture of these critical volume liquid bridges, resulting in an increase in the number of wet contacts per particle and a decrease in the mean liquid bridge volume per wet contact as shown in Figure 5.8(a) and (b). For initial condition B, as observed from Figure 5.5(b) and 5.6, the number of liquid bridges with higher liquid volume initially increases with time. In the initial state, all the contacts have an equal liquid bridge volume V_b^0 . When subjected to shear, many contacts break, resulting in distributing the liquid to the neighboring contacts, making them grow in liquid bridge volume content. Hence, here the mean liquid bridge volume increases at the cost of breaking contacts. Simultaneously, the number of wet contacts C_w decreases as shown in Figure 5.8(b). Thus, in this initial condition wet contacts are subjected to shear break or rupture more or less instantaneously, distributing the liquid to the neighboring existing contacts and resulting in a rapid increase in mean liquid bridge volume and a decrease in the number of wet contacts before equilibrating towards the pseudo-critical state.

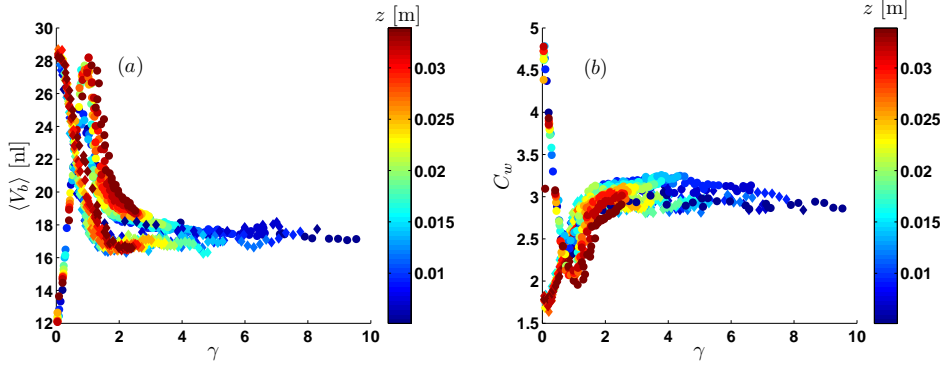


Figure 5.8: (a) Mean liquid bridge volume per contact $\langle V_b \rangle$ as a function of shear for initial condition A (\diamond) and initial condition B (\circ) and (b) wet contacts per particle C_w as a function of shear for initial condition A (\diamond) and initial condition B (\circ) for $\beta = 0.03$ nl, for $\dot{\gamma}(r, z) \geq \alpha \dot{\gamma}_{\max}(z)$ and $\alpha = 0.4$. Different colors indicate different heights.

5.4.3. DEPENDENCE ON THE RELATIVE SHEAR RATE THRESHOLD

As explained in Sec. 5.3.1, we define the shear band region by accumulating all local points having shear rate higher than a threshold value. This threshold value varies at every height and is defined as a fraction α of the maximum shear rate at the center of the shear band at a given height $\dot{\gamma}_{\max}(z)$. Thus, we consider the shear band region as all local points having shear rate $\dot{\gamma}(r, z) \geq \alpha \dot{\gamma}_{\max}(z)$. Thus, it is also evident that the span of the shear band region can be varied by varying α . The shear band is stable in an inhomogeneous system at a constant pressure and shear rate condition over regions with shear rate larger than the value $\alpha \dot{\gamma}_{\max}(z)$, $\alpha = 0.1$. The local shear rate $\dot{\gamma}$ is highest at the shear band center and drops as a Gaussian function of the distance from the center of the shear band at a given pressure [26, 43]. We vary the width (or distance from the center) of the shear band by varying $\alpha = 0.0$ to 0.8 and thereby see the effect on the liquid re-distribution. Figure 5.9(a) shows the liquid distribution of wet contacts for different

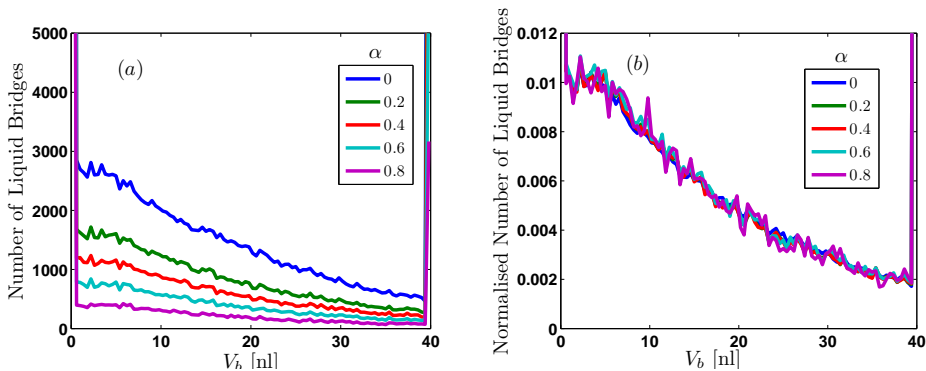


Figure 5.9: (a) Liquid bridge volume distribution and (b) normalized liquid bridge volume distribution for initial condition B for $\dot{\gamma}(r, z) \geq \alpha \dot{\gamma}_{\max}(z)$ and α varied from 0 to 0.8 after 6.03 s ($\gamma_g = 8.23$).

sections of the width of the shear band for α varying from 0.0 to 0.8. Here we do not show the distribution of the threshold liquid bridges. While we hardly observe a difference between the number of contacts between $\alpha = 0.2$ and 0.4, a significant difference is observed between $\alpha = 0.4$ and 0.8. Figure 5.9(b) shows the normalised liquid bridge distribution for different width of the shear band. Note that here we normalise the histogram for liquid bridge distribution by scaling with the total number of liquid bridges in the given histogram. The normalised distribution collapse for all width of the shear band, signifying that the liquid bridge distribution is symmetrical for any width of the shear band region. It is to be noted that here $\alpha = 0$ excludes the liquid bridge distribution near the boundaries.

5.4.4. DEPENDENCE ON THE LIQUID BRIDGE LIMIT-VOLUME

In this sub-section we discuss on the effect of increasing the liquid bridge limit-volume on the overall dynamics of liquid re-distribution. As a model simplification, we do not allow the formation of liquid clusters via bridge coalescence by using a limit V_{\max} of the bridge volumes which must not be exceeded. The liquid bridge limit-volume V_{\max} is varied in different simulations as explained in Section 5.2.3, Eq. 5.5. Figure 5.10(a) shows the mean liquid bridge volume $\langle V_b \rangle$ as a function of shear for different V_{\max} . Note that with increase in V_{\max} the maximum interaction distance between interacting particles i and j increases. Thus, the number of initial wet contacts increases with V_{\max} . The initial liquid bridge volume $V_b^0 \approx 11$ nl is same for all the simulations. The peak liquid bridge volume V_p and the intermediate liquid bridge volume V_i increases with increasing V_{\max} . Figure 5.10(b) shows that the number of wet contacts per particles decreases with increasing V_{\max} . Thus, allowing clustering of liquid leads to higher mean liquid bridge volume per contact and less number of wet contacts per particle in the intermediate pseudo-critical state. However, even though V_{\max} is very large for the extreme cases, $\langle V_b \rangle$ is well within the accuracy of the Willet model, i.e., very few number of liquid bridges are formed which are of large liquid bridge volume.

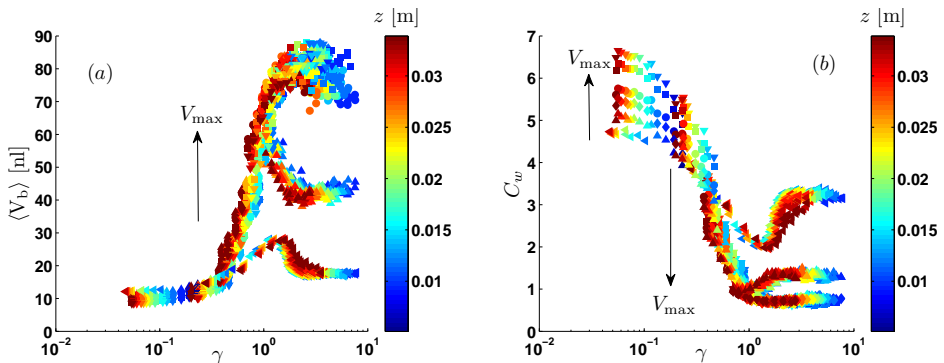


Figure 5.10: a) Mean liquid bridge volume per contact and b) fraction of wet contact as a function of shear for initial condition B for different different maximal liquid bridge volume quantified by β , $\triangleleft \beta = 0.03$, $\triangle \beta = 0.08$, $\diamond \beta = 0.15$, $\circ \beta = 0.23$, $\square \beta = 0.45$ and $\nabla \beta = 0.60$ for $\alpha = 0.4$ with initial condition B as initial condition.

5.4.5. DEPENDENCE ON THE LIQUID SATURATION

In this sub-section, we study the effect of liquid saturation on the liquid re-distribution process. The bulk saturation is varied by varying the initial liquid film volume on the particles as mentioned in Section 5.2.4, Eq. 5.7. Figure 5.11(a) shows the mean liquid bridge volume for initial condition B as a function of shear for different V_f^0 . It is evident that the mean liquid bridge volume $\langle V_b \rangle$ increases with increasing saturation, i.e., bridges hold larger volume of liquid with increasing saturation. All the other parameters like the peak liquid bridge volume V_p and the intermediate state liquid bridge volume V_i increases with saturation. Figure 5.11(b) shows the mean wet contacts per particle for initial condition B as a function of shear. The initial number of contacts per particle remain the same, which depends on the initial packing, irrespective of the saturation in the system. The number of wet contacts per particle increases with increasing saturation. Thus both the mean liquid bridge volume per contact and the number of contacts per particle increases with increasing saturation in the system.

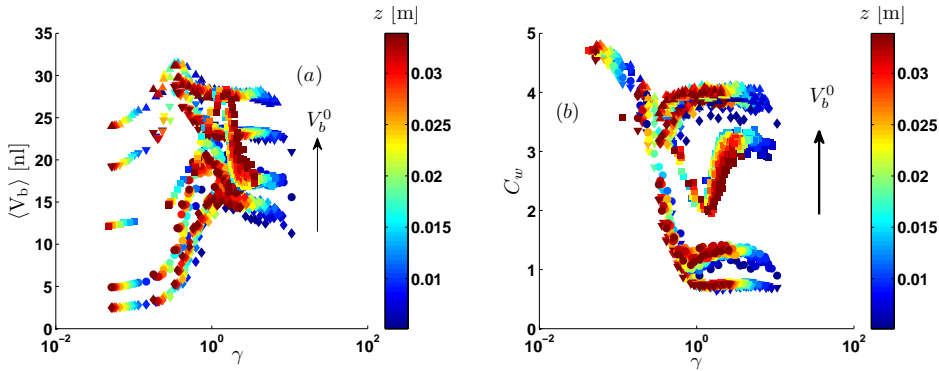


Figure 5.11: (a) Mean liquid bridge volume per contact (b) number of wet contacts per particle as a function of shear for different saturation $\nabla V_f^0 = 10$ nl, $\circ V_f^0 = 20$ nl, $\square V_f^0 = 50$ nl, $\diamond V_f^0 = 80$ nl and $\triangle V_f^0 = 100$ nl for $\alpha = 0.4$ with initial condition B as initial condition.

5.4.6. EFFECT OF DIFFUSION AND TRANSPORT OF LIQUID

There are two relevant processes that cause the spreading of liquid. It is known that in shear flows, particles undergo a self-diffusive motion and therefore, also liquid which is carried by the menisci will diffuse in space [44, 45]. It has been observed that the particle diffusivity is proportional to the local shear rate in quasi-static dense flows. Secondly, there is a transport of liquid associated to liquid bridge rupture. The overall liquid migration is a non-steady state diffusive process and occurs over a relatively larger scale of shear. The diffusive liquid transfer is triggered inside the shear band at the onset of shearing. However, of mass transport mechanisms, molecular diffusion is known as a slower one. Hence, at the initial, small shear strains, the liquid re-distribution dominates over the diffusive liquid transport process. This is shown in Figure 5.12(a) and (b).

Figure 5.12(a) shows the mean liquid bridge volume per wet contact inside the shear band as a function of shear for initial conditions A and B. Figure 5.12(b) shows the fraction of wet contacts as a function of shear inside the shear band for initial conditions A

and B. A dramatic change in the mean liquid bridge volume and the number of wet contacts is observed during the initial phase of shearing. This is evidently the phase of liquid re-distribution. The system reaches a pseudo-critical state followed by this when both the mean liquid bridge volume per contact and the number of wet contacts per particle reaches a temporary steady state. On further shear, the mean volume of liquid bridge per contact decreases slightly and the number of wet contacts per particle slowly decays. The overall liquid content decreases inside the shear band in the long term. This is evidently the regime when diffusive transfer of liquid is dominating. These mechanisms of liquid transfer are interesting, but beyond the scope of the present study, and thus will be discussed elsewhere (Chapter 6).

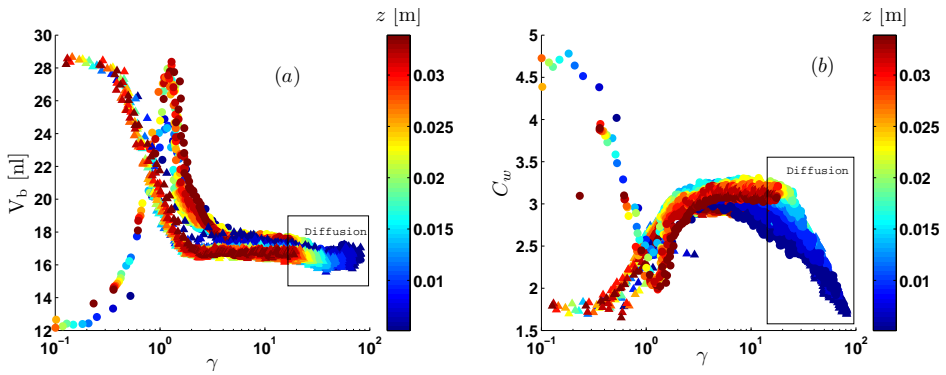


Figure 5.12: a) Mean liquid bridge volume per contact and b) wet contacts per particle as a function of strain for initial condition A (Δ) and initial condition B (\circ).

5.5. CONCLUSIONS

The transients of liquid transport and re-distribution are studied for different initial conditions of liquid distribution in the system. Governed by the rupture of existing, and the formation of new liquid bridges, the initial distribution of liquid in the system is modified to a pseudo steady- or critical-state within (local) shear strains of order of around 2 – 4, almost independent of the initial liquid distribution. While the random liquid re-distribution is dominating at small shear strains, shear driven diffusive liquid transport away from the shear band is dominating for larger shear strains above 10 – 20. Gradually the shear band becomes dry, devoid of wet contacts in this later regime, i.e., liquid is transported towards the already wet areas.

Besides the liquid-properties, the transients are also influenced by the bulk saturation in the system and the liquid bridge limit-volume imposed in our model. As expected, the mean liquid bridge volume per contact and the number of wet contacts per particle both increase with increasing saturation. The mean liquid bridge volume per contact increases, but the number of wet contacts per particle decreases with increasing limit-volume V_{\max} . Even when set to very large values for the extreme cases, the mean liquid bridge volume per contact ($\langle V_b \rangle$) is within the accuracy of the Willet model, well below the volume needed to fill the pores and the distribution is mostly unaffected by the limit-

parameter.

As future scope of our studies, we intend to focus more on the liquid transport theory in both small and large strain regimes (Chapter 6), as well as on experimental validation of the present numerical predictions (Chapter 7).

REFERENCES

- [1] M. Gonzalez and A. M. Cuitiño, *Journal of the Mechanics and Physics of Solids* **93**, 44 (2016).
- [2] T. Müllner, K. K. Unger, and U. Tallarek, *New Journal of Chemistry* **40**, 3993 (2016).
- [3] A. J. Liu and S. R. Nagel, *Nature* **396**, 21 (1998).
- [4] Y. Jin and H. A. Makse, *Physica A: Statistical Mechanics and its Applications* **389**, 5362 (2010).
- [5] D. Bi, J. Zhang, B. Chakraborty, and R. P. Behringer, *Nature* **480**, 355 (2011).
- [6] F. Göncü, O. Durán, and S. Luding, *Comptes Rendus Mécanique* **338**, 570 (2010).
- [7] V. Ogarko and S. Luding, *Soft Matter* **9**, 9530 (2013).
- [8] W. Lo, F. Yang, C. Chen, and S. Hsieh, *Granular Matter* **17**, 717 (2015).
- [9] K. Kamrin and G. Koval, *Computational Particle Mechanics* **1**, 169 (2014).
- [10] N. Guo and J. Zhao, *Computers and Geotechnics* **47**, 1 (2013).
- [11] T. Kurtay and A. Reece, *Journal of Terramechanics* **7**, 23 (1970).
- [12] A. Sawicki and W. Świdziński, *Archives of Hydro-Engineering and Environmental Mechanics* **54**, 207 (2007).
- [13] S. Roy, A. Singh, S. Luding, and T. Weinhart, *Computational particle mechanics* **3**, 449 (2016).
- [14] S. Luding and F. Alonso-Marroquín, *Granular Matter* **13**, 109 (2011).
- [15] A. Singh, V. Magnanimo, K. Saitoh, and S. Luding, *New Journal of Physics* **17**, 043028 (2015).
- [16] S. Roy, S. Luding, and T. Weinhart, *New Journal of Physics* **19**, 043014 (2017).
- [17] V. Richefeu, M. S. El Youssofi, and F. Radjai, *Physical Review E* **73**, 051304 (2006).
- [18] F. Radjai and V. Richefeu, *Philosophical transactions. Series A, Mathematical, physical, and engineering sciences* **367**, 5123 (2009).
- [19] S. Roy, S. Luding, and T. Weinhart, in *EPJ Web of Conferences* **140**, 03065 (2017).
- [20] R. Mani, D. Kadau, D. Or, and H. J. Herrmann, *Physical Review Letters* **109**, 248001 (2012).

- [21] R. Mani, C. Semperebon, D. Kadau, H. J. Herrmann, M. Brinkmann, and S. Herminghaus, *Physical Review E* **91**, 042204 (2015).
- [22] M. Scheel, R. Seemann, M. Brinkmann, M. Di Michiel, A. Sheppard, and S. Herminghaus, *Journal of Physics: Condensed Matter* **20**, 494236 (2008).
- [23] M. M. Kohonen, D. Geromichalos, M. Scheel, C. Schier, and S. Herminghaus, *Physica A: Statistical Mechanics and its Applications* **339**, 7 (2004).
- [24] S. Herminghaus, *Advances in Physics* **54**, 221 (2005).
- [25] F. Bianchi, M. Thielmann, R. Mani, D. Or, and H. J. Herrmann, *Granular Matter* **4**, 1 (2016).
- [26] J. A. Dijksman and M. van Hecke, *Soft Matter* **6**, 2901 (2010).
- [27] G. H. Wortel, J. A. Dijksman, and M. van Hecke, *Physical Review E* **89**, 012202 (2014).
- [28] A. Singh, V. Magnanimo, K. Saitoh, and S. Luding, *Physical Review E* **90**, 022202 (2014).
- [29] S. Luding, *Particulate Science and Technology* **26**, 33 (2007).
- [30] S. Luding, *Particuology* **6**, 501 (2008).
- [31] A. Gladky, *Granular Matter* **16**, 911 (2014).
- [32] S. Luding, *Particulate Science and Technology* **26**, 33 (2008).
- [33] R. Schwarze, A. Gladky, F. Uhlig, and S. Luding, *Granular matter* **15**, 455 (2013).
- [34] T. Weinhart, D. Tunuguntla, M. van Schroyen-Lantman, A. van der Horn, I. Denissen, C. Windows-Yule, A. de Jong, and A. Thornton, in *Proceedings of the 7th International Conference on Discrete Element Methods*, 1353–1360 (2017).
- [35] A. Thornton, D. Krijgsman, A. Voortwis, V. Ogarko, S. Luding, R. Fransen, S. Gonzalez, O. Bokhove, O. Imole, and T. Weinhart, 50–56 (2013).
- [36] C. D. Willett, M. J. Adams, S. A. Johnson, and J. Seville, *Langmuir* **16**, 9396 (2000).
- [37] B. Derjaguin, *Colloid and Polymer Science* **69**, 155 (1934).
- [38] G. Lian, C. Thornton, and M. J. Adams, *Journal of colloid and interface science* **161**, 138 (1993).
- [39] R. Mani, D. Kadau, and H. J. Herrmann, *Granular Matter* **15**, 447 (2013).
- [40] M. Scheel, R. Seemann, M. Brinkmann, M. Di Michiel, A. Sheppard, B. Breidenbach, and S. Herminghaus, *Nature materials* **7**, 189 (2008).
- [41] N. Mitarai and F. Nori, *Advances in Physics* **55**, 1–45 (2006).
- [42] A. Denoth, *Journal of Glaciology* **28**, 357 (1982).

- [43] A. Ries, D. E. Wolf, and T. Unger, *Physical Review E* **76**, 051301 (2007).
- [44] B. Utter and R. P. Behringer, *Physical Review E* **69**, 031308 (2004).
- [45] C. S. Campbell, *Journal of Fluid Mechanics* **348**, 85 (1997).
- [46] T. Weigert and S. Ripperger, *Particle & Particle Systems Characterization* **16**, 238 (1999).



6

DIFFUSIVE-CONVECTIVE LIQUID MIGRATION IN UNSATURATED SHEARED GRANULAR MEDIA

We study fluid migration in partly saturated shear bands where liquid is transported away from the shear band center. Given a continuum model for liquid migration in sheared granular media, we apply this model to a two dimensional (2D) Cartesian shear cell with one wide shear band and compare the solution with Discrete Element Method (DEM) simulations. Initially, a high liquid density is observed at the edges of the shear band where the second gradient of the shear rate profile is largest and positive. The high liquid density front propagates towards the shear cell boundaries, demarcating the sheared and liquid depleted zone from the unchanged non-sheared zone near the boundaries. We predict the trajectory of the liquid density peak from the continuum model and compare with our DEM simulations with good quantitative agreement and draw our conclusions.

In some detail, earlier studies show that the liquid migration can be modeled by a diffusive equation with a space-dependent diffusive coefficient in the split bottom shear cell. Simplifying to one dimensional diffusion and transforming this equation to an appropriate set of variables, we show that liquid migration is a drift-diffusion process with constant diffusivity coefficient and space dependent drift coefficient. In this way, we can obtain an analytical solution for the liquid density as a function of space and time, neglecting the diffusion term of the transformed equation. This analytical approximation gives a good qualitative agreement with the full continuum model, though not quantitative, signifying that the diffusion has a significant role in liquid transport. Further, we show that the contributions from drift (analytical) and diffusion (semi-analytical and numerical) on the

Roy, S., den Otter, W. K., Thornton, A. R., Luding, S., Tunuguntla, D. R. and Weinhart, T., Diffusive-convective liquid migration in unsaturated sheared granular media, to be submitted.

overall transport of liquid are additive for short time increments. Although, we did simplifications and transformation of the principal diffusion equation, which leads to some quantitative deviation of the liquid density profile, we show that the location of liquid density peak is determined by both terms of the transformed equation.

6.1. INTRODUCTION

Liquid saturation is of tremendous importance to the stability properties of soil structures. Granular materials generally gain strength with increasing liquid content [1–3]. On the other hand, liquid accumulation in soil pores may cause a dramatic decrease in strength leading, e.g., to landslides or soil collapses [4]. Thus, liquid migration within soil pores plays an important role for the overall properties of soil. Liquid migration is also of great interest in a variety of other applications like pharmaceutical industries, powder technology or in wet granulation process where grains are mixed with liquid and initial surface wetting is carried out by inducing liquid migration by shearing actions of e.g. the blades inside a rotating device. Thus, understanding the liquid transport phenomena in sheared wet granular media is of great importance for the granular community.

Pore liquids reconfigure in different ways depending on the saturation level of the granular materials. Liquid is sucked into dilating shear bands [5, 6] with increasing porosity in fully saturated granular materials. In contrast, liquid transport at low liquid contents is induced by firstly, (self)-diffusive motion of particles and liquid films and secondly, rupture and reconfiguration of individual liquid bridges on the local, microscale. The focus of our discussion here is the migration of liquid in unsaturated, i.e. partly saturated granular media. Reconfiguration of liquid bridges in the shear band, induced by the shear rate, leads to liquid bridge re-distribution and liquid transport (where liquid is driven out of the shear band). While the liquid re-distribution phenomenon is limited to small shear scale, i.e. happens at the beginning of shearing, liquid transport is rather a slow diffusive process driven by the local shear rate and is the subject matter of this paper.

Liquid migration or transport from the shear band can be understood as a shear rate driven diffusion phenomenon with the diffusivity coefficient proportional to the shear rate [7, 8]. The liquid density profile shows remarkable features, particularly in a split bottom shear cell, where the shear rate profile is an error-function of space [9, 10] and its width increases with the height in the system [10]. More precisely, in this set-up, liquid migrates from the zone of high shear rate to the relatively slowly sheared or non-sheared zones. While the shear band gets depleted, a high liquid density peak is initially observed at the edges of the shear band where the second gradient of the shear rate is positive and is the largest [7]. However, whether this liquid density peak is stationary over time or behave differently is still an open question.

There are different relevant processes involved in the spreading of liquid. It is known that in shear flows, particles undergo a self-diffusive motion and therefore, also liquid which is carried by the menisci will diffuse in space [11, 12]. It is observed that the particle diffusivity is proportional to the local shear rate in quasi-static dense flows. Secondly, there is a transport of liquid associated to liquid bridge rupture, the flux induced by bridge rupture being large compared to that by bridge formation. Both self-diffusion of particles and liquid bridge rupture processes are however, functions of the shear rate.

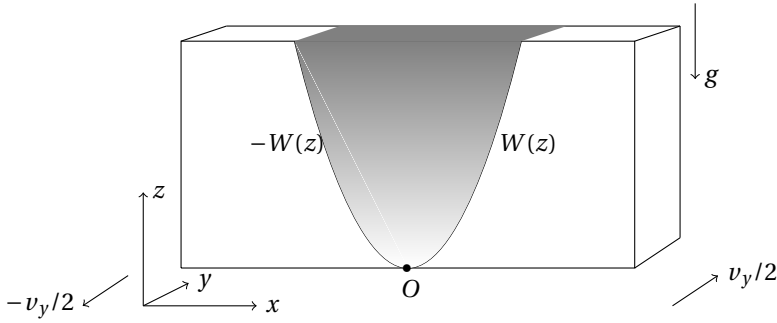


Figure 6.1: Schematic diagram of simulation set-up.

Thirdly, the equilibrium distribution of bridge volumes plays a fundamental role in liquid transport [13], the liquid transport flux between two capillary bridges on the same grain being proportional to the difference in their capillary pressure. However, we neglect the latter mode of liquid transport in our present study. Thus, liquid migration is a non-steady diffusive process with a shear rate dependent diffusive coefficient. In this case, the diffusion equation becomes a nonlinear partial differential equation, and the analytical/ mathematical solution is almost impossible, even in the case of only time and one dimension space coordinates. Thus, we make an approach towards a suitable transformation of the coordinates to find analytical or semi-analytical solutions. Thereby, we obtain a PDE in drift-diffusion form and analyse the role of drift and diffusion on the overall liquid transport process. In this paper, we investigate the dynamics of the liquid front trajectory in the initial part of our studies. We compare the results from the continuum model and compare with the DEM simulations for the liquid front trajectory.

6.2. SYSTEM AND NUMERICAL SCHEMES

6.2.1. GEOMETRY

We simulate a simple linear split bottom shear cell which consists of two straight ‘L’ shapes sliding past each other shown in Figure 6.1. We use Cartesian coordinates where the x direction is perpendicular and the y direction is parallel to the slit, with periodic boundaries, and the z direction is perpendicular to the bottom plates [10, 14, 15]. The left and the right sides of the boundary move along the y axis in opposite directions with speed $-v_y/2$ and $v_y/2$ and particles filled in between the ‘L’ shapes. When there is a relative motion at the split, a shear band propagates from the split position O upwards. The width of the shear band W increases as a power law function of the height z inside the shear cell [10] as shown in the schematic figure.

6.2.2. DISCRETE ELEMENT MODEL

The approach towards the microscopic understanding of macroscopic particulate material behavior is the modeling of particles using so-called Discrete Element Methods (DEM). Contact models are at the physical basis of DEM simulations. We perform DEM simulations using open source code MercuryDPM. Small grains are glued to the side

Table 6.1: Dimensions of simulation.

Parameters	Dimensions	Parameters	Dimensions
Gravity (g)	10 ms^{-2}	Particle diameter (d_p)	2.2 mm
Length	$8d_p$	Particle density (ρ_p)	2000 kgm^{-3}
Width	$30d_p$	Contact angle (θ)	20°
Height	$8d_p$	Particle stiffness (k)	$2367 \frac{\pi \rho_p d_p^2 g}{6}$
Shear Velocity (v_y)	$0.036 \sqrt{d_p g}$	Surface tension (σ)	$0.20 \frac{\pi \rho_p d_p^2 g}{6}$
Number of particles (N)	8220	Dissipation (γ_o)	$0.66 \frac{\pi \rho_p d_p^3 \sqrt{g}}{6 \sqrt{d_p}}$
		Limit Bridge Volume (V_b^{\max})	$0.006 d_p^3$

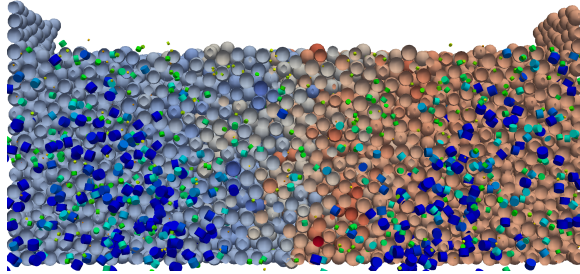


Figure 6.2: A snapshot from the DEM simulation showing liquid migration from the shear band in a Cartesian shear cell geometry. The colors of the particles indicate their increasing velocity $v_y/2$ from negative to positive (blue to red). The colors and sizes of the liquid bridges indicate their increasing liquid volume (red to blue).

walls and bottom to make the surface rough and periodic boundary conditions is applied in the y direction. All the dimensions of the shear cell geometry, particles and the contact model parameters for our DEM simulations are given in Table 6.1. The details of the contact model is given in [3] and we describe the mechanism of liquid bridge formation and rupture in details as given in Chapter 5.

Figure 6.2 shows a snapshot from the DEM simulation showing the liquid migration from the shear band in a Cartesian shear cell geometry. The particles are colored according to the magnitude and direction of their velocity from red (positive) to blue (negative). The liquid bridges are shown in the form of cylinders with their diameter signifying the liquid bridge volume at the contact. Note that the colors are adjusted to a suitable range to have a better visualisation. It is evident from the figure that the liquid bridge concentration is lowest inside the shear band, highest near the edges of the shear band and an intermediate concentration near the walls of the shear cell.

6.2.3. CONTINUUM MODEL

Numerical methods suitable for the solution of the transport equations are a matter of extensive research in computational fluid dynamics. Its application is predominant in

various research fields like geophysical fluid dynamics [16], hydrological processes [17], reactor flow [18] etc. In the Eulerian solution of equations, difficulties arise because of the dual nature of the transport equation. When the transport is advection or drift dominated, the equation behaves as a first-order hyperbolic equation, but when the transport is diffusion dominated the equation behaves as a second-order parabolic equation. To accurately model the drift-diffusion transport, the numerical scheme must be able to handle the mixed parabolic-hyperbolic character of the systems. Eulerian models that have grids fixed in space have a number of difficulties when transport is drift dominated. These include numerical diffusion, oscillations, instabilities and peak clipping because of the numerical representation of advection terms in the transport equation.

The unsteady diffusive equation for liquid transport is given as:

$$\dot{Q} = D_{\text{liq}} \nabla^2 (\dot{\gamma} Q) \quad (6.1)$$

where, Q is the specific volume of liquid (also referred to as liquid density), D_{liq} is the constant part of diffusivity coefficient of liquid depending on the liquid flow properties, global shear rate and $\dot{\gamma}$ is the local shear rate. Note that the local shear rate is a Gaussian function of space and is given by $\dot{\gamma} = v_y / (W \sqrt{\pi}) \exp[-(x/W)^2]$, $v_y = v_y(z)$ is the shear velocity and the width of the shear band $W = W(z)$ is predicted from [10]. The overall diffusivity coefficient $D = D_{\text{liq}} \dot{\gamma}$ is dependent on the local shear rate. The above equation appears to be a diffusive equation, though in the later sections we discuss about the transformation of this equation to a drift-diffusive form in another frame of reference.

To avoid instabilities, Eq. 6.1 is solved over the domain using a backward Euler method (or implicit Euler method) in time and a central difference method in space, by using Neumann boundary conditions and with the same initial condition and shear rate as in the DEM simulation. The total liquid volume is conserved over time with a relative error of less than 10^{-13} . The system being symmetrical to $x = 0$, in the following sections, we show our results for half of the system.

6.3. COMPARISON OF DEM AND CONTINUUM MODEL

We use a coarse graining post-processing tool MercuryCG to translate DEM data from discrete to continuum level. Discrete data of liquid film volumes and liquid bridge volumes related to particles and their contacts respectively are converted to continuous fields of specific liquid volume. Since the liquid density profile is dynamic in nature, we obtain the temporal averaging over a very short period of time of 0.28 s. We obtain the local fields mean liquid bridge volume $\langle V_b \rangle$ and mean liquid film volume $\langle V_f \rangle$ respectively as functions of positions x and z . Followed by this, we obtain the local liquid density Q , which is the focus of our interest in the continuum scale.

6.3.1. LIQUID DENSITY

Figure 6.3(a) shows a comparison of the liquid density field obtained from the DEM simulation with the continuum model for the middle height (blue data) and close to the surface (green) of the shear cell. Keeping all the parameters of the continuum model exactly same as the DEM model, we have tuned the parameter $D_{\text{liq}} = 2 \times 10^{-5} \text{ m}^2$ in order to match the specific liquid volume with the DEM model. Thus, the continuum model is in

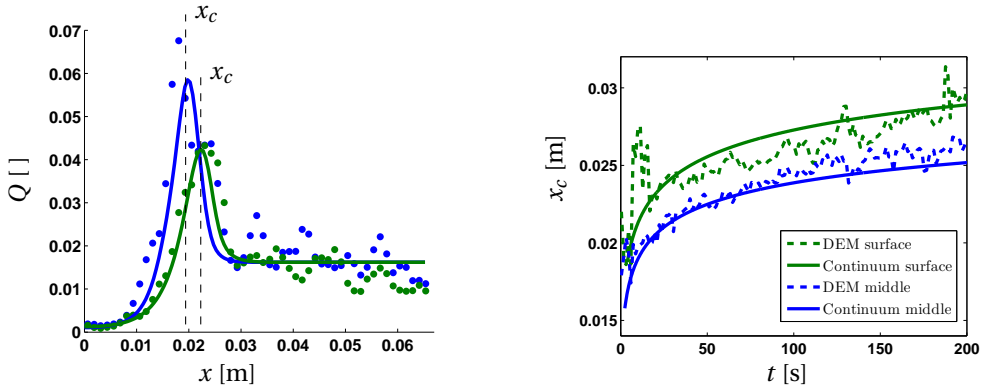


Figure 6.3: Comparison of (a) liquid density as a function of x after 40 s, the dashed lines are given by Eq. 6.2. and (b) liquid front trajectory from the DEM and continuum models at middle height (blue, $z = 8$ mm) and surface (green, $z = 12$ mm) predicted by Eq. 6.2.

good agreement with the DEM model for predicting the liquid volume density. The shear rate profile in a split bottom shear cell is a Gaussian function of the axial positions x and the width increases with height z . The shear rate being highest at the shear band center and the second derivative of shear rate $\partial^2 \dot{\gamma} / \partial x^2$ being smallest and negative, the liquid content decreases in the shear band. $\partial^2 \dot{\gamma} / \partial x^2$ being largest and positive at the edges of the shear band, this causes an accumulation of liquid along the edges at the beginning of shear. The locations near the boundary of the shear cell are barely affected by finite shear and thus the liquid density remains unchanged as the initial liquid density Q_0 . Thus, a liquid density peak is observed initially at the edges of the shear band that separates the sheared depleted zone from the relatively saturated non-sheared zone of liquid near the walls of the shear cell.

6.3.2. TRAJECTORY OF LIQUID MIGRATION

In the earlier sub-section we have discussed that when the shear band gets depleted of liquid, an accumulation of liquid happens near the edges of the shear band. We have compared the results of our DEM simulation with the continuum model. We observe that this liquid density peak propagates towards the wall with time. Thus, we get a location of the peak liquid density x_c , which moves towards the wall with time.

Defining the location of peak liquid density as the location of the maximum liquid density has the following disadvantages: firstly, as the grid resolution is finite (130 points in x -direction), the peak of the liquid density can only be located with an accuracy of 0.05 cm, resulting in an undesirable stepwise definition. Secondly, the noise in the coarse grained data from the DEM model, especially at small times, can create local maxima of the liquid density, thus creating an error in finding the peak location. To avoid these effects, the location of the peak liquid density is defined as the centroid of the liquid density profile which is lying above the initial liquid density Q_0 . Thus the definition of

x_c is given as:

$$x_c = \frac{\int_0^{W/2} x \tilde{Q} dx}{\int_0^{W/2} \tilde{Q} dx} \quad \text{where } \tilde{Q} = \max(Q - Q_0, 0). \quad (6.2)$$

The location of the peak liquid density is well approximated by this definition for both the continuum and the DEM models. We compare the trajectory of x_c from our DEM simulations with the continuum model as shown in Figure 6.3(b) over a time period of 200 s. The data shows good agreement between the discrete and the continuum model, both at the middle height (blue color) and near the surface (green color), thus verifying the continuum description of liquid migration.

6.4. EFFECT OF DIFFUSION IN VERTICAL DIRECTION

The important purpose of this section is to lead towards finding an analytical solution for the Eq. 6.1 to get the liquid volume density Q as a function of space and time. However, we need to simplify the equation to its one-dimensional form as a first step towards the analytical solution, neglecting the z diffusion component. Thus, the non-steady state diffusion Eq. 6.1 is simplified as:

$$\frac{\partial Q_x}{\partial t} = D_{\text{liq}} \frac{\partial^2 (\dot{\gamma} Q_x)}{\partial x^2} \quad (6.3)$$

We solve Eq. 6.3 using the same numerical scheme as mentioned in Sec. 6.2.3. We compare here the location of the front x_c and the peak liquid density for the two Eqs. 6.1 and 6.3 by solving them numerically. Both Eqs. 6.1 and 6.3 are solved numerically and the results of the location of the peak liquid density, x_c and the peak liquid density, Q_{max} are plotted as a function of time t as shown in Figure 6.4(a) and (b) respectively at the middle height (blue) and near the surface (green). The solutions of Eqs. 6.1 and 6.3 are represented by the solid and dotted lines respectively. Note that, while x_c is unaffected, Q_{max} is significantly affected by the diffusion in z direction, especially closer to the base of the shear cell, where the shear gradient is stronger. This is also evident from Figure 6.5(a) and (b) showing the contour plot of liquid volume as a function of space x and z solved for Eqs. 6.1 and 6.3 respectively after $t = 40$ s. Thus, an approach towards a simplified analytical solution of the liquid density profile is likely to deviate quantitatively from our observations in the first place. Starting to shear from an uniform distribution of liquid, the location of x_c at the first time step is obtained analytically as $x_c^0 = x_c(t = 0) = \sqrt{1.5}W(z)$, given by the location where $\partial^2 \dot{\gamma} / \partial x^2$ is maximum.

6.5. TRANSFORMATION TO DRIFT AND DIFFUSION EQUATION

In this section, we propose methods for solving Eq. 6.3 analytically to determine the liquid volume density as a function of time and space at an intermediate height. At each height z , the variable diffusion coefficient is $D(x) = D_{\text{liq}} \dot{\gamma}(x)$. We discuss methods for solving this one-variable diffusion equation with horizontally (only) space dependent diffusion coefficient $D(x) > 0$. In order to solve this analytically, one needs to have a suitable transformation of frame of reference using the field $\xi = \xi(x)$ so that the x -dependent diffusion coefficient can be transformed to an arbitrary diffusion *constant* $D_c > 0$. For

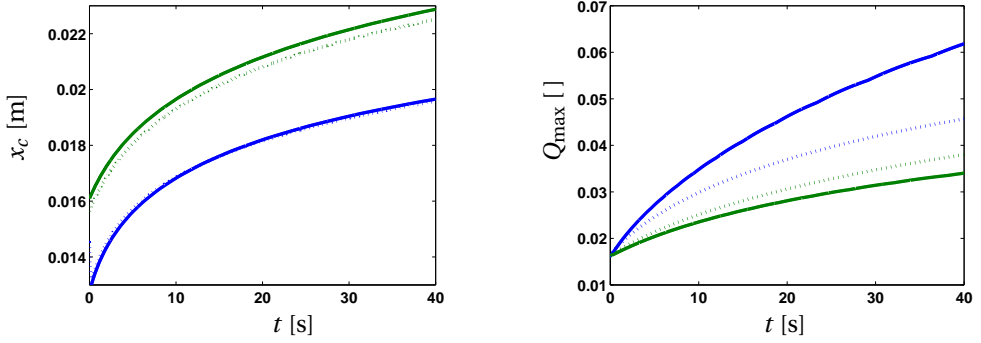


Figure 6.4: (a) Location of the liquid front x_c (from Eq. 6.2) and (b) peak liquid density Q_{\max} as a function of time t as obtained from Eq. 6.1 (solid lines) and Eq.6.3 (dotted lines) respectively for the middle height (blue, $z = 8$ mm) and surface (green, $z = 12$ mm).

6

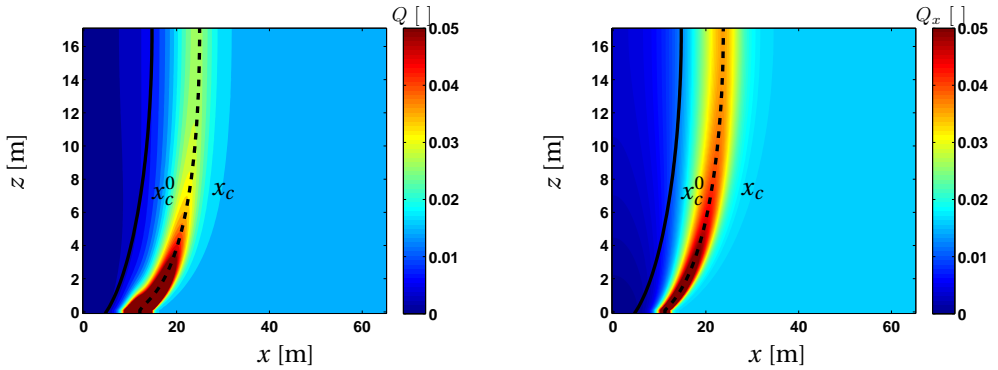


Figure 6.5: Contour plot of liquid volume density in cartesian shear cell after 40 s for (a) Eq. 6.1 and (b) Eq. 6.3. The solid line is given by the analytical prediction of the location of liquid density peak x_c^0 at $t = 0$. The dashed line denotes the location of maxima liquid density for different heights as obtained from Eq. 6.2.

the one variable case, this transformation reads:

$$D_c = \left(\frac{d\xi}{dx} \right)^2 D(x) \quad (6.4)$$

We obtain $d\xi/dx = \frac{1}{\sqrt{D_{\text{liq}}\dot{\gamma}(x)}}$ and $d^2\xi/dx^2 = \frac{x}{W^2} \frac{1}{\sqrt{D_{\text{liq}}\dot{\gamma}(x)}}$ from the above equations. The transformed Eq. 6.3 now reads :

$$\frac{\partial Q'_x(\xi, t)}{\partial t} = - \underbrace{\frac{\partial(D'(\xi)Q'_x(\xi, t))}{\partial \xi}}_{\text{Drift}} + D_c \underbrace{\frac{\partial^2 Q'_x(\xi, t)}{\partial \xi^2}}_{\text{Diffusion}}, \quad (6.5)$$

where, $Q'_x = Q_x \sqrt{D(x)/D_c} = Q_x \sqrt{D_{\text{liq}}\dot{\gamma}(x)}$. Now, the equation transformed using a suitable coordinate $\xi = \xi(x)$ with a constant diffusion coefficient $D_c = 1$ has a space dependent drift coefficient $D'(\xi) = \frac{d^2\xi}{dx^2} D(x) = \frac{x}{W^2} \sqrt{D_{\text{liq}}\dot{\gamma}(x)}$. Drift and diffusion processes can now be considered independently and their effects are explored in the following sections.

6.5.1. DRIFT

The overall transfer mechanism of liquid can be described as a convection process which is governed by the combined effect of drift and diffusive mass transfer processes. We solve the equation analytically, neglecting the effect of diffusion and consecutively do a comparison with the effect of drift and diffusion sources of liquid transfer. We start with a simplistic approach, neglecting the diffusive term of the transformed Eq. 6.5 which can be re-written as:

$$\frac{\partial Q'_{x, \text{Drift}}(\xi, t)}{\partial t} + \frac{\partial \left(\frac{x}{W^2} \sqrt{D_{\text{liq}}\dot{\gamma}(x)} Q'_{x, \text{Drift}}(\xi, t) \right)}{\partial \xi} = 0. \quad (6.6)$$

The above equation is transformed to eliminate ξ and is given as:

$$\frac{\partial Q'_{x, \text{Drift}}(x, t)}{\partial t} + \left(\frac{\partial \xi}{\partial x} \right)^{-1} \frac{\partial \left(\frac{x}{W^2} \sqrt{D_{\text{liq}}\dot{\gamma}(x)} Q'_{x, \text{Drift}}(x, t) \right)}{\partial x} = 0. \quad (6.7)$$

Re-transforming the above equation to a simpler form with $R(x, t) = \frac{x}{W^2} \sqrt{D_{\text{liq}}\dot{\gamma}(x)} Q'_{x, \text{Drift}}(x, t)$ yields:

$$\frac{\partial R(x, t)}{\partial t} + \frac{x}{W^2} D_{\text{liq}}\dot{\gamma}(x) \frac{\partial R(x, t)}{\partial x} = 0. \quad (6.8)$$

The general solution is deduced as $R(x, t) = f\left(-t + \frac{W^3 Ei(x^2/W^2)}{2C}\right)$ using Mathematica. With an initial condition at $x_o(t=0)$, the general solution is:

$$x_o = \sqrt{W^2 Ei^{-1}\left(-\frac{2Ct}{W^3} + Ei\left(\frac{x^2}{W^2}\right)\right)} \quad (6.9)$$

and

$$R(x, t) = R_o \left(\sqrt{W^2 Ei^{-1}\left(-\frac{2Ct}{W^3} + Ei\left(\frac{x^2}{W^2}\right)\right)} \right) \quad (6.10)$$

The initial condition is given as:

$$R_o(t=0) = Q_o \frac{x}{W^2} D_{\text{liq}} \dot{\gamma}(x). \quad (6.11)$$

This has to satisfy the initial condition for $Q_{x, \text{Drift}} = Q_o(t=0)$, where $R = Q_{x, \text{Drift}} \frac{x}{W^2} D_{\text{liq}} \dot{\gamma}(x)$. Therefore,

$$R(x, t) = \frac{C}{W^3} \sqrt{W^2 Ei^{-1}\left(-\frac{2Ct}{W^3} + Ei\left(\frac{x^2}{W^2}\right)\right) \exp\left[-Ei^{-1}\left(-\frac{2Ct}{W^3} + Ei\left(\frac{x^2}{W^2}\right)\right)\right]} \quad (6.12)$$

and the liquid volume density

$$Q_{x, \text{Drift}}(x, t) = Q_o \frac{\sqrt{W^2 Ei^{-1}\left(-\frac{2Ct}{W^3} + Ei\left(\frac{x^2}{W^2}\right)\right) \exp\left[-Ei^{-1}\left(-\frac{2Ct}{W^3} + Ei\left(\frac{x^2}{W^2}\right)\right)\right]}}{x \exp[-(x/W)^2]} \quad (6.13)$$

This analytical solution is tested with the numerical solution of Eq. 6.8 in order to verify that the employed numerical method captures the analytical solution with sufficient accuracy.

6.5.2. DIFFUSION

In this section, we study the effect of diffusion on the overall liquid transfer process. Neglecting the drift term of Eq. 6.5 yields:

$$\frac{\partial Q'_{x, \text{Diff}}(\xi, t)}{\partial t} - \frac{\partial^2 Q'_{x, \text{Diff}}(\xi, t)}{\partial \xi^2} = 0. \quad (6.14)$$

The above equation is transformed back to x -coordinate and solved numerically by the method described in Sec. 6.2.3.

6.5.3. SIGNIFICANCE OF DRIFT AND DIFFUSION

In this section, we explore the significance of drift and diffusion processes separately on the overall liquid transport process. While both contributions change over time (not shown in the figure), they behave qualitatively the same, i.e. having a minimum at the center $x = 0$, a maximum of liquid density at the edges of the shear band and a constant liquid density near the boundary region. We explore here the trajectory of the high density liquid peak as a function of time for the drift and diffusion process as obtained from Eq. 6.8 and 6.14 respectively. We compare the trajectory given by drift and diffusion with the overall liquid transport trajectory given by Eq. 6.3 in order to interpret which mechanism dominates the liquid transport. Figure 6.6 (a) and (b) show the relative error of the trajectory of maximum liquid density as obtained from drift and diffusion with respect to the solution given by Eq. 6.3 for different heights $z = 8$ mm (blue solid lines) and $z = 12$ mm (green dashed lines). While the drift process shows a significant rise in the error upto 15%, the diffusion process error initially decreases to a minimum and then is saturated to a value of 6% in time scale of 10^3 s. Thus, we conclude that the trajectory of the liquid density peak in the liquid migration process is diffusion dominated on the long term. Note that these preliminary results show x_c is unpredictable in the initial time period and thus the plots in the Figure 6.6 (a) and (b) does not include time $t = 0$.

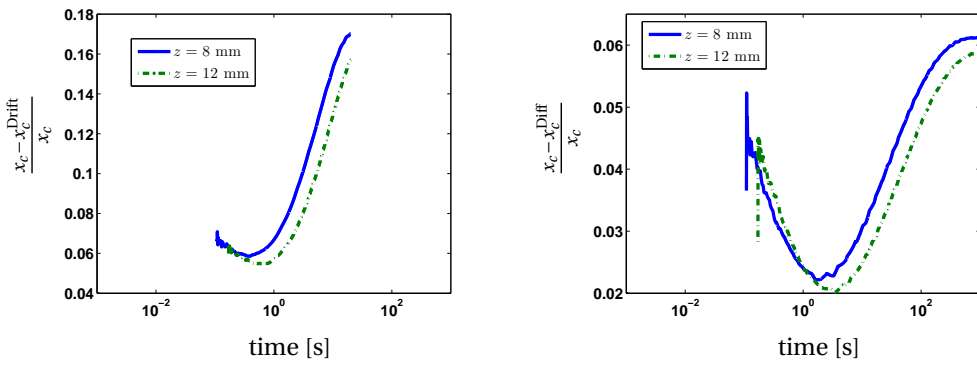


Figure 6.6: Error for the measurement of maximum liquid density peak as obtained from (a) Eq. 6.8 and (b) Eq. 6.14 for different heights $z = 8$ mm (blue solid lines) and $z = 12$ mm (green dashed lines).

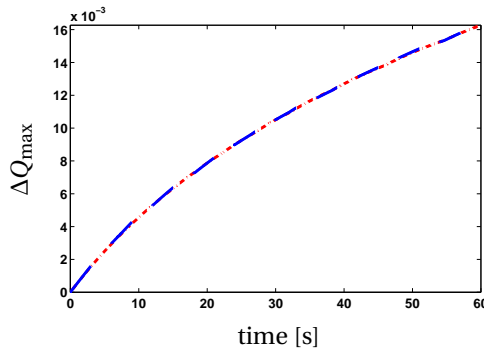


Figure 6.7: Net contribution to the incremental peak liquid density from drift $\Delta Q_{\max, \text{Drift}}$ (Eq. 6.8) and from diffusion $\Delta Q_{\max, \text{Diff}}$ (Eq.6.14), as compared with the overall contribution $\Delta Q_{\max, x}$ (Eq. 6.3) at the middle height ($z \approx 10$ mm).

6.5.4. SUPERPOSITION OF DRIFT AND DIFFUSION EFFECTS

The PDE for the transport of liquid from the shear band is composed of two components in a transformed coordinate, namely, diffusion and drift. While the drift is the flow of liquid due to bulk motion under the influence of shear, diffusion leads to the spreading of liquid from a higher to lower concentrations also under the influence of shear. It is to be noted from Eq. 6.5 that while diffusion leads to an increment in the local liquid volume, the drift acts reversely. However, both fluxes are additive. It is obvious that if the two fluxes are separately integrated over time, the resulting liquid density should also be additive, at least at a small time, when other effects, such as coupling, are negligible.

In this section, we analyse the incremental peak liquid density $\Delta Q_{\max} = Q_{\max} - Q_0$ from the two fluxes separately. The objective is to see if the resultant liquid density from the drift and diffusive fluxes by integrating Eq. 6.8 and 6.14 respectively, together contribute to the same incremental flux as obtained by integrating Eq. 6.3.

Figure 6.7 shows the comparison of the sum of the contribution from drift ($\Delta Q_{\max, \text{Drift}}$

from Eq. 6.8) and diffusion ($\Delta Q_{\max, \text{Diff}}$ from 6.14), given by the blue solid lines, with that of the overall contribution ΔQ_{\max} from Eq. 6.3 to the peak liquid density given by the red dash-dotted lines, at $z \approx 10$ mm. We observe that the contribution from drift and diffusion to the peak liquid density matches initially with the overall contribution, signifying that the two effects are additive in the initial phase. However, with further progress in time, the net contribution from the two effects over-predicts the liquid density.

6.6. CONCLUSION

The liquid content decreases within partially saturated shear bands, as observed from experiments, DEM and continuum numerical simulation results. A simple model for liquid transport explains this phenomenon as diffusion driven with a variable diffusivity dependent on the strain-rate. Being diffusion driven, the liquid re-distribution process is slow and hardly reaches a stationary state. Further, a high liquid density front located initially at the tails of the shear band, propagates away from the shear band towards the boundary, making the fluid depleted region wider and decreasingly saturated with time. We track the trajectory of the liquid front from DEM and continuum theory and show that the two numerical solutions are in good agreement.

Further, we show that the diffusive liquid migration model, defines the liquid migration phenomenon as a combination of drift and diffusive transport of liquid in a transformed coordinates frame where the new space variables' derivative is inversely proportional to the local square root of the shear-rate. The process can alternatively be understood as driven by constant diffusivity and a space dependent drift. An analytical expression is obtained for the liquid migration as a function of space and time for drift driven liquid migration, neglecting the effect of diffusion. It is observed that both drift and diffusion are significant for the overall liquid transport where diffusion wins on the long term. However, we get the same qualitative profile of liquid density over space from one or the other mode of liquid transport.

REFERENCES

- [1] S. Herminghaus, *Advances in Physics* **54**, 221 (2005).
- [2] F. Radjai and V. Richefeu, *Philosophical Transactions of the Royal Society of London A: Mathematical, Physical and Engineering Sciences* **367**, 5123 (2009).
- [3] S. Roy, A. Singh, S. Luding, and T. Weinhart, *Computational Particle Mechanics* **3**, 449 (2016).
- [4] S. Strauch and S. Herminghaus, *Soft Matter* **8**, 8271 (2012).
- [5] P. Hicher, H. Wahyudi, and D. Tessier, *Computers and Geotechnics* **16**, 205 (1994).
- [6] H.-J. Tillemans and H. J. Herrmann, *Physica A: Statistical Mechanics and its Applications* **217**, 261 (1995).
- [7] R. Mani, D. Kadau, D. Or, and H. J. Herrmann, *Physical Review Letters* **109**, 248001 (2012).

- [8] R. Mani, D. Kadau, and H. J. Herrmann, *Granular Matter* **15**, 447 (2013).
- [9] J. A. Dijksman and M. van Hecke, *Soft Matter* **6**, 2901 (2010).
- [10] A. Ries, D. E. Wolf, and T. Unger, *Physical Review E* **76**, 051301 (2007).
- [11] B. Utter and R. P. Behringer, *Physical Review E* **69**, 031308 (2004).
- [12] C. S. Campbell, *Journal of Fluid Mechanics* **348**, 85 (1997).
- [13] R. Mani, C. Semprebon, D. Kadau, H. J. Herrmann, M. Brinkmann, and S. Herminghaus, *Physical Review E* **91**, 042204 (2015).
- [14] M. Depken, W. van Saarloos, and M. van Hecke, *Physical Review E* **73**, 031302 (2006).
- [15] M. Depken, J. B. Lechman, M. van Hecke, W. van Saarloos, and G. S. Grest, *Europhysics Letters* **78**, 58001 (2007).
- [16] D. R. Durran and S. Mobbs, *Quarterly Journal of the Royal Meteorological Society* **127**, 273 (2001).
- [17] M. U. Igboekwe and N. Achi, *Journal of Water Resource and Protection* **3**, 192 (2011).
- [18] M. A. Hastaoglu and I. A. Abba, *Chemical Engineering & Technology* **19**, 337 (1996).
- [19] C. D. Willett, M. J. Adams, S. A. Johnson, and J. P. Seville, *Langmuir* **16**, 9396 (2000).
- [20] S. Roy, S. Luding, and T. Weinhart, *New Journal of Physics* **19**, 043014 (2017).
- [21] S. Roy, S. Luding, and T. Weinhart, *EPJ Web of Conferences* **140**, 03065 (2017).
- [22] M. Scheel, R. Seemann, M. Brinkmann, M. Di Michiel, A. Sheppard, B. Breidenbach, and S. Herminghaus, *Nature Materials* **7**, 189 (2008).



7

SURFACE FLOW PROFILES FOR DRY AND WET GRANULAR MATERIALS

Two-dimensional Particle Tracking Velocimetry (PTV) is a promising technique to study the behavior of granular flows. The aim is to experimentally determine the width and the position of the shear band in a split-bottom ring shear cell from the surface velocity profile and validate the simulations by experiments. The discrete particle velocities are tracked by analyzing images of scattered flow tracer particles as they move with the bulk flow. We extract the continuum velocity field by applying a coarse-graining technique using the MercuryCG postprocessing tool on the discrete experimental PTV data. For an intermediate filling height, the surface velocity field is extremely well fitted by an error function of the radial coordinate. From the error function fit, we get the surface width and the location of the center of the shear band. We investigate the dependence of the shear band properties on different filling heights and different rotation frequencies of the shear cell for dry glass beads. We study the effect of cohesion on the shear band by mixing different interstitial liquids, glycerol and silicon oil, with the glass beads.

7.1. INTRODUCTION

Dense granular materials display a rich and complex flow properties, which differentiate them from ordinary fluids. Despite their ubiquity, experimental studies of granular flows are difficult to perform due to their opaque nature. Nevertheless, insight has been generated through use of magnetic resonance imaging [1, 2], digital imaging [3–5], particle image velocimetry (PIV) applied to quasi-2D granular flows [6–8] and particle tracking velocimetry (PTV) [9–12]. Gollin et al. [13] did a comparative study on PIV and PTV for granular flow measurements.

Until recently, it was mostly reported that all granular shear bands were narrow i.e.

Roy, S., Polman, H., Scheper, B. J., Thornton, A. R., Tunuguntla, D. R., Luding, S. and Weinhart, T., Surface flow profiles for dry and wet granular materials, to be submitted, working towards including the torque measurements.

a few particle diameters [14–16]. However, in 2003 Fenistein et al. [17] discovered that in a modified Couette cell, granular shear bands can be arbitrarily broad. In this geometry, particles are filled in upto height H , confined under gravity, in the annular space between a fixed central disk and a rotating outer disk. For very shallow packs, the shear band measured at the top surface is narrow and located at $r = R_s$. The inner region directly above the central disk is stationary while the remaining part rotates as a solid. As the filling height of the material, H , increases, the shear band increases in radial width and moves toward the cylinder axis. For sufficiently large H , the shear band overlaps the axis at $r = R_{in}$ i.e. qualitatively different behavior. Indeed, Unger et al. [18] predicted that the shape of the boundary between moving and stationary material would undergo a first-order transition as H is increased past a threshold value H^* : the shearing region which for $H < H^*$ is open at the top and intersects the free surface abruptly collapses to a closed cupola completely buried inside the bulk. Ries et al. [19] measured the width of the shear band in the bulk as a function of height in the system from DEM simulations. Unger et al. [18] predicted the position of the shear band center as a function of height in the system applying the *principle of least dissipation of energy*.

Previous studies focused primarily on the surface and bulk flows in shallow containers for dry granular flows and left unexplored many questions about the effect of interstitial liquid on the shear band for wet granular materials. A small amount of interstitial liquid in granular materials is likely to introduce inter-particle adhesive forces and thus results in a bulk cohesion of the materials. Singh et al. [20] studied the effect of dry cohesion on the width and the position of the shear band by DEM simulations, including a detailed report on the local rheology and micro-structure. The general conclusion was that both the position and the width of the shear band remain unaffected in a cohesive system for $Bo < 1$, while the shear band moves inward and becomes wider for $Bo > 1$. In the similar spirit as for the dry cohesive system, we intend here to experimentally investigate the surface flow profile of dry and wet granular materials.

Continuum fields are often need to be constructed from discrete particle data for stationary or transient dynamic particulate systems. One such approach is applying coarse graining (CG); the method has several advantages: (i) the fields automatically satisfy the conservation equations of continuum mechanics (ii) particles are not assumed to be rigid or spherical and (iii) the results are valid for single particles and single snapshots (no averaging over ensembles of particles or snapshots). This CG-technique was initially proposed by [21] and has been applied extensively to obtain continuum fields from discrete element simulations [22–26]. In our present study, we explore Particle Tracking Velocimetry for measuring the surface velocity profile of granular materials. Thereby, we obtain discrete particle data from the experiments. Our novel approach is to apply the aforementioned CG technique using Mercury CG tools to obtain continuum fields from discrete experimental data. Moreover, our exploration in this paper is not limited to dry granular materials; we apply both the tracking by PTV and obtaining the continuum velocity fields by CG for investigating the surface velocity profile of wet granular materials as well. The primary challenges are to track the tracer particles (i) in a two phase system and (ii) in a system where particles are closely bonded.

Another purpose of the experimental investigations is to measure the total torque required to shear the material. The net torque can be measured as difference from the

unloaded and the loaded shear cell torques. We intend to measure the torque required to shear dry glass beads as well as glass beads mixed with different concentrations of liquids: glycerol and silicon oil. The original idea was to compare the experimentally measured torque with the torque obtained from simulations in [27] and thus validate them. A similar experimental work was done by Wortel et al in [28] to explore the rheology of weakly vibrated dry granular materials. However, this aspect of our experimental work is still under progress. We plan to re-do the experiments for measuring torque as a future part of our research.

We focus on the flow observed at the free surface. We measure the shear band properties from the surface velocity profile of dry and wet glass beads and present the set-up in Sec. 7.2, the velocity tracking in Sec. 7.3.1 and the coarse-graining of experimental data in 7.3.2. The observations for dry and wet glass beads experiments are given in Sec. 7.4 and 7.5, respectively. Finally, we conclude in Sec. 7.6.

7.2. EXPERIMENTAL SET-UP

We probe the rheology of granular media in split-bottom shear cell geometry shown in Figure 7.1. This geometry proposed by Fenistein et al. [17] is a modification of the Couette cell, that leads to the formation of a wide shear zone near the free surface which is free from the boundary effects.

7.2.1. GEOMETRY

The shear cell consists of a rotating outer cylinder of radius $R_o = 110$ mm, a fixed inner cylinder of radius $R_i = 14.7$ mm and a split at the bottom of the shear cell at $R_s = 85$ mm. This split separates the rotating outer part from the stationary inner part of the shear cell. The inner wall is made rough by an additional rough layer that is fastened over the wall. The annular space between the inner and the outer cylinder is filled in with glass beads upto a given filling height H . The filling height is according to the parameters given in Table 7.1. For shallow layers, a narrow shear zone is developed above the split at R_s . With increasing height within the system, this shear zone shifted away from R_s and broadened continuously and without any apparent boundary. The outer cylinder rotates at a constant frequency f . We vary the rotation rate of the outer cylinder according to the parameters given in Table 7.2, keeping the default filling height constant at $H = 36$ mm. The rotational motion is driven by a motor attached to the bottom of the setup. Figure 7.1 shows the experimental set-up, as captured by the high speed camera, with the moving region indicated by the hazy particles and the static region indicated by the clearly defined particles and a schematic figure for the same set-up.

7.2.2. PARTICLES

We use transparent glass beads from Singmund Lindner, SiLi beads type S. We analyse the distribution of the size specification provided by the manufacturer and find a Gaussian size distribution with mean diameter $d_p = 1.70$ mm and width of the distribution equal to ± 0.083 mm. We measure the surface flow profile of the granular glass beads by image analysis of the surface snapshots. We use the PTV technique to measure the velocity of the seed particles that are added as resident tracers to the bulk. The correct choice

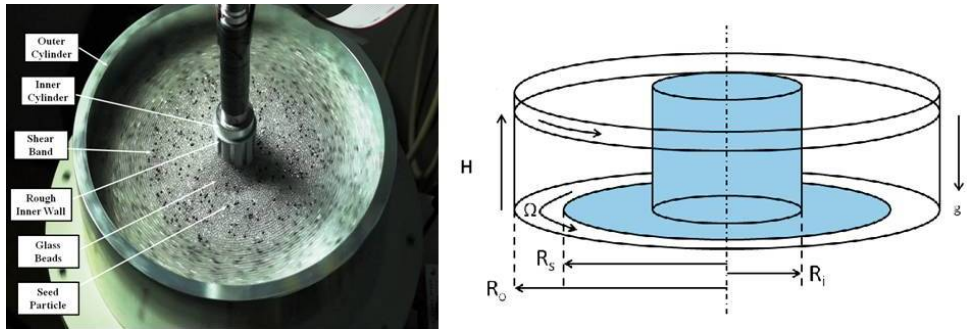


Figure 7.1: The experimental setup of the split-bottom shear cell (left) and schematic (right).

of seed particles is critical to the successful execution of PTV experiments. The source of PTV signals is the scattering of the residual particles, and thus the physical properties of those particles influence signal quality. Particle size, composition, density, shape, and concentration are important factors when selecting seed particles. Seed particles should be small enough to follow the flow being measured, but large enough to generate a strong signal. The physical properties of these particles should be close to the properties of the bulk granular particles to guarantee that they properly represent the flow behavior. The two-dimensional (2D) PTV, in which the flow field is measured at the illuminated surface, requires a low density of the residual particles to allow for tracking each of them individually for several successive frames. Since the high frame rate of the camera allows a very short exposure time, the illumination of the system has to be strong and homogeneous enough for the cameras to see the light reflected by the granular particles, including the tracer particles, in every part of the measurement field.

7

7.2.3. LIQUIDS AND CONCENTRATIONS

Our primary focus in the experiments was to determine the shear band properties from the surface velocity profile, obtained by 2D Particle Tracking Velocimetry method. While we do preliminary studies on the properties of dry glass beads, in the later section of this chapter, we discuss on the effect of adding different interstitial liquids on the bulk flow properties. We use primarily two different liquids; glycerol and silicon oil, for doing different experiments. We measure the contact angle properties of the given liquids on the glass bead surface. Aqueous glycerol solution (80% glycerol) has an average contact angle of 24° on the glass surface. Silicon oil sample of the given viscosity of 1000 st has an average contact angle of 7° on the glass bead surface at a standard temperature 25° . However, the surface tension properties of the liquid-solid interface are not measured here. Aqueous glycerol solutions has a standard surface tension of 64 mNm^{-1} . In general, a standard 1000 st silicon oil sample used for the experiments has a surface tension of 40 mNm^{-1} .

We vary the saturation of each of these liquids in a set of experiments. The bulk saturation of liquid in the system is measured by the ratio of the liquid volume to the

pore volume and is defined as:

$$S^* = \pi \frac{1 - \epsilon}{\epsilon^2} \varphi^*, \quad (7.1)$$

where, ϵ is the bulk porosity in the system and the dimensionless volume φ^* is the ratio of the volume of liquid bridge at a contact to the volume of the contacting particles. The liquid saturation S^* of glycerol and silicon oil are varied according to Table 7.3 and 7.4. While most of the given saturation are within the pendular regime of liquid bridge ($S^* \approx 0.30$), we do a set of experiment outside this range to observe its effect.

7.3. VELOCITY MEASUREMENT

Liquid granular flows are often inhomogeneous with shear bands. In geometries such as inclined-plane flows, avalanches and Couette flows, shear bands are narrow with clear distinction between the flowing and the nonflowing zone. In our present study, in a modified split-bottom shear cell, the granular flow is driven from the bottom, not from the side walls. The differential motion of the outer and the inner cylinder creates a wide shear zone away from the side walls. The observed wide shear zone satisfies a number of robust scaling laws and the velocity tails decay as an error function. The flow pattern is influenced by three factors related to the geometry: the split position R_s , the filling height H and the rotation rate f . Though the flow is purely azimuthal and rate independent for small rotation frequency f , it is influenced by the flow rate at higher rotational rate e.g. due to the influence of frictional dissipation among other reasons. Additionally, the flow is also influenced by the presence of interstitial liquid due to the effect of additional attractive force. These motivate us to explore the surface velocity profile of granular materials for varying conditions by the PTV-CG combined method.

7.3.1. PARTICLE TRACKING VELOCIMETRY

Particle tracking velocimetry (PTV) is a Lagrangian approach of measuring the velocity of each of the tracer particles in several successive time frames. We use a two-dimensional PTV in which the surface flow field is measured which is illuminated by a LED light banks. Seeded flow tracers in the surface flow pictures allow for tracking each of them individually for several frames. These particles of interest are ideally of same size and properties as the bulk particles. The data images were individually digitized and stored as (1120×744) pixels by a CCD camera oriented vertically over the illuminated surface, fixed in a tripod. The particles of interest should be ideally between 5 to 20 pixels in diameter. The illuminated test section was recorded at the rate of 120 frames per second. The shear cell is allowed to run initially for a given time interval $t_i = 2/f$, for complete 2 rotations, until a steady state is achieved. The camera is turned on thereafter, to capture frames for analysing surface velocity profile in the steady state. At least of 3000 images are taken to get good results from PTV.

We use a particle tracking code in Matlab in adaption of the *IDL Particle Tracking* software developed by Crocker and Grier [29] originally for colloidal particle tracking. This present Particle Tracking code repository in Matlab was modified by Blair and Dufresne to reach a broader possible community of people who are interested in particle tracking. We demonstrate here the steps for processing original image Figure 7.2(a). The main

features of the particle tracking algorithm are image inversion, use of *Bandpass filtering*, particle detection and linking of the particle locations from the trajectories. First, we do an inversion of the image to improve the contrast as shown in Figure 7.2(b). In this step, we make all the regions outside the drum region also turn black. Followed by this, we do a spatial filtering of the image by using a **Bandpass** filter. This filtering not only enhances the edges by suppressing the low frequencies, but also reduces the noise by attenuating the high frequencies. The background is subtracted from the image by masking the area. Next, we detect the particles by finding the peaks at the centroids of the seed particles on the surface. This plots dots where each particle was found as shown in Figure 7.2(c). Likewise, we find the surface particle locations for all the images from different time snapshots. We link the particles in the corresponding images by a forward-backward search algorithm. The tracker searches for particles that are within a certain *maximum* distance that the particles are expected to move between frames. After all potential matching particles were examined within this maximum range, only a uniquely matching particle is accepted. Thus, we get the trajectories of individual tracer particles over time as shown in Figure 7.2(d). Different colors in the figure represent increasing time snapshots from blue to yellow color. Finally, the velocity vectors corresponding to the matching particles are determined.

After by particle tracking, we determine the location of the center of the shear cell from the principles of least square minimization method [30–32]. In order to locate the center \vec{r}_c , the required condition is to minimize the *dot* product of the two orthogonal vectors, $\vec{r}_i - \vec{r}_c$ and \vec{v}_i . Thus, the sum of the squared residuals over all tracer signals to be optimized is given by:

$$S = \sum [(\vec{r}_i - \vec{r}_c) \cdot \vec{v}_i]^2 \quad (7.2)$$

The above equation is minimized using least squares to locate the center labeled by **O** as shown in Figure 7.2(d). This is a novel technique for locating the center of an (incomplete) circle by fitting the positions and velocity vectors of the particles.

7.3.2. COARSE-GRAINING: DISCRETE TO CONTINUUM VELOCITY FIELD

We use the coarse graining tool MercuryCG to translate the discrete particle velocity to a continuous velocity field v , averaged over a 100 by 100 grid and time t . In this way, we translate the discrete velocity data at each point into a continuous velocity field as shown in Figure 7.3. Followed by this, we obtain the tangential component of the velocity field v_θ in each local grid. Note that the obtained velocity is zero in regions where there are no particles, e.g. outside the drum area and on the fixed part of the drum. Thus, we ignore the locations where the velocity is calculated as exactly zero. The surface flows satisfy a set of simple scaling laws. Denoting the ratio between the observed azimuthal velocity normalised by the imposed external rotation rate Ω rad s^{-1} as $\omega = v_\theta/\Omega$, where $\Omega = 2\pi R_o f$, and the radial coordinate as r , we can capture the flow profiles of shallow layers ($H/R_s < 0.45$) by:

$$\omega(r) = \frac{f}{f_e} \left(\frac{1}{2} + \frac{1}{2} \operatorname{erf} \left(\frac{r - R_c}{W} \right) \right) \quad (7.3)$$

where, f_e is the estimated external rotation frequency obtained from the fit, R_c denotes the position of the shear band center and W denotes its width on the free surface. Thus,

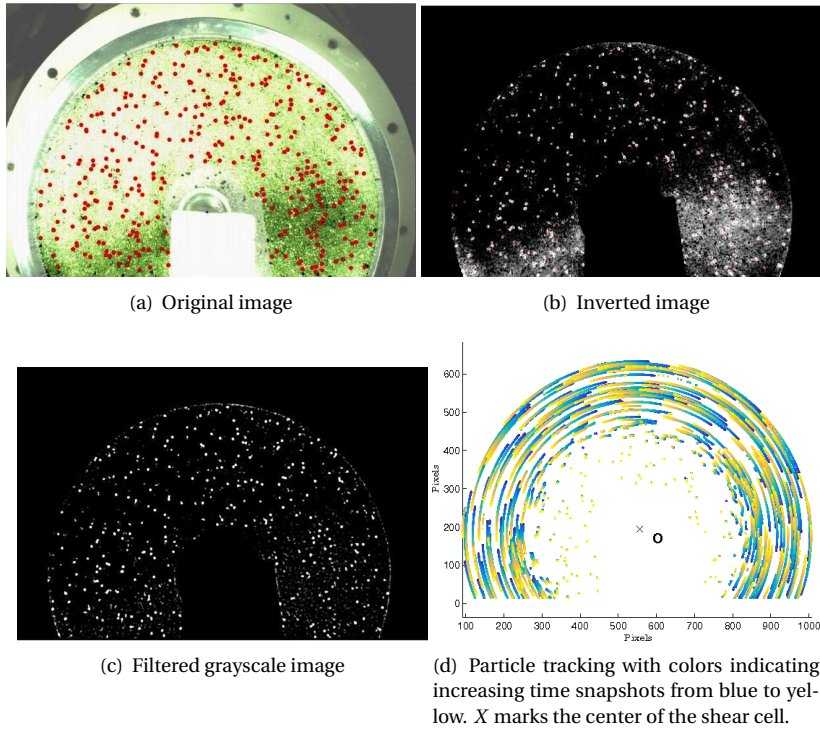
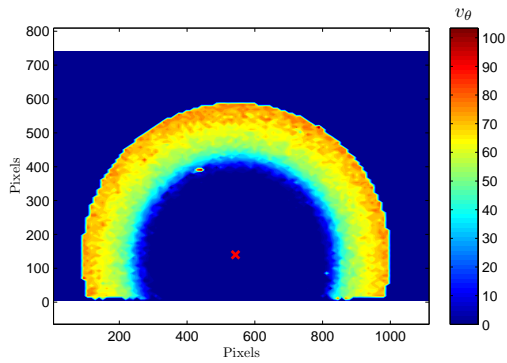


Figure 7.2: Steps of 2D Particle Tracking Velocimetry (PTV).

7

Figure 7.3: Coarse grained velocity field as obtained by processing using MercuryCG tool. X marks the center of the shear cell.

we get an estimation of the width and location of each shear band from the surface velocity profiles.

7.4. EXPERIMENTS WITH DRY GLASS BEADS

In the following subsections, we analyse the effect of varying filling height and shear rate on the width and position of the shear band on the free surface for dry granular materials. As a preliminary work and to verify with the existing established theory, we do experiments with different filling heights H and different external rotation frequency f and measure the surface flow properties for dry granular materials in the following subsections. We compare our results for dry glass beads flow with the existing established theory and experimental work. This is essentially a prerequisite for the experiments with wet glass beads. Figure 7.4 shows a typical velocity profile at the free surface as a function of the radial position which is fitted by Eq. 7.3 to obtain the width W and the position of the shear band center R_c .

Table 7.1: Results for experiments with dry glass beads for different filling heights and $f = 0.03 \text{ s}^{-1}$.

	Filling Height H [mm]	13	18	23	28	32	38
Experiment 1	Width W [mm]	6.17	6.38	6.81	6.92	7.25	8.68
	Position R_c [mm]	81.92	77.8	74.4	72.2	69.7	67.4
Experiment 2	Width W [mm]	6.43	5.92	7.25	6.95	7.17	7.71
	Position R_c [mm]	82.1	77.5	74.4	72.1	70.1	66.9

7

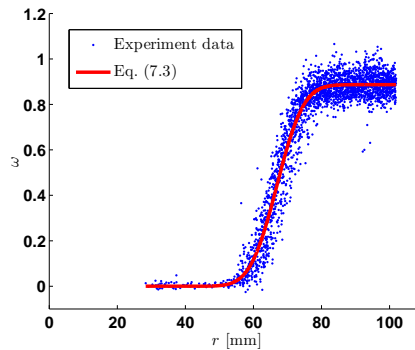


Figure 7.4: Velocity profile as a function of radial position for a filling height of $H = 36 \text{ mm}$. The red solid line represents the fitting given by Eq. 7.3.

7.4.1. VARYING FILLING HEIGHT

For shallow layers, a narrow shear zone develops above with center $R_c < R_s$ at the split at R_s . When H is increased, the shear zone broadens continuously. Therefore, the only

relevant length scales for R_c are the geometric scales H and R_s . The dimensionless displacement of the shear zone, $(R_s - R_c)/R_s$, should thus be a function of the dimensionless height (H/R_s) only and the simple relation fits the data well as:

$$(R_s - R_c)/R_s = (H/R_s)^{5/2} \quad (7.4)$$

Note that R_c , the center of the shear zone, is mostly independent of grain properties. The relevant length scale for the shear zone width W defined above is given by the grain size, and is independent of R_s . Note that grains shape, size, and type also influence $W(H)$: irregular particles display smaller shear zones than spherical ones of similar diameter. The best available experimental data show that the width of the shear zone is related to the filling height H and particle diameter d as:

$$\frac{W}{d_p} \sim \left(\frac{H}{d_p}\right)^{2/3} \quad (7.5)$$

Simulations and experiments essentially confirm these relations [19, 33–35]. We do ex-

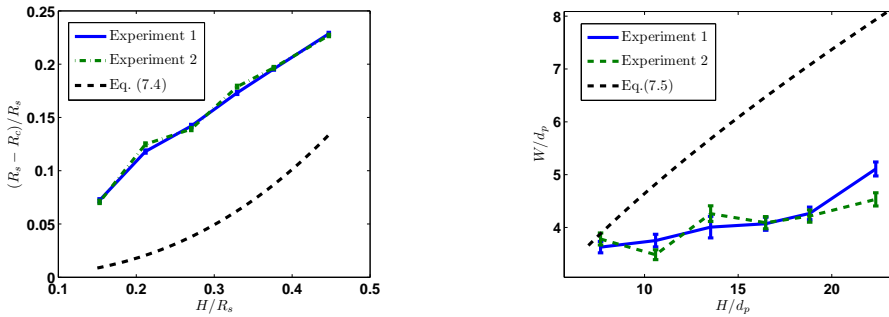


Figure 7.5: (a) Relative shift of the shear band center as a function of scaled filling height H/R_s and (b) scaled width W/d_p of the shear band as a function of scaled filling height H/d_p . Experimental data in the above figures are given in Table 7.1.

periments for measuring the location R_c and width W of the shear band on the flow surface for shallow granular flow, varying the filling height approximately between 10 to 40 mm. However, our experimental results are not conforming to the above mentioned Eqs. 7.4 and 7.5 as shown in Figure 7.5(a) and (b). The dashed lines in the the figures refer to the Eqs. 7.4 and 7.5, respectively, and the data show our experimental results. The results are also presented in Table 7.1. The effective R_s of our system can be slightly different than what we set as $R_s = 85$ mm. The edge of the stationary disk can be probably rough or entirely smooth and both effects can make R_s a bit smaller than its set value. This might shift the data in Figure 7.5(a) downwards a bit, closer to the predicted line. However, the reasons of qualitative non-conformity of our results are not investigated in details here. Note that we do coarse-graining over different sections of the geometry to confirm that there is no effect of geometry on our results. We obtain similar results of R_c and W as a function of H in this case from different sections of the geometry (not shown here). Nevertheless, it is clear that the shear band moves inwards with increasing filling

height and also becomes slightly wider. For filling heights larger than $H \approx 50$ mm (data not shown), deviation from this behavior is observed as the inner cylinder is reached and thus sensed by the shear band.

As Eq. 7.3 already indicates, the flow rate away from the shear band center does not decay exponentially but rather decays like an error function. The difference in the functional form of the tails of wide shear zones and narrow shear bands is discussed in [36], which shows surface flow profiles in a Couette split-bottom cell. The resulting flows are similar to the split-bottom geometry for small H , but for increasing filling heights, the flow profiles reach the inner cylinder, become independent of H , and exhibit exponential tails, independent of grain shape [17].

7.4.2. VARYING SHEAR RATE

Shear localization is a generic feature of flows in yield stress fluids and soft glassy materials but is incompletely understood. In the classical picture of yield stress fluids, shear banding happens because of a stress heterogeneity. The shear band is given by a 6 to 8 grain diameters thick layer where the frictional dissipation is more intense than on the average. A higher shear rate would result in a more intense frictional dissipation inside the shear band. A natural effort to minimise this dissipation would result in shifting the shear band inwards for higher shear rate [18]. On the other hand, transition in regime in granular flow results in more heterogeneous force distribution network [50, 51], shorter lengths of force chain and increasing diffusion of particles, indicating towards a wider shear band. Dijkstra [37] investigated the effect of shear rate on the surface width and position of the shear band. We vary the external rotation rates between $f = 0.01$ to 0.50 s^{-1} keeping a constant filling height $H \approx 36$ mm. The surface velocity profiles are obtained for the varying rotation rates with images captured at a constant 120 frames per second to conform with the threshold criteria for the highest rotational velocity of 0.50 s^{-1} . The stationary velocity profiles are found to develop after two complete rotations (covered in a time interval $t_i = 2/f$) and remain stable thereafter in steady state. Thereby, we obtain the position of the shear band center and its width from the flow profile as mentioned in Sec. 7.3.2. Figure 7.6(a) and (b) show the scaled shear band center location and the shear band width plotted against the external rotation frequency f of the shear cell as obtained from our experiments given by the green \circ . The results are also presented in Table 7.2. Our experimental data is also compared with [37] and the comparisons are shown in the figures. The shear band moves inwards (a little) and gets wider with increasing shear rate as expected.

We compare the results of our experiments with simulations of particle friction coefficient $\mu_p = 0.01$ as given by the blue ∇ in Figure 7.6. The shear band is wider and the position of the shear band is outwards for the simulation data $\mu_p = 0.01$, mean particle diameter $d_p = 2.2$ mm, $d_{\max}/d_{\min} = 2.0$ with a homogeneous size distribution of particles, as compared with the experimental data. Next we run simulations with particle friction $\mu_p = 0.50$ and mean particle diameter $d_p = 2.2$ mm as given by the brown $*$ in Figure 7.6. The presence of friction does not affect the qualitative behavior of the center position and the width: the shear band with friction moves inwards slightly more rapidly and is also somewhat narrower. Thus for calibrating our simulation results with the experiments, simulations with higher particle friction might approach our experimental

results.

As a next step to match simulation results with experiments, we run new simulations with $\mu_p = 0.50$, mean particle diameter $d_p = 1.7$ mm and particle size distribution as mentioned in Sec. 7.2.2. However, the results deviate from the experimental results as shown by the blue \diamond in Figure 7.6. Changing the particle friction to $\mu_p = 0.80$ in our simulations also does not change the simulation results significantly as shown by the red \triangle in Figure 7.6(a) and (b). Though the simulation results do not agree quantitatively, all the results show qualitative agreement with the experimental results. This observation is consistent with the previous studies on non-cohesive dense emulsions in a split-bottom shear cell geometry [38]. Slower shearing does not affect the position and width of the shear band. Faster shearing moves the shear band inwards and makes it wider.

Table 7.2: Results for experiments with dry glass beads for different rotation frequencies and $H = 36$ mm.

Rotation frequency f [s^{-1}]	0.01	0.03	0.07	0.19	0.50
Width W [mm]	7.30	7.90	8.30	8.70	8.60
Position R_c [mm]	68.3	67.4	67.3	67.4	66.9

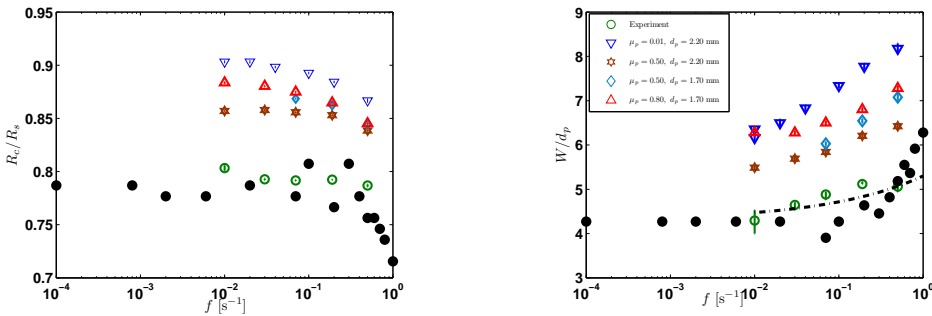


Figure 7.6: a) Scaled position R_c/R_s of the shear band center b) scaled width W/d_p of the shear band at the surface as a function of the rotation frequency f . The dash-dotted line shows a power law $W \sim f^{0.38}$ to allow comparison with the predictions from Jop et al. [39] and the black solid \bullet is the comparison with data from Dijkstra et al. [37]. Experimental data in the above figures (green \circ) are given in Table 7.2.

7.5. EXPERIMENTS WITH WET GLASS BEADS

Previous studies showed that the position and width of the shear band has a strong dependence on inter-particle cohesion. Such inter-particle cohesion can be introduced by adding interstitial liquid to the glass beads. Preceded by the preliminary experiments on dry glass beads, the objective of this section is to study the effect of interstitial liquid on shear band properties. Experiments are done for wet glass beads with two different interstitial liquids; namely, glycerol and silicon oil. The idea is to compare the role of interstitial liquids of different properties on the bulk rheology of wet glass beads. Several runs of experiments were done for both the cases of interstitial liquid with different

liquid volumes added to the system.

7.5.1. EFFECT OF GLYCEROL

We varied the glycerol content from 0 to 25 ml, added to bulk material of 1.97 kg, which corresponds to a varying saturation of 0 to 0.41. We track the velocity of the particles and get the continuous velocity profile in each of the cases of different saturation of glycerol. With the addition of a small amount of glycerol to the glass beads, we observe a finite slip velocity of the particles close to the stationary walls as shown in Figure 7.7(a). This is due to the slippage of the particles on the wall surface. Thus, we fit the data with an error function, taking into account the slip, given as:

$$\omega(r) = \frac{f}{f_e} \left(\frac{1 + \bar{s}}{2} + \frac{1 - \bar{s}}{2} \operatorname{erf} \left(\frac{r - R_c}{W} \right) \right) \quad (7.6)$$

where \bar{s} is the slip in the velocity profile. It is further observed that the slip increases with the net glycerol content added to the glass beads which is shown in Figure 7.7(b). Addition of a small amount of glycerol to the glass beads make them sticky, forming agglomerates. The agglomerates of particles move together as a clump and often they have a slippage at the inner wall due to less friction between the walls and the particles. Though precautions are taken to make the inner wall surface rough by fastening an artificial rough surface on the inner wall, this measure seems to be not enough to prevent slippage even for small amount of glycerol. The shear band becomes wider and moves inwards which is an indication of flow behavior of cohesive materials. The results are presented in Table 7.3. Figure 7.8(a) shows an increasing trend of the width of the shear band W scaled by the particle diameter d_p plotted against the glycerol saturation S^* , indicating that the shear band gets wider. Figure 7.8(b) shows an decreasing trend of the position of the shear band center at the surface R_c relative to the split location R_s plotted against the glycerol saturation S^* , indicating that the shear band moves inwards.

Table 7.3: Results for experiments with glass beads and glycerol for $f = 0.03 \text{ s}^{-1}$ and $H = 36 \text{ mm}$.

Glycerol saturation S^*	0	0.08	0.17	0.25	0.41
Width W [mm]	7.9	18.45	21.12	18.75	20.06
Position R_c [mm]	69.5	62.2	58.9	61.2	60.7
Slip \bar{s}	0	0.15	0.13	0.21	0.18

The shear band is the region with a strong velocity gradient and is caused by the *sliding motion* of the particles. However, strong cohesive forces keep particles in contact (in other words, the cohesive forces promote *collective motions* of particles) and prevent them from sliding. As a result, the velocity gradient is smoothed and the width of the shear band is broadened. This observation is consistent with the previous studies on adhesive dense emulsions [20, 38]. Interestingly, such an effect of cohesion is suppressed if the global Bond number is less than 1, where our experimental data agrees well with previous theoretical/numerical studies on noncohesive particles. Hence, the global Bond number, Bo , captures the transition between essentially noncohesive free-flowing granular assemblies ($Bo < 1$) to cohesive ones ($Bo > 1$). The Bond number for

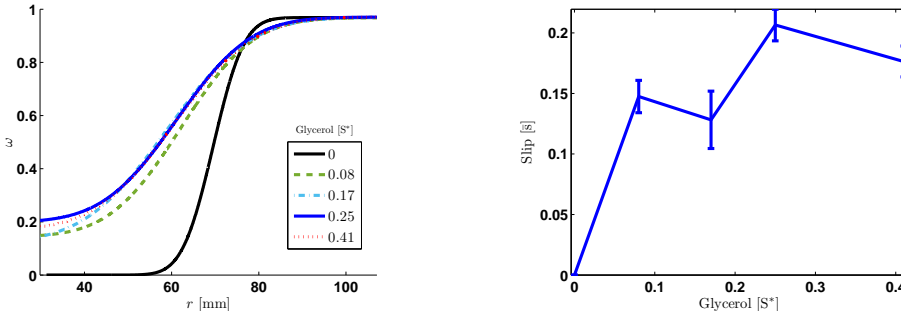


Figure 7.7: Surface velocity profile ω/Ω as a function of radial position r for glass beads mixed with different volumes of glycerol. Experimental data for slip in the above figure are given in Table 7.3.

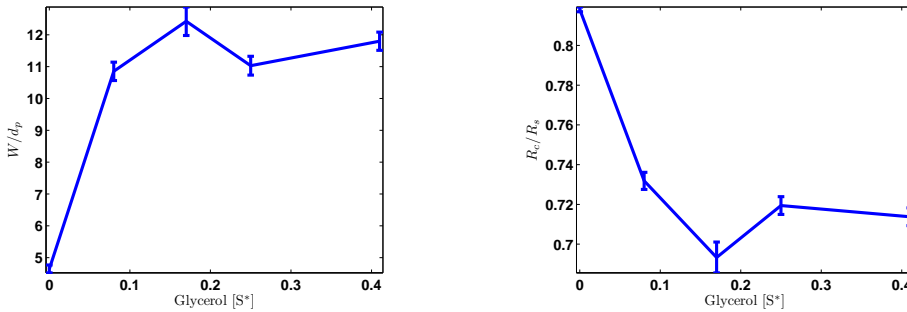


Figure 7.8: (a) Width of the shear band scaled with particle diameter W/d_p and (b) position of the shear band center at the surface relative to the split position R_c/R_s as a function of glycerol saturation S^* . Experimental data for slip in the above figure are given in Table 7.3.

wet cohesive materials increase linearly with the surface tension of the liquid. Thus, the Bond number increases by adding a small amount of liquid as compared with the dry materials. However, the Bond number does not increase significantly with saturation, adding more liquids. Thus the position and the width of the shear band increase significantly from dry to wet transition of granular system, but not the same by adding more amount of liquid.

7.5.2. EFFECT OF SILICON OIL

The saturation of silicon oil is also varied from 0 to 0.41 for different experiments in the similar way as experiments done with glycerol. The results of width W and position R_c of the shear band at free surface for different saturation of silicon oil content are presented in Table 7.4. Figure 7.9 shows the velocity profile for different saturation of silicon oil. Unlike glycerol, we observe no slippage at the inner wall with addition of oil. Thus the error function fit is given without slip effect as Eq. 7.3. We observe a rather decrease in width and a outward shift of the shear band location for increasing silicon oil con-

centration shown in Figure 7.10(a) and (b) respectively, in contrast to what we observe for increasing concentration of glycerol. The wetting and the capillary action behavior is strongly dependent upon the physical properties of the liquids (surface tension and viscosity) and roughness of the surfaces. Glycerol having a higher surface tension compared to silicon oil, is likely to exhibit a stronger capillary effect than silicon oil. However, we use a sample of silicon oil of viscosity 1000 St which is highly viscous. The dynamic contact angles increase with increasing the viscosity of liquids. Higher viscosity liquids tend to produce low wettability caused by higher viscous dissipation that reduces the rate of spreading. This is a probable reason why silicon oil as interstitial liquid exhibit very weak changes to the shear band properties.

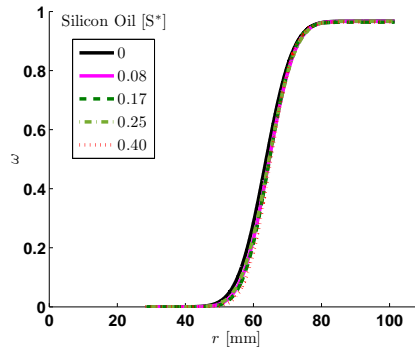


Figure 7.9: Surface velocity profile of glass beads mixed with different volumes of silicon oil.

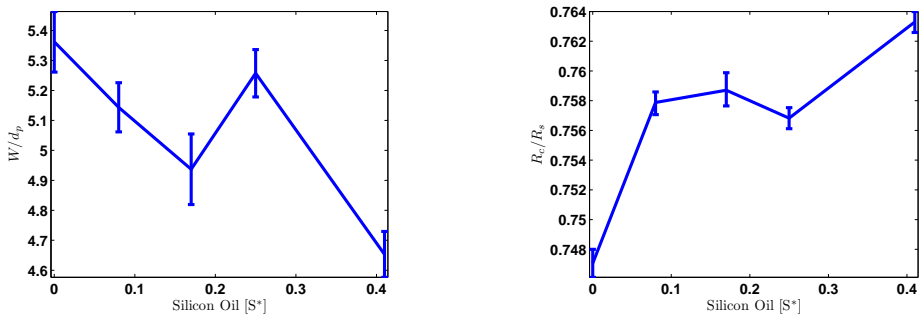


Figure 7.10: (a) Width of the shear band scaled with particle diameter W/d_p and (b) position of the shear band center at the surface relative to the split position R_c/R_s as a function of silicon oil saturation S^* . Experimental data for slip in the above figure are given in Table 7.4.

Table 7.4: Results for experiments with glass beads and silicon oil for $f = 0.03 \text{ s}^{-1}$ and $H = 36 \text{ mm}$.

Silicon Oil saturation S^*	0	0.08	0.17	0.25	0.41
Width W [mm]	9.12	8.74	8.39	8.94	7.91
Position R_c [mm]	63.5	64.4	64.5	64.3	64.9

7.6. CONCLUSION

Our primary focus in the experiments is to determine the shear band properties from the surface velocity profile, obtained by 2D Particle Tracking Velocimetry method. Previous studies focused primarily on the surface and bulk flows in shallow containers for dry granular flow, while our goal in this paper is beyond that to do experiments on wet granular flow: glass beads with interstitial liquids glycerol and silicon oil. This paper describes the novel approach of successfully implementing the PTV-CG combination to obtain discrete to continuum data from experiments. The MercuryCG tool which is primarily designed for coarse-graining data from DEM simulations and evaluation of continuum fields, is proven to be applicable on discrete experimental data as well.

Preliminary studies on dry glass bead experiments showed that the shear band moves inwards and gets slightly wider with increasing filling height of the material in the shear cell. However, these results are not qualitatively conforming to the studies done before which are quite extensive and robust. The reasons behind the disagreement of our results with earlier published trends with different filling heights is not clearly known. Preliminary studies on dry glass bead experiments also showed that the shear band moves inwards and gets wider with increasing rotation frequency of the shear cell. These results are in better agreement with some of the previous studies. Further, experiments with glycerol added as interstitial liquid, resulted in an inner wall slippage, an increase in width and inwards shift of the shear band. Unlike for glycerol, experiments with silicon oil as interstitial liquid showed no significant change in the shear band width and position. Highly viscous silicon oil is likely to have an increased dynamic contact angle and thus the wettability is reduced. This is one probable reason for silicon oil not showing significant effect on the shear band properties.

The deviations observed in the surface flow profile for different filling heights from the earlier published results is noteworthy. We are working in the direction of finding a possible explanation for this deviation; this work is in progress. Another open issue is to re-do more experiments on very small saturation of glycerol and silicon oil in glass bead as interstitial fluid.

REFERENCES

- [1] T. Kawaguchi, *Advanced Powder Technology* **21**, 235 (2010).
- [2] K. M. Hill, A. Caprihan, and J. Kakalios, *Physical Review Letters* **78**, 50 (1997).
- [3] M. Guler, T. B. Edil, and P. J. Bosscher, *Journal of Computing in Civil Engineering* **13**, 116 (1999).
- [4] H. Capart, D. Young, and Y. Zech, *Experiments in Fluids* **32**, 121 (2002).

- [5] D. Bonamy, F. Daviaud, and L. Laurent, *Physics of Fluids* **14**, 1666 (2002).
- [6] G. A. Bokkers, M. van Sint Annaland, and J. A. M. Kuipers, *Powder Technology* **140**, 176 (2004).
- [7] J. A. Laverman, I. Roghair, M. van S. Annaland, and H. Kuipers, *The Canadian Journal of Chemical Engineering* **86**, 523 (2008).
- [8] C. Zeilstra, J. Collignon, M. Van der Hoef, N. Deen, and J. Kuipers, *Powder Technology* **184**, 166 (2008).
- [9] H. T. Chou and C. F. Lee, *Granular Matter* **11**, 13 (2009).
- [10] W. L. Yang and S. S. Hsiau, *Chemical Engineering Science* **61**, 6085 (2006).
- [11] C. C. Liao and S. S. Hsiau, *Chemical Engineering Science* **64**, 2562 (2009).
- [12] S. Shirsath, J. Padding, H. Clercx, and J. Kuipers, *Chemical Engineering Science* **134**, 312 (2015).
- [13] D. Gollin, W. Brevis, E. T. Bowman, and P. Shepley, *Granular Matter* **19**, 42 (2017).
- [14] C. Veje, D. W. Howell, and R. Behringer, *Physical Review E* **59**, 739 (1999).
- [15] B. Utter and R. P. Behringer, *Physical Review E* **69**, 031308 (2004).
- [16] V. Jasti and C. F. Higgs III, *Physical Review E* **78**, 041306 (2008).
- [17] D. Fenistein and M. van Hecke, *Nature* **425**, 256 (2003).
- [18] T. Unger, J. Török, J. Kertész, and D. E. Wolf, *Physical Review Letters* **92**, 214301 (2004).
- [19] A. Ries, D. E. Wolf, and T. Unger, *Physical Review E* **76**, 051301 (2007).
- [20] A. Singh, V. Magnanimo, K. Saitoh, and S. Luding, *Physical Review E* **90**, 022202 (2014).
- [21] I. Goldhirsch, *Granular Matter* **12**, 239 (2010).
- [22] T. Weinhart, A. R. Thornton, S. Luding, and O. Bokhove, *Granular Matter* **14**, 289 (2012).
- [23] A. Thornton, T. Weinhart, S. Luding, and O. Bokhove, *International Journal of Modern Physics C* **23**, 1240014 (2012).
- [24] T. Weinhart, A. R. Thornton, S. Luding, and O. Bokhove, *Granular Matter* **14**, 531 (2012).
- [25] T. Weinhart, R. Hartkamp, A. R. Thornton, and S. Luding, *Physics of Fluids* **25**, 070605 (2013).

- [26] D. R. Tunuguntla, A. R. Thornton, and T. Weinhart, *Computational Particle Mechanics* **3**, 349 (2016).
- [27] S. Roy, A. Singh, S. Luding, and T. Weinhart, *Computational Particle Mechanics* **3**, 449 (2016).
- [28] G. H. Wortel, J. A. Dijksman, and M. van Hecke, *Physical Review E* **89**, 012202 (2014).
- [29] J. C. Crocker and D. G. Grier, *Journal of Colloid and Interface Science* **179**, 298 (1996).
- [30] D. Umbach and K. N. Jones, *IEEE Transactions on Instrumentation and Measurement* **52**, 1881 (2003).
- [31] P. R. Bevington, D. K. Robinson, J. M. Blair, A. J. Mallinckrodt, and S. McKay, *Computers in Physics* **7**, 415 (1993).
- [32] L. Y. Chang and N. S. Pollard, *Journal of Biomechanics* **40**, 1392 (2007).
- [33] X. Cheng, J. B. Lechman, A. Fernandez-Barbero, G. S. Grest, H. M. Jaeger, G. S. Karczmar, M. E. Möbius, and S. R. Nagel, *Physical Review Letters* **96**, 38001 (2006).
- [34] M. Depken, J. B. Lechman, M. van Hecke, W. van Saarloos, and G. S. Grest, *Europhysics Letters* **78**, 58001 (2007).
- [35] S. Luding, *Particulate Science and Technology* **26**, 33 (2008).
- [36] P. Schall and M. van Hecke, *Annual Review of Fluid Mechanics* **42**, 67 (2009).
- [37] J. A. Dijksman, *Granular Media: Flow & Agitations* (Granular and Disordered Media, Leiden Institute of Physics, Faculty of Science, Leiden University, 2009).
- [38] G. Ovarlez, S. Rodts, A. Ragouilliaux, P. Coussot, J. Goyon, and A. Colin, *Physical Review E* **78**, 036307 (2008).
- [39] P. Jop, *Physical Review E* **77**, 032301 (2008).
- [40] C. Bonnoit, J. Lanuza, A. Lindner, and E. Clement, *Physical Review Letters* **105**, 108302 (2010).
- [41] N. Huang and D. Bonn, *Journal of Fluid Mechanics* **590**, 497 (2007).
- [42] A. Ries, D. E. Wolf, and T. Unger, *Physical Review E* **76**, 051301 (2007).
- [43] P. Jop, Y. Forterre, and O. Pouliquen, *Nature* **441**, 727 (2006).
- [44] O. Pouliquen, C. Cassar, P. Jop, Y. Forterre, and M. Nicolas, *Journal of Statistical Mechanics: Theory and Experiment* **2006**, P07020 (2006).
- [45] Y. Forterre and O. Pouliquen, *Annual Review of Fluid Mechanics* **40**, 1 (2008).

- [46] S. Luding, A. Singh, S. Roy, D. Vescovi, T. Weinhart, and V. Magnanimo, in *Proceedings of the 7th International Conference on Discrete Element Methods* (Springer, 2016) pp. 13–19.
- [47] D. L. Henann and K. Kamrin, *Proceedings of the National Academy of Sciences* **110**, 6730 (2013).
- [48] N. J. Wagner and J. E. Brady, *Physics Today* **62**, 27 (2009).
- [49] A. Fall, F. Bertrand, G. Ovarlez, and D. Bonn, *Journal of Rheology* **56**, 575 (2012).
- [50] X. Wang, H. Zhu, S. Luding, and A. Yu, *Physical Review E* **88**, 032203 (2013).
- [51] C. S. Campbell, *Journal of Fluid Mechanics* **539**, 273 (2005).

8

CONCLUSIONS AND OUTLOOK

The focus of this thesis concerned modelling the response of quasistatic dense wet granular flows subjected to shear. Granular media have been studied since decades using several discrete simulation techniques like Contact Dynamics (CD), Event Driven (ED) or the DEM approach. However, only small systems can be modelled at this level of detail. Here, they are used to extract continuum constitutive relations, forming the basis for a hydrodynamic theory of granular materials. Such multiscale granular research is the way forward towards pure continuum modeling of these systems. Given that very little was explored on wet granular flow, this thesis focused on partly saturated granular systems, primarily on their rheology, in the initial parts of this thesis. We make an attempt to understand and predict the rheology of shear-driven partially saturated granular flows through discrete particle simulations by utilising accurate discrete to continuum mapping methods, i.e. a micro-macro transition. In the second part of this thesis, we focus on the migration of interstitial liquid itself within the granular media and predict their flows through continuum models, discrete particle simulations and ensure close agreement between the two methods. Additionally, we used also experimental techniques to explore some of the rheological properties of dry and wet granular flows.

Dense granular materials obey a local, phenomenological rheology, known as the $\mu(I)$ -rheology, that can be expressed in terms of relations between non-dimensional quantities: shear to normal stress ratio μ and inertial number I . While the classical $\mu(I)$ -rheology is well established from extensive studies in different geometries from simulations and experiments, recent studies confirmed that the effect of local compressibility p^* must also be included to characterize the bulk granular flow behavior when particles are not perfectly rigid. Confirming this and investigating further, we realized that other non-dimensional numbers such as pressure scaled by gravity p_g^* and cohesion scaled by pressure, i.e. the Bond number Bo , are vital for the full flow characterization, especially near the free surface and for cohesive materials, respectively. As a step forward, towards application, in Chapters 2 and 3, we have showcased the strength of DEM in modeling generalized rheological constitutive relations for the macro friction coefficient and the local volume fraction. This generalized phenomenological rheology is valid for a

wide range of granular flows, from dense quasistatic to dynamic inertial flows, for a wide range of compressibilities (hard to soft particles) and for non-cohesive to wet cohesive material flows. A comparative study on the viscosity of non-cohesive to wet cohesive granular materials shows a significant increase in viscosity and change in flow behavior with increasing Bond number. Indeed, the shear-thinning rate of a granular fluid which reduces with increasing Bond number, is captured remarkably well by the generalized constitutive relation for the macro friction coefficient.

The mechanical properties of dry and wet granular materials are important both for practical and fundamental reasons. Bulk cohesion is one extrinsic mechanical property of wet granular materials that varies depending on the bulk saturation and the properties of the interstitial liquid. Previous analyses were done, starting from numerical simulations and experiments to see the effect of micro adhesion on the bulk cohesion. In Chapter 4 of this thesis, we have used Discrete Element Method simulations to study the cohesive response of wet granular materials based on varying micro-properties. In particular, we have obtained definite micro-macro correlations for the bulk cohesion as a function of bulk saturation and interstitial liquid surface tension. Inter-particle cohesion can arise from a variety of sources: van der Waals forces, electrostatic forces, liquid bridging (capillary) forces; our motivation being the latter. We have identified the key parameters of different contact models, pertaining to different origins of interparticle cohesion, that result in identical bulk cohesion. The maximum adhesive force and the adhesive energy dissipated per contact are identified as the two key parameters of the contact models.

Interstitial liquid migration from the shear band is a known mechanism in unsaturated granular media, supposedly established by experimental studies and continuum description. We have studied in detail the transient and theoretical description of interstitial liquid movement in Chapters 5 and 6. In Chapter 5, we investigate in depth the interstitial liquid re-distribution on shear. A simple conceptual mechanism is shown to be valid using DEM simulations: interstitial liquid re-distributes to the same state or pattern under large shear strain, irrespective of the different transient behavior. The final liquid distribution is highly sensitive to the maximal liquid bridge volume (an empirical cap parameter, imposing a maximum volume of liquid bridge formed in simulations). The liquid re-distribution process is limited to small shear, before the onset of the dominating diffusive liquid migration behavior at large strains. The latter is the focus of Chapter 6. We perform combined studies by DEM simulations, continuum solutions and analytical solutions in this chapter. In previous experimental studies, the mode of mass transfer of interstitial liquid in unsaturated granular media was stated as a diffusive mode of transfer. Unlike previous observations, we re-phrase this mass transfer of interstitial liquid as an advective-diffusive transfer process, when transformed to a different coordinate frame. Further, we observe that the dynamic high density liquid front between the shear band and the boundaries follows a trajectory which is diffusion dominated. Still, both advection and diffusion are significant, their effects being additive for short times, but deviating from the overall combined liquid migration on larger time scales, which requires numerical solution schemes.

Unlike in previous chapters, we undertake experimental studies in Chapter 7. Our primary focus was to experimentally determine the shear band properties from the sur-

face velocity profile, obtained by 2D Particle Tracking Velocimetry. Previous studies focused on the surface and bulk flows in shallow containers for dry granular flow, while our goal in this chapter has been to go one step further and do experiments on wet granular flow: glass beads with interstitial liquids glycerol and silicon oil. We have done this using coarse-graining using the MercuryCG post-processing tool. This tool is primarily designed for coarse-graining data from DEM simulations and evaluation of continuum fields. However, we have shown that this technique is satisfactorily applied to postprocess discrete data from experiments as well. Preliminary studies on dry glass bead experiments confirmed that the shear band moves inwards and gets wider with increasing rotation frequency of the shear cell. Further, experiments with glycerol added as interstitial liquid resulted in an unexpected inner wall slippage, an increase in width and an inwards shift of the shear band. Unlike for glycerol, experiments with silicon oil added as interstitial liquid showed no significant change in the shear band, the reason still being an open question.

Finally, some important messages and conclusions from this thesis:

1. Bulk cohesion is an extrinsic mechanical property of wet granular materials that varies with the bulk saturation and the properties of interstitial liquid and a definite correlation is established between the micro- and macro- worlds.
2. Generalized constitutive relations are obtained for the macro friction coefficient and the local volume fraction of granular materials steady state flow in terms of granular dimensionless numbers. These form the basis of continuum modeling of general granular flows.
3. Interstitial liquid bridges in partially wet granular materials re-distribute to the same states under shear, irrespective of the initial distribution of the liquid and this basic mechanism has wide range of industrial applications.
4. Mass transfer of interstitial liquid in unsaturated sheared granular media can be re-phrased as a diffusive-convective process in a different coordinate frame, showing that both processes are significant.
5. Shear band properties of granular glass beads flow are determined from experimental measurements of the surface velocity. The addition of interstitial liquid glycerol increases the width of the shear band significantly and moves it inwards, while the addition of silicon oil shows very similar bulk behavior as dry particles.

OUTLOOK

1. It is shown in the thesis by simulations that the experimentally measurable torque can be related to the bulk cohesion of the wet granular materials. Thus, experimentally measuring torque would give us an estimation of wet materials hydrodynamics. A proper validation of the micro-macro correlation through experimental measurement of the torque is desirable. However, a sensitive enough torque meter is required to capture the small differences in torque at different saturation of granular materials.

2. In experimental measurements, addition of glycerol and silicon oil as interstitial liquids to glass beads show different responses in the shear band properties. It is to be further investigated on the reasons for this and for the differences in bulk properties arising from the two different interstitial liquids.
3. Having done experiments with glycerol and silicon oil as interstitial liquid in glass beads, mostly in their intermediate to the limiting pendular regime saturation, we realise that we have a gap in the trend from our experiments for very small saturation of liquid. We need to conduct more experiments in the small saturation regime to clearly capture the trend. Also, we need to do more experiments on different types of interstitial liquids having different surface wetting properties.
4. Our generalized phenomenological rheology takes into account the effect of different micro-mechanical mechanisms via respective granular dimensionless numbers, which capture the effect of varying confining pressure, flow inertia, particle softness and cohesion. However, the effect of kinetic energy of the particles' random motion is important in the inertial flow regime but not captured here. Thus, the rheological models need to be extended to include the effects of granular temperature.
5. Another prospective domain that still lacks clarity is to relate the generalized rheology with the micromechanics of wet granular materials such as the fabric and contact anisotropy.
6. Our goal here was to define the rheology of granular materials in a continuum framework. Now, the overall constitutive relations mentioned above are to be implemented in continuum solvers to recover or even predict the flow rheology such as shear bands and patterns, allowing for the simulation of large systems where DEM simulations are no longer possible.

A

APPENDIX

A.1. CONTINUUM MODEL

A.1.1. CONTINUUM EQUATIONS

Previous studies show different approach for translating granular rheology in the continuum model framework [4]. The continuum equations that are solved are the steady-state axi-symmetric Navier-Stokes equations in cylindrical coordinates. The assumption in the axi-symmetric coordinates is that all derivatives with respect to the azimuthal-coordinate, ϕ are zero. This implies the fluid in the ϕ -direction is constant and the equations can be solved in the two dimensional $z - r$ -plane. The momentum equations after this assumption reads as follows [1]:

$$\rho \left[u_r \frac{\partial u_r}{\partial r} - \frac{u_\theta^2}{r} + u_z \frac{\partial u_r}{\partial z} \right] = -\rho \frac{u_\theta^2}{r} - \frac{\partial p}{\partial r} + \frac{\partial \tau_{rr}}{\partial r} + \frac{\tau_{rr}}{r} - \frac{\tau_{\theta\theta}}{r} + \frac{\partial \tau_{rz}}{\partial z}, \quad (\text{A.1})$$

$$\rho \left[u_r \frac{\partial u_z}{\partial r} + u_z \frac{\partial u_z}{\partial z} \right] = \rho g - \frac{\partial p}{\partial z} + \frac{\partial \tau_{zr}}{\partial r} + \frac{\tau_{zr}}{r} + \frac{\partial \tau_{zz}}{\partial z}, \quad (\text{A.2})$$

$$\rho \left[u_r \frac{\partial u_\theta}{\partial r} + \frac{u_r u_\theta}{r} + u_z \frac{\partial u_\theta}{\partial z} \right] = -\frac{\partial \tau_{r\theta}}{\partial r} + \frac{2\tau_{r\theta}}{r} + \frac{\partial \tau_{z\theta}}{\partial z} + \frac{\partial \tau_{\theta r}}{\partial r} + \frac{\tau_{\theta r}}{r} + \frac{\tau_{r\theta}}{r} + \frac{\partial \tau_{\theta z}}{\partial z}. \quad (\text{A.3})$$

We assume incompressibility, thus mass balance is satisfied by the continuity equation:

$$\frac{\partial u_r}{\partial r} + \frac{u_r}{r} + \frac{\partial u_z}{\partial z} = 0. \quad (\text{A.4})$$

The pressure in the momentum equation enforces this continuity equation; it functions as a Lagrange multiplier. We assume hydrostatic pressure with $\frac{\partial p}{\partial r} = \frac{\partial p}{\partial \theta} = 0$ and $\frac{\partial p}{\partial z} = \rho g$. ρ is the bulk density and $\vec{u} = (u_r, u_\theta, u_z)$ is the velocity. In a granular material the viscosity is written in the form of:

$$\eta = \frac{\mu p}{\dot{\gamma}}, \quad (\text{A.5})$$

Schrojenstein Lantman, M.P. van, Roy, S., Weinhart, T., Thornton, A. R. and Luding, S., Continuum simulation of granular flows: the split bottom ring shear cell, WCCM 2016, Seoul, Korea.

where the friction, μ , is the constitutive relation described in Chapter 2. The equations are solved using the open-source library *Oomph-lib* package. Using Crouzeix-Raviart elements, the axi-symmetric Navier-Stokes equations are discretised and a Newton-iteration method is used to solve the system of equations.

A.1.2. RHEOLOGY

Details of DEM simulations of a split-bottom ring shear cell, given in Chapter 2 have revealed that the macroscopic friction coefficient, μ , depends on a few non-dimensional numbers. For a simple non-cohesive system of particles, these numbers are given in the table below. In these definitions k is the stiffness of a particle, d_p is the mean particle diameter, ρ_p is the material density of a particle, g is the gravity and p is the pressure. Additionally, σ is the surface tension of liquid for wet granular materials (rheology for wet granular materials is not discussed here).

Table A.1: Non-dimensional numbers.

Non-dimensional numbers	Symbol	Definition
Inertial number	I	$\frac{\dot{\gamma} d_p}{\sqrt{\frac{p}{\rho_p}}}$
Softness number	p^*	$\frac{p d_p}{k}$
Surface number	p_g^*	$\frac{p}{\rho_p d_p g}$
Bond number	Bo	$\frac{\pi \sigma}{p d_p}$

The inertial number I is mostly dominant in the flowing region and relates the motion of the particles with the confining pressure, for instance in the shear band of the split-bottom ring shear cell. The softness number p^* is practically a non-dimensional pressure in the DPM simulations as the stiffness and the particle diameter are often taken as constants. The surface number p_g^* is active at the surface where the pressure forces start to diminish compared to the gravity forces.

These non-dimensional numbers have a significant effect on the macroscopic friction. The most well-known effect is the $\mu(I)$ rheology.

$$\mu_I(I) = \mu_o f_I(I) = \mu_o \left[1 + \frac{\Delta\mu/\mu_o}{1 + I_0/I} \right] \quad (\text{A.6})$$

Here, the static friction μ_o , the dynamic friction $\mu_\infty = \Delta\mu + \mu_o$ and I_0 are rheological coefficients that depend on the granular material properties. This rheology works very well for values of $10^{-2} < I < 1$. When using this rheology only, the friction goes to μ_o as I

goes to zero, however in DPM simulations a lower limit has been observed that corrects this behavior for smaller I , known as the stretched exponential as discussed by [2],

$$f_q(I) = 1 - \exp(-(I/I^*)^{\alpha_1}). \quad (\text{A.7})$$

This equation contains the rheology coefficients I^* and α_1 . The physical meaning behind these coefficients still need to be investigated. The corrections for the softness number p^* and surface number p_g^* are, respectively:

$$f_p(p^*) = 1 - \left(\frac{p^*}{p_o^*}\right)^\beta, \quad (\text{A.8})$$

and

$$f_g(p_g^*) = 1 - a' \exp\left(-\frac{p_g^*}{p_{go}^*}\right), \quad (\text{A.9})$$

with p_o^* and p_{go}^* as coefficients determined from DEM simulations. The complete (dry) rheology for the split-bottom ring shear cell is thus given as [3]:

$$\mu(I, p^*, p_g^*) = \mu_o f_I(I) f_q(I) f_p(p^*) f_g(p_g^*). \quad (\text{A.10})$$

A.1.3. CONTINUUM SOLUTION

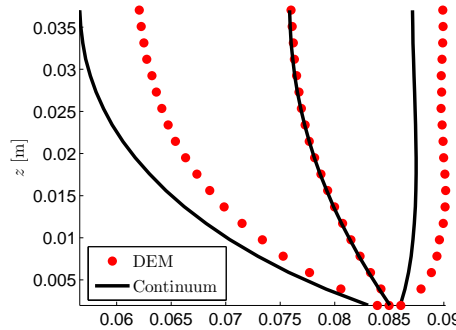


Figure A.1: Comparison of shear band obtained from DEM and continuum solutions.

The components of the stress tensor in Eqns. A.1, A.3 and A.2 are substituted in terms of the granular fluid viscosity obtained from Eq. A.5 [1]. Solving the continuum equations, we obtain the velocity profile and thereby the shear band position and width, fitted by an error function. The shear band position and width, obtained at different heights of the shear cell, are further compared DEM solutions, shown in figure A.1. The centers of the shear band, obtain from continuum solution, are well aligned with the DEM results, the small difference being due to the finite grain size in the DEM. However, the width of the shear band is not aligned with DEM results, the width obtained from continuum solution being asymmetric. Our work in progress is further to improve the continuum results.

REFERENCES

- [1] R Byron Bird, Warren E Stewart, and Edwin N Lightfoot, *Transport phenomena* (John Wiley & Sons, New York 2004).
- [2] Stefan Luding, Constitutive relations for the shear band evolution in granular matter under large strain, *Particuology* **6**, 501–505 (2008).
- [3] Sudeshna Roy, Stefan Luding, and Thomas Weinhart, A general(ized) local rheology for wet granular materials, *New Journal of Physics* **19**, 043014 (2017).
- [4] Ken Kamrin, and David L Henann, Nonlocal modeling of granular flows down inclines, *Soft Matter* **11**, 179–185 (2015).

ACKNOWLEDGEMENTS

“Learn from yesterday, live for today, hope for tomorrow. The important thing is to not stop questioning. Curiosity has its own reason for existing.” -Albert Einstein

Research to me is a lifelong journey en route to the source of light of knowledge. A journey is easier when we travel together. Interdependence is certainly more valuable than independence. This dissertation is the result of four years of work whereby I have been accompanied and supported by many people. It is a pleasant aspect that I have now the opportunity to express my gratitude for all of them.

First and foremost, I would like to thank my advisor, Prof. Stefan Luding for accepting me in this group and introducing me to the world of granular materials. Stefan, during the journey of my PhD, your invaluable suggestions, pointed directions and lucid explanations have helped me in every single step while working on this dissertation. It has been a pleasure for me that you gave me so much freedom in my work and let me travel for many international conferences. Thanks to you that I could see so much and gain insight on other parts of the world. My heartiest acknowledgement to your wife, Gerlinde. I am grateful that Stefan and Gerlinde have made me feel at home in The Netherlands. Your hospitality is always so warm and made me feel closer. You have made a place in my heart, in my mind, that evokes a feeling much beyond a formal relationship.

Dr. Thomas Weinhart, my co-supervisor, your day-to-day advice and supervision has been really invaluable to me. You have shown me the light whenever I seem to have stuck in a dark corner. You always seem to have simple answers to problems that looked so complicated to me. I am really fortunate to have you by my side for the entire journey. The discussions, comments, advice and iterations with you and Stefan have helped me a lot to learn about research and scientific writing. Thomas, I extend my thanks to your wife Raquel for the support and conversation we often had, especially during the initial years of my PhD.

I would like to extend my thanks to Dr. Vanessa Magnanimo for taking the effort for last minute discussion on my thesis. Vanessa, my amateurish proposal writing would have been incomplete without you. Nevertheless, my thanks to Dr. Anthony Thornton for carefully reviewing my papers and providing technical insights. Anthony, perhaps you ever realised that your constant talking and cheerful acts had been the source of entertainment in times of my gloomy mood too. Thank you, Dr. Wouter den Otter for the novel ideas on taking my work to a different direction. Extending my gratitude towards the persons I met beyond my life in the University, I would like to thank Prof. Jin Ooi, Prof. Jens Harting, Dr. Marco Ramaioli, Dr. Joshua Dijkman and Prof. Leonid Berlyand for the appreciation and useful suggestions I received often on my research work. Thanks to the MercuryDPM team, Thomas and Anthony, for making the liquid migration set-up working. Thanks are due for Abhi, Hao, Bert, Harmen, Deepak, Anton and Marnix with whom I have also collaborated while working on this dissertation.

I would like to take this opportunity to thank my fellow labmates - Rohit, Kia, Ahmed, Hoong, Deepak, Durai, Irana, Giuseppe, Sampan, Thejas and Yousef. Rohit, you are the one on whom I could easily count on without a thought. I will never forget the days of my crisis when you have always been here right beside me. You are indeed *a friend in need, a friend indeed*. Thanks Kia for the conversations we often had around the coffee corner and sometimes our trip together with Rohit to Ochtrup. Hao, thanks to your socializing and always providing a solution attitude. Thanks for the Chinese lunch that you often organised in the office. Thanks to your wife Yidan for the nice interactions we had often. Hongyang and Ahmed, thanks to you, my weekends would have been so boring without you in office and without the discussions. Hong, my thanks to your wife Dr. Xinyan Fan too for accompanying us often during the off-hours. I extend my thanks to Deepak for helping me with presenting this thesis in good format and Bert for helping me in writing the *Samenvatting* of this thesis. Thanks to my former labmates - Kay, Kuni, Kit, Kasper, Dalila, Georgio, Nico, Dinant, Vitaliy, Mateusz and Bram too. They all helped and accompanied me wholeheartedly throughout my PhD tenure. Things would not have been easier without the technical support I got from Wouter den Breeijen, thanks Wouter. I express my special thanks to Sylvia for the care and support she has shown to me in these years. I acknowledge Sally for the help I have got from her so often. My friends Shazia and Afsheen at Twente deserve thanks too for helping me to cruise through the graduate life.

I would like to thank all my committee members for their interests in my research. I am grateful to Dr. Niels Kruyt who took all the effort to make a careful assessment of my thesis. Thanks to Prof. Dietrich Wolf, Prof. Sergiy Antonyuk and Prof. Devaraj van der Meer for your kind appreciation of my work. I express my thanks to Prof. Rüdiger Schwarze for making me feel comfortable in the discussion over my thesis before my defense.

Debangshu, you are the constant source of my motivation for the next move in my life. Thanks for triggering and guiding me to take the first step towards my forthcoming journey in US. Life looks promising and blissful with your advent. I am glad to have my good old friends Gaurav, Dwaipayyan and Tridip for their great support. Our last year reunion in New York remains immemorable to me. It was a 'After ten years' reunion after all and the journey continues! Thanks to Sudarshana, Abhi and Shruti for the wonderful time spent in US last year.

My journey to this stage of the academic life has been motivated with the guidance and support of an wonderful person I have come across in my life. I express my deep gratitude to Prof. Bharat Ballal - one of my finest mentors, a true philosopher and guide. I am also thankful to all my other teachers, whose names I could not include here.

I should not have been writing this dissertation without my *Maa*, Bharati Roy who formed part of my vision and taught me the good things that really matter in life. I fondly remember those starry nights at our balcony when we shared many of our dreams. I wish you would have been here to share this golden moment with me, yet I believe you are there in every footstep of my life. The seeds that you have sown in my mind has been thoroughly nurtured by me, you have been my constant source of strength. My life would have been incomplete without my *Baba*, Satyananda and *Dada*, Suvankar by my side. Though life has moved in a different direction, sweet memories of childhood

remain evocative. I express my thanks to all my family members whose name I could not mention here.

Now it is time to thank the abstract objects and other forms of life who have contributed greatly for all these years. Thanks to my old Dell Laptop which has accompanied me throughout this PhD. Thanks to my good old bicycle and my first car for accompanying me every now and then during these days. Thanks to the city of Enschede, the accompanying forests and biking paths, for the wonderful life it provided outside my lab. Nature is always so appealing to me! The church in Hengelo had been my company for every Sunday, the place of my peace.

Finally, I thank myself, my good own self, for being my comfort and showing endurance during the dark phase. I *pranaam* God for His unconditional love, guidance, sustenance and strength. He is the source of all my inspiration, dedication and strength to complete this work.

Sudeshna Roy

University of Twente
January, 2018



CURRICULUM VITAE

Sudeshna Roy

01-10-1984 Born in Kolkata, India.

EDUCATION

2002–2006 B. E. in Chemical Engineering
Jadavpur University, Kolkata

2010–2012 M. Tech. in Metallurgical Engineering and Materials Science
Indian Institute of Technology, Bombay

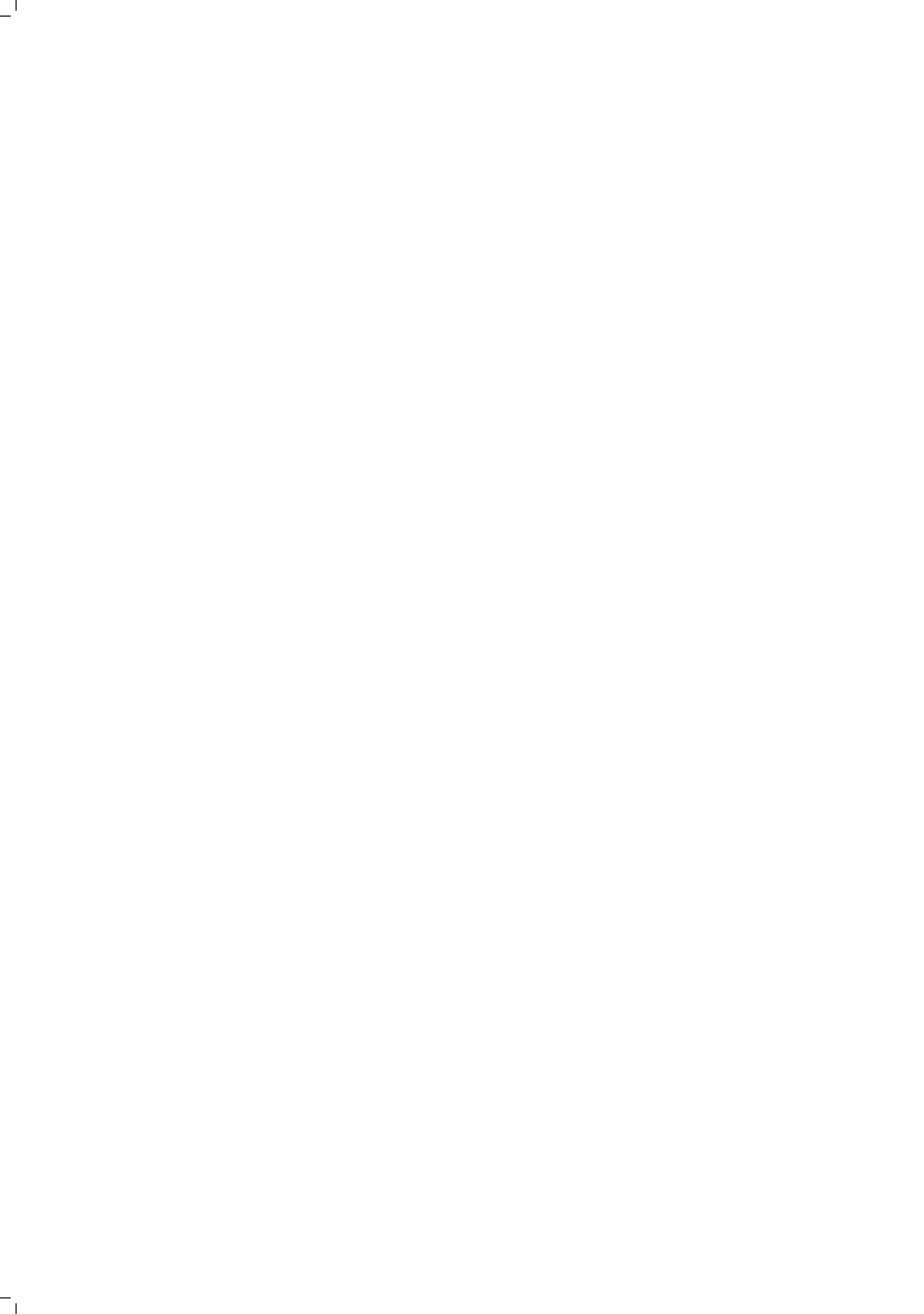
2013–2018 PhD candidate Multi Scale Mechanics
University of Twente, Netherlands
Thesis: Hydrodynamic Theory of Wet Particle Systems
Promotor: Prof.dr.rer.-nat. S. Luding
Co-Promotor: Dr. T. Weinhart

INDUSTRIAL EXPERIENCES

Assistant Manager in Essar Steel Ltd., Process Engineer, Hazira, India,
(September 2006-October 2008).

Assistant Manager in Essar Steel Ltd., Clean Development Mechanism,
Mumbai, India, (November 2008-July 2010).

Deputy Manager in Essar Steel Ltd., Research and Development in Pro-
cess Modeling, Hazira, India, (July 2012-August 2013).



LIST OF PUBLICATIONS

JOURNAL PUBLICATIONS

- **S. Roy**, S. Luding, T. Weinhart, A general(ized) local rheology for wet granular materials, *New Journal of Physics* **19**, 043014 (2017).
- **S. Roy**, A. Singh, S. Luding, T. Weinhart, Micro-Macro Transition and Simplified Contact Models for Wet Granular Materials, *Computational Particle Mechanics* **3**, 449-462 (2015).
- **S. Roy**, S. Luding, T. Weinhart, Liquid re-distribution in sheared granular media, (Chapter 5, *submitted Jan. 2018*).
- **S. Roy**, H. Polman, B. J. Scheper, A. R. Thornton, D. R. Tunuguntla, S. Luding, T. Weinhart, Surface flow profile of dry and wet granular materials using Particle Tracking Velocimetry, (Chapter 7, *to be submitted*).
- **S. Roy**, W. K. den Otter, A. R. Thornton, S. Luding, D. R. Tunuguntla, T. Weinhart, Convective-diffusion liquid migration in unsaturated sheared granular media, (Chapter 6, *to be submitted*).
- H. Shi, **S. Roy**, T. Weinhart, V. Magnanimo, S. Luding, Rheology of granular materials in homogeneous and inhomogeneous system, (*in preparation*).

CONFERENCE PROCEEDINGS

- T. Weinhart, D. R. Tunuguntla, M. P. van S. Lantman, I. F. C. Denissen, C. R. Windows-Yule, H. Polman, J. F. M. Tsang, B. Jin, L. Orefice, K. van der Vaart, **S. Roy**, H. Shi, A. Pagano, W. den Breeijen, B. Scheper, S. Luding, A. Thornton, MercuryDPM: Fast, flexible particle simulations in complex geometries Part II: Applications, V International Conference on Particle-based Methods - Fundamentals and Applications, *PARTICLES* 2017.
- **S. Roy**, S. Luding, T. Weinhart, Effect of cohesion on compaction of soft granular materials, *EPJ Web of Conferences* **140**, 03065 (2017).
- S. Luding, A. Singh, **S. Roy**, D. Vescovi, T. Weinhart, and V. Magnanimo, From particles in steady state shear bands via micro-macro to macroscopic rheology laws, *Proceedings of the 7th International Conference on Discrete Element Methods* 2016.
- **S. Roy**, S. Luding, T. Weinhart, On Time Scales and Rheology of Dry and Wet granular Materials, *Proceedings of the 2nd International Conference for Powder, Granule and Bulk Solids: Innovations and Applications* 2016.
- A. Gladky, **S. Roy**, T. Weinhart, S. Luding, R. Schwarze, DEM simulations of weakly wetted granular materials: implementation of capillary bridge models, *Fourth Conference on Particle-Based Methods, PARTICLES* 2015.

- **S. Roy**, S. Luding, T. Weinhart, Macroscopic bulk cohesion and torque for wet granular materials, Proceedings of the 8th International Conference for Conveying and Handling of Particulate Solids 2015.
- **S. Roy**, S. Luding, T. Weinhart, Towards hydrodynamic simulations of wet particle systems, Procedia Engineering **102**, 1531-1538 (2015).

BOOK CHAPTER

- H. Shi, D. Vescovi, A. Singh, **S. Roy**, V. Magnanimo, S. Luding, Granular flow: from dilute to jammed state, DOI: 10.5772/intechopen.68465.